




Universitetet
i Stavanger

FACULTY OF SCIENCE AND TECHNOLOGY

MASTER'S THESIS

| | |
|--|--|
| Study programme and specialization: Engineering structures and Materials - Machine constructions | Spring semester, 2018 Open |
| Author: Marius Aga Belsvik |  (signature of author) |
| Programme coordinator: Professor Vidar Hansen Supervisor: Geir Tandberg | |
| Title of master's thesis: Specification of resulting microstructure from additive manufacturing by Direct Laser Deposition of SS316L-Si on stainless steel base materials | |
| Credits: 30 | |
| Keywords: <i>Direct Laser Deposition</i> <i>Additive Manufacturing</i> <i>316L-Si stainless steel</i> <i>Microstructural investigation</i> <i>Hardness evaluation</i> | Number of pages: 77 + supplemental material: 7 Stavanger, 13.06.2018 |

Abstract

The purpose of this study was to investigate the macro- and microstructural constitution of Direct Laser Deposited (DLD) SS316L-Si on stainless steel base materials. The characterisation of the deposited material was carried out using light optical microscopy (LOM), scanning electron microscopy (SEM), energy dispersive X-ray spectroscopy (EDS), electron backscattered diffraction (EBSD), transmission- and scanning transmission electron microscopy (TEM and STEM) together with Vickers hardness measurements. The DLD process produced a crack-free, almost fully dense (porosity >99.5%) metallic part. The investigation revealed a duplex microstructure containing a primary austenitic matrix with secondary δ -ferrite interdendritic and along sub-grain boundaries. The δ -ferrite has formed due to segregation of ferrite stabilizing alloying elements and has helped voiding the material from hot-cracking during the thermal cycles. The austenitic dendrites have formed preferentially along $\langle 001 \rangle$ direction generating a solidification texture and large columnar grains along the thermal gradient being 5-10 times larger in longitudinal- than latitudinal direction. A microstructural variation exists throughout the samples with cellular- and columnar dendritic structures depending on solidification rate, with a localized heat-affect zone for each layer. While the process has formed a solid metallurgical bond to the base material in the case where the cleaning procedure was followed thoroughly, with a small heat-affect zone in the base material. Hardness values was found to be almost uniform in parallel- and normal to build directions, $\sim 170\text{HV}$. The elevated hardness compared to conventional manufactured SS316L is due to silicate nano-inclusions that generate large concentrations of dislocations and the uniform distribution of δ -ferrite facilitating the dislocation pile-ups. The investigation has also reveal defects such as entrapped gas which has created spherical pores, inter-track porosity along laser travel direction and segregation of alloying elements. Various solutions to improve the defects has been discussed so the study may serve as a guide to improve the process parameters.

Acknowledgments

A sincere acknowledgment is given to Professor Vidar Hansen who has been my faculty supervisor during this thesis. You have contributed greatly with knowledge and encouragement during the process of completing my work. A genuine acknowledgment is also to be given to Wakshum Mekonnen Tucho for your preliminary instructions and guidance on the use of the electron microscopes. Appreciation is also due to my external supervisor Geir Tandberg, previously of TechnipFMC Subsea for making this work possible and supplying the material. Lastly, gratitude is also shown towards the University of Stavanger where most of the work has been done. By supplying an office to work from and allowing me to use the equipment during the late hours, the University has allowed for the work to be done at my own pace and premises which is appreciated.

Directory of abbreviations

| | |
|-----------|---|
| AM | Additive Manufacturing |
| ASTM | American Society for Testing and Materials |
| BCC | Body-Centred Cubic |
| CAD | Computer Aided Design |
| DLD | Direct Laser Deposition |
| EBS | Electron Backscattered Diffraction |
| EDAX | Energy Dispersive Analysis of X-rays |
| EDS | Energy Dispersive X-ray Spectroscopy |
| FCC | Face-Centred Cubic |
| HAZ | Heat-Affected Zone |
| LOM | Laser Optical Microscope |
| LTD | Laser Travel Direction |
| N/A | Not Available |
| N1-15 | Numbering of the deposited layers |
| SAD | Selected Area Diffraction |
| SDAS | Secondary Dendritic Arm Spacing |
| SEM | Scanning Electron Microscope |
| SS304 | Type 304 stainless steel |
| SS316L-Si | Low-carbon, high silicon type 316 stainless steel |
| TEM | Transmission Electron Microscope |
| Sample 1 | SS316L-Si deposited on SS304, cross-sectional cut w.r.t. laser travel direction. |
| Sample 2 | SS316L-Si deposited on SS304, plane cut w.r.t. laser travel direction. |
| Sample 3 | SS316L-Si deposited on SS316L, cross-sectional cut w.r.t. laser travel direction. |
| Sample 4 | SS316L-Si deposited on SS316L, plane cut w.r.t. laser travel direction. |

TABLE OF CONTENTS

| | |
|---|-----|
| ABSTRACT..... | I |
| ACKNOWLEDGMENTS..... | II |
| DIRECTORY OF ABBREVIATIONS..... | III |
| CHAPTER 1 INTRODUCTION..... | 1 |
| CHAPTER 2 LITERATURE STUDY | 3 |
| 2.1 ADDITIVE MANUFACTURING..... | 3 |
| 2.1.1 <i>A brief History</i> | 3 |
| 2.2 DIRECT LASER DEPOSITION..... | 4 |
| 2.2.1 <i>The deposition process</i> | 4 |
| 2.2.2 <i>Powder material</i> | 5 |
| 2.2.3 <i>Benefits and Limitations</i> | 5 |
| 2.3 STAINLESS STEEL | 7 |
| 2.3.1 <i>Type 316L</i> | 7 |
| 2.3.2 <i>Type 304</i> | 8 |
| 2.4 MICRO- AND MACROSTRUCTURE..... | 8 |
| 2.4.1 <i>Influence of alloying elements</i> | 8 |
| 2.4.2 <i>Iron-Carbon equilibrium diagram</i> | 11 |
| 2.4.3 <i>Iron-Chromium equilibrium diagram</i> | 12 |
| 2.4.4 <i>Ternary phase diagram</i> | 13 |
| 2.4.5 <i>Schaeffler diagram</i> | 14 |
| 2.4.6 <i>Solidification of δ-ferrite</i> | 15 |
| 2.4.7 <i>Segregation of alloying elements</i> | 16 |
| 2.4.8 <i>Heat Affected Zone</i> | 16 |
| 2.5 STRENGTHENING MECHANISMS..... | 18 |
| 2.5.1 <i>Dislocations</i> | 18 |
| 2.5.2 <i>Solid solution strengthening by interstitial- and substitutional atoms</i> | 19 |
| 2.5.3 <i>Refinement of grain size</i> | 19 |
| 2.5.4 <i>Solidification</i> | 20 |
| 2.6 EQUIPMENT FOR CONSTITUTIONAL ANALYSIS | 22 |
| 2.6.1 <i>Light optical microscope</i> | 22 |
| 2.6.2 <i>Electron microscope</i> | 23 |
| 2.6.3 <i>Scanning Electron Microscope</i> | 23 |
| 2.6.4 <i>Transmission Electron Microscope</i> | 28 |
| 2.6.5 <i>Hardness measurement</i> | 31 |
| CHAPTER 3 THE MATERIAL | 32 |
| 3.1 DIRECT LASER DEPOSITED MATERIAL..... | 32 |
| 3.2 POWDER MATERIAL – METCOCLAD SS316L-Si | 33 |
| CHAPTER 4 EXPERIMENTAL PROCEDURES..... | 35 |
| 4.1 SAMPLE EXTRACTION | 35 |
| 4.2 CONSTITUENT ANALYSIS | 36 |
| 4.2.1 <i>Light Optical Microscope</i> | 36 |
| 4.2.2 <i>Scanning Electron Microscope</i> | 38 |
| 4.2.3 <i>Electron Backscattered Diffraction</i> | 39 |
| 4.2.4 <i>Transmission Electron Microscope</i> | 39 |
| 4.2.5 <i>Hardness evaluation</i> | 40 |
| 4.2.6 <i>Cross-sectional density calculation</i> | 41 |
| CHAPTER 5 EXPERIMENTAL RESULTS AND DISCUSSION | 42 |
| 5.1 MICROSTRUCTURE..... | 42 |
| 5.1.1 <i>General macro- and microstructure</i> | 42 |

| | |
|---|-----------|
| 5.1.2 Fusion to base material..... | 48 |
| 5.1.3 Quantitative analysis of microstructure | 48 |
| 5.1.4 Secondary phase δ -ferrite..... | 51 |
| 5.1.5 Dislocations | 56 |
| 5.1.6 Silicate inclusions..... | 57 |
| 5.2 DEFECTS | 59 |
| 5.2.1 Element segregation | 59 |
| 5.2.2 Pores and voids | 61 |
| 5.3 HARDNESS EVALUATION | 63 |
| 5.4 FURTHER RESEARCH..... | 66 |
| CHAPTER 6 SUMMARY AND CONCLUSIONS..... | 67 |
| CHAPTER 7 REFERENCES | 70 |
| APPENDIX A IMAGEJ PROCEDURE | I |
| APPENDIX B MICROSTRUCTURAL CONTRASTS | II |
| APPENDIX C FUSION BOUNDARY AND HAZ | IV |
| APPENDIX D HARDNESS DATA | V |

CHAPTER 1

INTRODUCTION

Over the last few decades, additive manufacturing (AM) has experienced a significant increase in attention from the industry and researchers from around the world leading to a remarkable evolution from initially enabling only poor prototyping [1] to now producing fully functional parts for everything from medical [2] to the aerospace [3] and automotive industry [4], into oil and gas industry [5] and even fabricating functional tools in space [6]. Today there exists several varieties of AM, while one of the contemporary techniques for producing near-net shape parts is material deposition by applying a laser beam. Within this category there is several different techniques such as laser engineered net shaping® (LENS) [7], laser metal deposition shaping (LMDS) [8], laser solid forming (LSF) [9] and direct laser deposition (DLD) [10]. AM by applying the method of DLD can directly fabricate, repair, add strength enhancing- and fully dense metallic features with complex geometry to existing small- and large-scale parts. In comparison to traditional manufacturing, additive manufacturing with DLD is advantageous in the applied technology and is competitive in terms of economics. By applying highly developed laser- and machining technology DLD can customize and repair pre-existing parts, generate components with geometry beyond the capability of conventional manufacturing, reduce material wastage significantly by directly depositing the material with fine precision which reduce the need of costly equipment and machining [11, 12]. DLD also allows for designing components with specifically refined microstructures to achieve desired properties which is not possible with conventional manufacturing [13, 14].

The AM process utilizes layer-by-layer fabrication of previously generated computer aided design (CAD) models. By applying lasers, such as Nd:YAG (Neodymium-doped Ytterium Aluminium Garnet) diode lasers, a concentrated melt pool is produced on a base material surface which is injected by a high pressurized gas carrying powder material used to generate the metallic feature. During the process, the laser moves in a raster specified in computer aided manufacturing (CAM) software while the powder material is continuously fed in the rapidly evolving melt pool. High alloyed stainless steels such as 316L contain larger amounts of chromium, molybdenum and nickel which gives it impeccable corrosion resistance, good ductility, high strength and good weldability at relatively low cost. This

makes the material highly applicable for the automotive, oil-, gas- and refinery industry, chemical plants, biomedical, within construction and for nuclear reactors [15-17].

Today the AM of metal parts are under thorough investigation as the technique of layer-by-layer manufacturing generate specific macro- and microstructures, defects and phases that are different from conventional manufacturing of the same materials. This makes it necessary to formulate relationships between the multiple process parameters and the resulting microstructure and correlating mechanical properties before the technology are applied to crucial structural parts.

Saeidi et al. [14] studied the microstructure of applying laser melting to SS316L generating a hardened single-phase austenitic structure with molybdenum enriched sub-grain boundaries with large dislocation concentrations and dispersed silicate nano-inclusions. While Dutta et al. [15] produced almost fully dense SS316L parts with a homogenous microstructure. The study showed that scan speed has a major influence on the microstructural morphology. Yadollahi et al. [13] studied the effect of process time interval followed by heat treatment of DLD SS316L and showed that longer local time intervals resulted in higher cooling rates and finer microstructure. While pores and weaker metallurgical bonds was found to be predominant in the last layers due to reduced laser penetration. On the other hand, the relatively high cooling rates has been shown to have an adverse effect on layer adhesion and give inter-track porosity [18, 19].

The aim of this thesis is to carefully and thoroughly study the macro- and microstructural evolution of DLD SS316L-Si metal powder on SS304 base material without proper cleaning procedure, and on SS316L base material with proper cleaning procedure. Study the microstructural variations in the layers, solidification textures, investigate the presence of secondary phases, defects, hardness and fusion to base materials.

CHAPTER 2

LITERATURE STUDY

2.1 Additive Manufacturing

Additive manufacturing, AM, is a term given to describe all processes which is based upon generating three-dimensional objects by adding material layer-upon-layer. The common denominator for AM is the use of computers, software to generate 3D models by computer aided design (CAD), lasers and inert environment.

The 3D CAD model is converted to an STL-file. The file is sliced into discrete layers which represent each layer thickness. When this is done, computer aided manufacturing (CAM) software integrated into AM equipment reads the file and starts to add successive layers of the process material. Depending on the geometry and the manufacturing process, there may be a need to specify support material for surfaces with overhang angle larger than 45° to avoid deformation of the shape.

AM is diverse and can be used in different applications as:

- Concept visualization
- Rapid Prototyping
- To generate parts with intricate and complex geometry
- Medical application
- Manufacturing of structural parts

2.1.1 A brief History

The thought of producing a 3-dimensional object layer by layer, came long before the idea of additive manufacturing. In 1902, Peacock submitted a patent for a laminated horse shoe [20]. 50 years later, a Japanese man, Kojima, published research demonstrating the benefits of layered manufacturing [21].

In 1987 the Stereolithography Apparatus 1, SLA-1, marks the first ever commercialized rapid prototyping system in the world. This process is based on curing a photo-polymer resin by laser. The object is created on a platform which is submerged one layer thickness into a chamber containing the resin. A laser solidifies the first layer, before the platform is lowered another thickness into the chamber, and the process is repeated until the object is complete.

Over the years, additive manufacturing processes has evolved, and new material has come into play. Polymers, ceramics, composites, food, biological material, metals and even rock [22]. And the newer AM techniques such as Selective Laser Sintering (SLS), Selective Laser Melting (SLM) and Direct Laser Deposition (DLD) among others, makes it possible to create not only prototypes, but also fully functional and structural parts which in some cases has better mechanical properties than conventionally manufactured parts due to their refined microstructure [23].

2.2 Direct Laser Deposition

2.2.1 The deposition process

Direct laser deposition is the process of adding material by spray deposition to pre-existing material and parts, similar to cladding. The process is used to create free-formed components and repair previously damaged parts. And can also be used to add strengthening features to casted and forged structural components. As for other AM techniques all the required data comes in a predefined CAD-model.

The deposition process is executed in a controlled environment to minimize any atmospheric influence on the end result, similar to welding where a shielding inert gas is used. A high-power laser generates a small melt pool at the base material surface and a nozzle inject powdered material directly into the focused laser beam. This generates a weld bead and by the addition of multiple layers a 3-dimensional feature is generated. Figure 1 is a schematic illustration over the DLD process. As a consequence of a small laser spot size and the speed which the laser travels, the deposited melted material experiences a cooling rate of 10^3 - 10^4 K/s [24]. This result in a very localized and small heat-affected zone in the fusion between base- and the deposited material, which also occurs between each layer in the build. The cooling rates has an additional large influence on the end result, generating a refined microstructure [10].

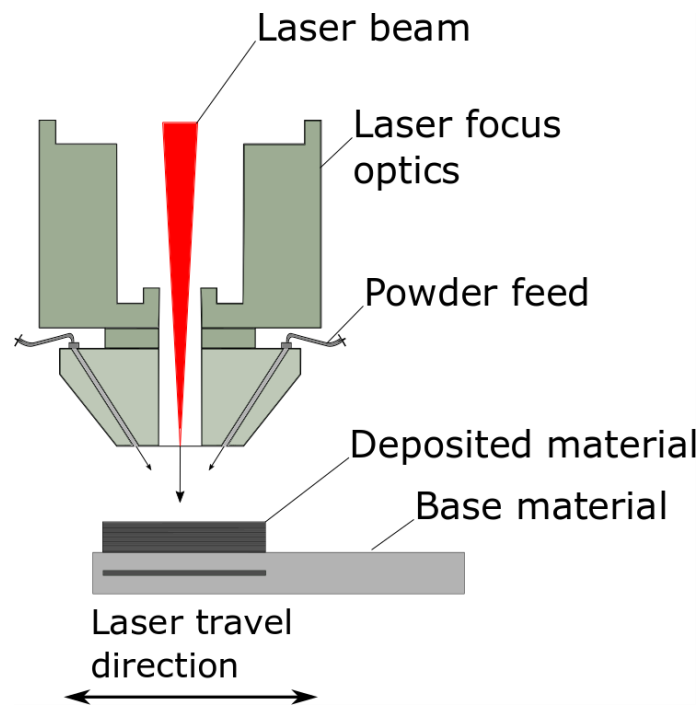


Figure 1: Schematic illustration over the Direct Laser Deposition process, the focus optics, powder feeder and base material.

2.2.2 Powder material

Depending on the type of metal or the alloy, the metal powder comes in different size and shapes and is produced using a large variety of processes. The requirement for repeatable processes in additive manufacturing makes the geometry, size and chemistry of the powder particles critical for successful part production. There is also a requirement for the powder material to be stable in a molten pool [25].

The powder particle size range generally from 20-150 μm . In this size range, the material can be delivered with a gas flow and will easily transform to a liquid state in the melt pool.

2.2.3 Benefits and Limitations

The DLD process involves a complex interaction between the laser beam and the metal powder. This interaction can lead to different kinds of unwanted constituents in the material, such as residual stresses due to high cooling rates, binding defects between the layers leading to layered voids and entrapped gas forming spherical pores [26]. Also element segregation and carbide formation can occur due to the nature of continuous reheating of the material.

As expected from high cooling rates, residual stresses will occur in the material. This can cause development of crack formations and further propagation of the cracks which eventually leads to failure of the component [27]. As the melt pools are formed, gas may get

enclosed in the layers during solidification. This gas can come from contaminants, turbulent impact between particles that generate gases, gases contained inside the powder-particles or vaporization of alloying constituents. The gas will generate spherical voids if it does not reach the material surface before the material has solidified. The interface between two layers may also contain voids, generated due to lack of fusion between them. These voids tend to have a more irregular and elongated shape [26].

Other limitations to the DLD process is poor resolution and rough surface finish. With it being difficult to achieve accuracy better than 250 μm and surface roughness less than 25 μm [28]. The deposition rates are fairly low with 25-40 g/h, which makes the build time long for larger components. It is possible to achieve better deposition rates on the expense of surface finish. And similar it is possible to achieve better accuracy with reduced laser beam spot size and deposition rates. Changes in the input power for the laser and scan speed will influence the microstructure, and optimal setting must be found by trade-offs between deposition rate, accuracy, surface finish and microstructure.

The benefits of DLD are many, and already in this stage of the development, the benefits outweigh the disadvantages in a lot of areas. At this time in our history, a products lifespan is relatively short due to rapid improvements made in all fields every year. This suits DLD, and other AM techniques, as the time from design to the part being available on market can be shortened to a fraction of what conventional machining can do. Weight reduction optimization is possible to some degree by removing unnecessary material from the part in the CAD model, a pre-printing preparation. DLD does not have the same unlimited possibilities for the geometry as other AM techniques, such as powder bed fusion, as DLD has a larger requirement for support structures since the powder material is deposited directly onto the surface material. This still allows for internal structures to be made such as pipe channels, ducts, support columns or other desired features. Expensive and extensive tooling is not needed, the part can be printed and directly used if the part does not have any aesthetically function.

DLD present the capability of exceptional control over the microstructure. With the ability to change material composition and solidification rate by changing powder content and process parameters, this makes the mechanical properties of DLD parts proportionate to conventional produced parts, and in some cases much improved [23]. With continuous research on the effects of process parameters, in some years the process will open up the

possibility of generating parts with specific mechanical-, corrosive- and conductive properties on demand.

DLD can be utilized for effectively repairing defective and service-damaged components. To deposit thin layers of corrosion and wear resistance material to components to improve their performance and lifetime. Or to adding features and material to existing structural parts to improve their performance characteristics [28]. Material wastage during production is also reduced significantly with DLD. The laser is non-pollutive and the process is environmentally friendly and allows for green production, thus DLD is suitable for the sustainable development that is currently ongoing [29].

2.3 Stainless Steel

2.3.1 Type 316L

American Iron and Steel Institute graded 316L stainless steel is a low carbon austenitic steel. SS316L has a similar chemical composition as SS304, with less carbon and the addition of molybdenum which gives the material excellent corrosion resistance properties, even in environment containing chlorides [30]. Table 1 gives the chemical composition of the material.

Table 1: Chemical composition of 316L grade stainless steel.

| | C | Mn | Si | P | S | Cr | Ni | N | Mo | Fe |
|---------------|------|------|------|-------|------|-------|-------|------|------|---------|
| Min. [wt%] | - | - | - | - | - | 16.00 | 10.00 | - | 2.00 | Balance |
| Max. [wt%] | 0.03 | 2.00 | 0.75 | 0.045 | 0.03 | 18.00 | 14.00 | 0.10 | 3.00 | Balance |

Its chemical composition makes the material excellent for use in weldments, cladding and additive manufacturing as it reduces the possibility of sensitization. The material exhibits good machinability even though it has a tendency to work harden. Good ductility, weldability and toughness, even down to cryogenic temperatures. The creep, stress to rupture and tensile strength at elevated temperatures is also higher compared to other chromium-nickel stainless steels. Because of these properties the material is seen in use in a wide range of applications; from onshore to offshore constructions, in marine environments all the way into

the food industry and in medical implants. For conventionally forged SS316L the average hardness value is 155HV [31].

2.3.2 Type 304

The type 304 stainless steel is a versatile and widely used stainless steel, it may be referred to as 18/8 which is a name derived from the chemical composition of 18wt% chromium and 8wt% nickel. In Table 2 the chemical composition of 304 is given. The hardness value for SS304 can be up to 260HV [32].

Table 2: Chemical composition of 304 grade stainless steel.

| | C | Mn | Si | P | S | Cr | Ni | N | Fe |
|---------------|------|------|------|------|------|-------|-------|------|---------|
| Min. [wt%] | - | - | - | - | - | 17.50 | 8.00 | - | Balance |
| Max. [wt%] | 0.07 | 2.00 | 1.00 | 0.05 | 0.03 | 19.50 | 10.50 | 0.11 | Balance |

SS304 has good corrosive properties, though it is prone to pitting and crevice corrosion in chloride environments and may experience stress corrosion cracking (SCC) at temperatures above 60°C. The grade SS304 is suitable for welding as the material is non-hardenable during cooling and require no pre- or post-weld heat treatment [33].

2.4 Micro- and macrostructure

The microstructure has a direct influence on some of the mechanical properties and physical behaviours of the material. The features in material are characterized by different phases, its locations and defects. And the final structural configuration at room-temperature depends mainly on the alloying elements, solidification conditions and post-processing heat- and mechanical treatment [34].

2.4.1 Influence of alloying elements

Austenitic steels are susceptible to different phase transformations depending on temperature, cooling rate and alloying elements. The high amount of alloying elements in SS316L slow down the ferritic transformation to a point where the transformation might be completely repressed, then the material preserve the face-centred cubic austenite at room temperature [35].

Austenitic steels do not undergo a ductile-brittle transition, which causes problem in ferritic steels. The austenite structure is also less exposed to σ -phase. The σ -phase is one of the main reasons for the degradation of the stainless steels' properties, its mechanical properties, weldability and corrosion resistance [36].

If chromium is added alone to a plain carbon steel the solution will favour the formation of ferrite. However, when nickel is introduced it retards the austenite-to-ferrite transformation. Nickel, together with chromium and molybdenum is the alloying elements which give the 316L stainless steels its superior corrosive properties. The chromium improves the corrosion resistance by forming a thin and stable oxide film on the material surface. While the molybdenum increase the resistance to crevice- and pitting corrosion [35]. The nickel helps facilitate the passivation of the surface, thus controlling the pitting resistance [37].

The conventional chemical composition of the SS316L, previously given in Table 1, is presented again in Table 3 to ease the reading of the rapport. All the elements in the alloy are added to influence the material in a specific way, thus in the following a short description of each elements role in the solution is given [38]:

Table 3: Chemical composition of 316L grade stainless steel.

| | C | Mn | Si | P | S | Cr | Ni | N | Mo | Fe |
|---------------|------|------|------|-------|------|-------|-------|------|------|---------|
| Min. [wt%] | - | - | - | - | - | 16.00 | 10.00 | - | 2.00 | Balance |
| Max. [wt%] | 0.03 | 2.00 | 0.75 | 0.045 | 0.03 | 18.00 | 14.00 | 0.10 | 3.00 | Balance |

- Carbon: The addition of carbon to iron helps the material gain strength and hardness by its substitutional and interstitial placement in the lattice. Carbon is also a strong austenite former.
- Manganese: In order to improve the ductility at elevated temperature manganese is added. This element also helps stabilize the austenite at lower temperatures and increase the solubility of nitrogen in the material.
- Silicon: Silicon benefits the formation of ferrite. Increase the materials resistance to oxidation and prevent carburising at elevated temperatures.
- Phosphorus: Phosphorus is added to improve the machinability of the material. This element has a detrimental effect on the corrosion resistance and increase the

possibility of formation of cracks during welding, thus it is critical to control the amount added to the solute.

- Sulphur: Similar to phosphorus, sulphur increase the machinability when added in small amounts. It also has a detrimental effect on corrosion resistance and weldability.
- Chromium: The addition of chromium, as mentioned earlier, benefits the material by making it highly corrosion resistant. Chromium is a ferrite stabilizer.
- Nickel: Nickel is a beneficial element, together with the improvement in ductility it also gives the material toughness and favours the formation of austenite. In 316L stainless steel, the nickel content as given in the table lies between 10-14wt%. In this range the nickel content makes the material more prone to stress corrosion cracking [39].
- Nitrogen: Nitrogen actively promote the formation of an austenitic microstructure. It significantly increases the resistance to pitting corrosion in addition with molybdenum.
- Molybdenum: This element strongly promotes a ferritic microstructure. As previously mentioned, it significantly improves the corrosion resistance, both pitting and crevice corrosion. And to some extent increase the mechanical strength of the material.

Due to the amount of chromium and carbon in the 316L stainless steel, and the method which the DLD process deposits material layer-by-layer, it can lead to formation of carbides. If the material is held at a temperature within the range of 500-800°C it will lead to rejection of carbon from the solution. The carbon will then favour binding with the surrounding material and form Cr_{23}C_6 carbides. Since most of the carbon is found near the grain boundaries, the carbides will precipitate there. Because carbon can bind large amounts of chromium, one of the two alloying elements giving the material its impressive corrosive properties, the surrounding area will get depleted and may thus be susceptible to intergranular corrosive attacks. There are several ways to stabilize this:

- Reheating the part after the DLD process. Heating to 950-1100°C allows for the Cr_{23}C_6 to dissolve followed by rapid quenching.
- Reduction of carbon content to below 0.03wt%.
- Increase amount of molybdenum will considerably increase the time for sensitization.
- Introduce stronger carbide-forming elements, such as niobium and titanium. The carbon will then preferentially combine with them and thus lessen the possibility for chromium carbides to nucleate [35].

The alloying constituents' microstructural influence can be conveniently represented by diagrams such as the Iron-Carbon equilibrium-, Iron-Chromium equilibrium- and the Schaeffler diagram.

2.4.2 Iron-Carbon equilibrium diagram

The iron-carbon phase diagram is a highly important binary alloy system, the diagram provides an invaluable foundation for the understanding of the microstructural evolution before, during and after solidification of an iron-carbon alloy. The solidification behaviour of the 316L stainless steel after the DLD process is influenced by the diagrams basic features.

The iron-carbon phase equilibrium diagram can be seen in Figure 2. As seen in the figure, the diagram contains multiple critical points which must be considered. A_1 , the eutectoid reaction, which occur at a temperature of 723°C is the upper limit of the ferrite-cementite phase field. At A_2 , the so-called Curie point, the ferritic iron change from ferromagnetic to paramagnetic and happen at 769°C for pure iron. A_3 marks the line where the ferritic structure transforms to austenitic. A_4 marks where the α -ferrite change to δ -ferrite. It's worth noting that there are no physical differences between the two phases, the δ is used to represents a high-temperature formation of the ferrite [35].

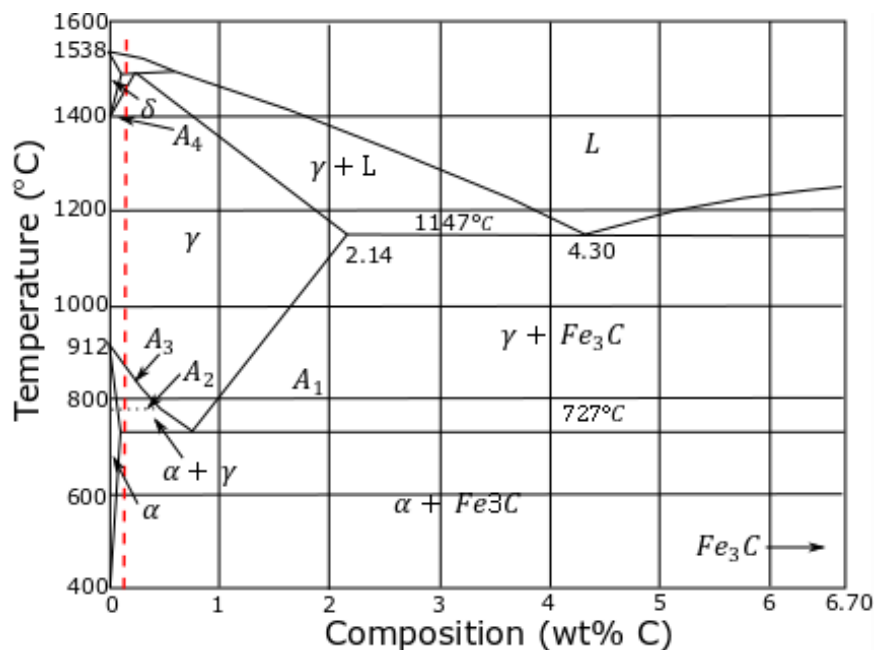


Figure 2: Iron-carbon phase equilibrium diagram. Red and vertical line is indicating 0.03wt% carbon [34].

The red and vertically dashed line in the Figure 2 represents the carbon content of 0.03wt% for a pure iron-carbon alloy. From the liquid state some of the material transforms to δ -ferrite at about 1535°C to form a liquid + δ -ferrite. At 1493°C the solution undergoes another

transformation to δ -ferrite + austenite before an amount of the austenite transforms to ferrite again at A_3 . The material keeps this duplex phase until A_1 where the remaining austenite transforms to cementite, Fe_3C .

The course of phase transformation described will occur if the material is a pure iron-carbon alloy of 0.03wt% carbon. The alloying elements in SS316L hinders these transformations to some extent, as can be represented by the iron-chromium equilibrium diagram.

2.4.3 Iron-Chromium equilibrium diagram

The iron-chromium equilibrium diagram is given in Figure 3, with a red dashed line indicating the chromium content of SS316L. The figure shows how a chromium content over 13wt% give a microstructure containing only ferrite over the whole temperature range. The ferrite here is the previously described δ -ferrite, since the chromium allow the phase to have a continuous existence from it occurs and all the way down to room temperature.

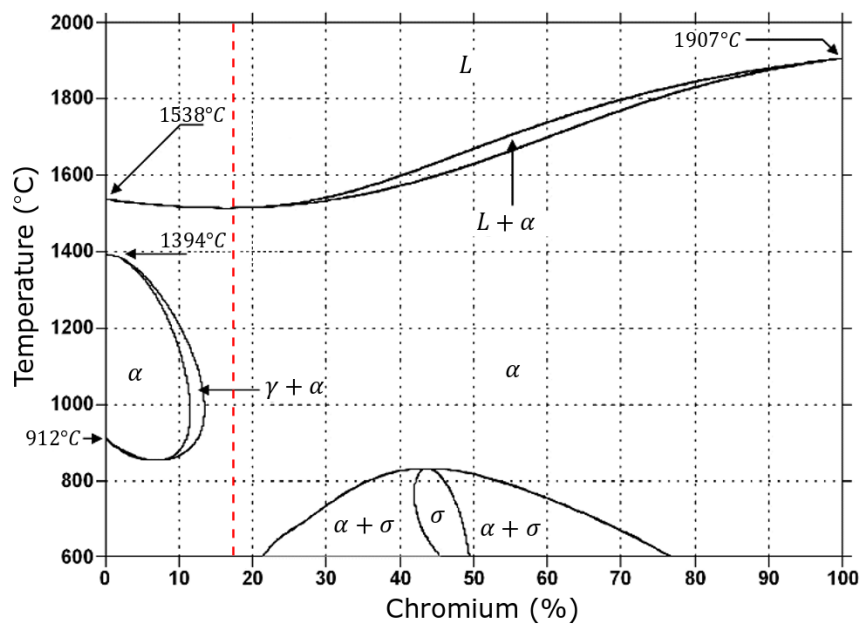


Figure 3: The iron-chromium equilibrium diagram, with a dashed red line indicating the chromium content of SS316L [40].

Figure 4 show the effect of adding carbon to the binary alloy, which extends the austenite-loop into higher chromium content, the dashed red line indicates the chromium content of SS316L. As can be seen in the figure it also widens the ferrite + austenite phase. The addition of nickel further expands the austenite-loop until at about 8wt% nickel which allows for the austenitic microstructure to remain down to room temperature. Aside from the possibility of forming chromium carbides as previously mentioned by introducing carbon into the alloying

mixture, Figure 4 show that above ~7.5% chromium other carbides can be formed. In 316L stainless steel, where the carbon content lies around 0.03wt% and chromium are above 16wt% the carbide $K_1=M_{23}C_6$ is the most significant carbide formed. 'M' represent various metal atoms. These carbides precipitate preferentially along the grain boundaries and intragranular where they form along dislocations. The carbides exists from below ~900°C down to room temperature [35].

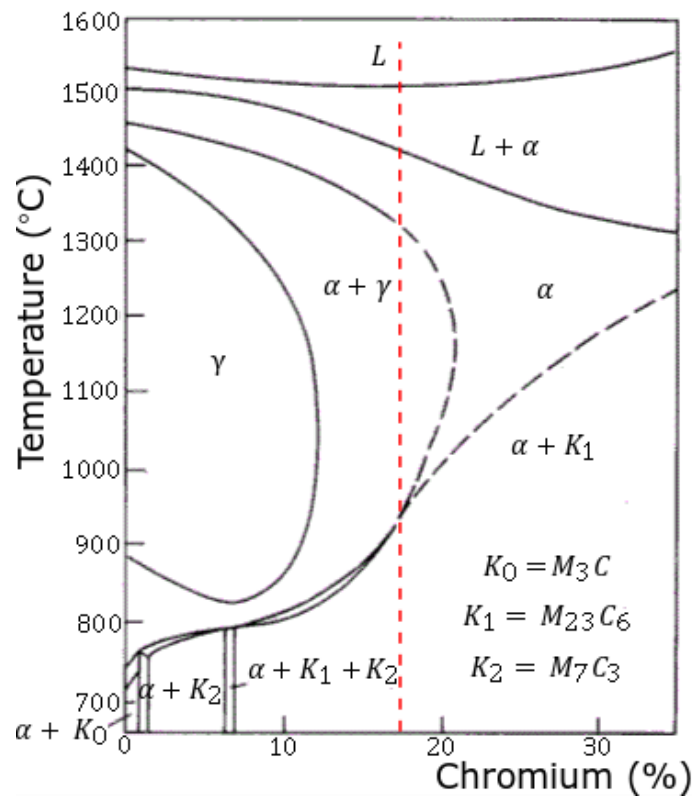


Figure 4: The iron-chromium equilibrium diagram with expanded loops due to addition of carbon, with a dashed red line indicating the amount of chromium in SS316L [35].

2.4.4 Ternary phase diagram

As the SS316L is a high alloyed stainless steel, with the three main alloying constituents iron, chromium and nickel. The ternary phase diagram is beneficial for understanding the solidification behaviour and the phase evolution. Figure 5 show an excerpt from a ternary system with ~68% iron. The vertical, dashed red line indicates the compositions of nickel and chromium in SS316L. As the line indicate, the phase evolution is in the proximity to both the peritectic transformation $L \rightarrow L + \gamma \rightarrow \gamma$ and ternary peritectic transformation $L \rightarrow L + \gamma + \delta \rightarrow \gamma$. The complete description of the solidification process and the result at room temperature will be given in sub-chapter 2.4.6

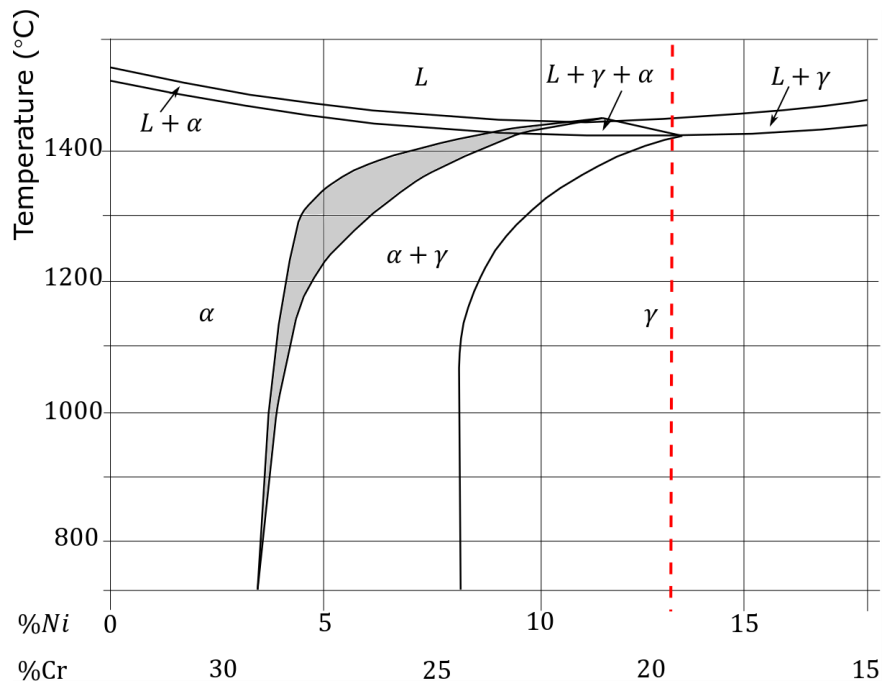


Figure 5: Ternary phase diagram containing primary alloying elements in SS316L. Excerpt at ~68% iron. Dashed red line approximates the phase evolution of SS316L [41].

2.4.5 Schaeffler diagram

An invaluable way of understanding the effect the alloying elements have on the microstructure of a nickel-chromium based stainless steel such as 316L is the Schaeffler diagram, given in Figure 6.

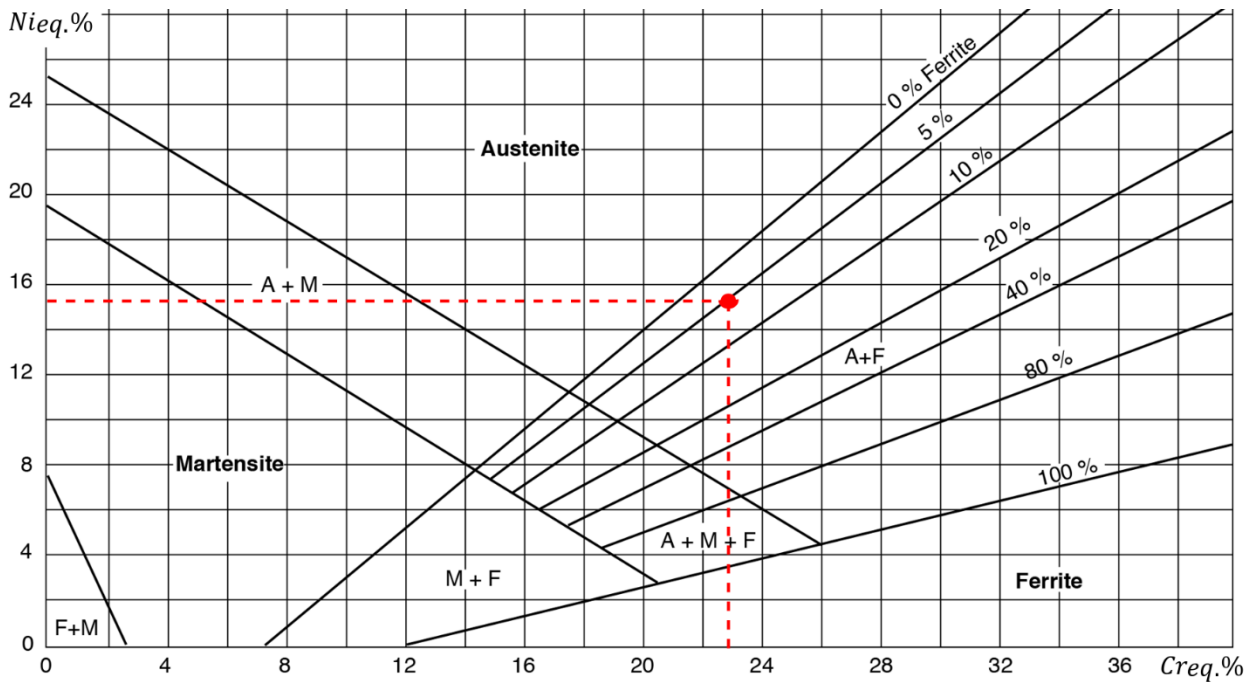


Figure 6: Schaeffler diagram. Intersection of the dashed red lines indicate the chromium- and nickel equivalents of 316L-Si stainless steel powder used to produce the studied components [42].

The benefits of the Schaeffler diagram is that it plots the material composition at room temperature with respect to austenite, ferrite and martensite by the use of the nickel- and chromium equivalents given in equation (1) and (2). The equivalents use the weight percentage of each elements [43, 44].

$$Cr \text{ equivalent} = Cr + Mo + 1.5Si + 0.5Nb \quad (1)$$

$$Ni \text{ equivalent} = Ni + 0.5Mn + 30N + 30C \quad (2)$$

These equivalents consist of respectively ferrite- and austenite stabilizing elements and are empirically determined. The crossing point given in Figure 6 between the two red lines indicate the area which an average SS316L-Si microstructure should lie at room temperature; the values are calculated using the content of the constituents from the powder material used in the deposition process presented in Table 5 in sub-chapter 3.2 . As the point indicate, the microstructure for the SS316L-Si may contain ~5% δ -ferrite. This small amount of ferrite would be beneficial to the material as the ferrite can dissolve more sulphur and phosphorous than austenite, thus improve the resistance to the formation of sulphur containing liquid films along the grain boundaries and also reduce the possibility of cracking during solidification [45]. Welding and AM is analogous in many ways, and some of the literature from welding may be applicable to AM. To avoid solidification cracking during conventional welds, a chromium- to nickel ratio of minimum 1.48 has been proposed [46]. For AM the cooling rates are higher due to a small laser spot size and corresponding small weld pool, thus this ratio has been adjusted to 1.7 for laser melting processes [47]. The ratio of equivalents for the average SS316L-Si powder are 1.47, hence the DLD process may facilitate cracking during solidification.

2.4.6 Solidification of δ -ferrite

As the Schaeffler diagram and the ternary phase diagram indicate the possibility of δ -ferrite formation it is necessary to consider the transformation and how it is retained in the austenitic matrix. A study done by Takalo et al. [48] showed that the amounts of δ -ferrite present with a chromium/nickel equivalent ratio ≤ 1.48 will form from the remaining melt retained between growing austenitic cells or dendrites leading to eutectic solidification between the primary austenite and the secondary δ -ferrite. As this δ -ferrite is formed by the remaining melt there will exist a difference in composition between the two phases as a result of element

segregation during solidification. Element segregation will be revisited later in sub-chapter 2.4.7. As previously mentioned there are some benefits with the presence of δ -ferrite, but it can also have a negative effect on the corrosion properties due to the difference in alloy composition between austenite and δ -ferrite [49]. Takalo [48] also proposed different solidification types “Microstructural type A, B and C” for welding of stainless steels. Where type A gives cellular and dendritic ferrite formation with a soft appearance and correspond to a chromium/nickel equivalent ratio ≤ 1.48 . Type B gives a vermicular or lathy/needle morphology for the ferrite located at cellular or dendritic axes and lies between type A and C, while type C in relation to chromium/nickel equivalent ≥ 1.98 has a higher δ -ferrite content with lathy morphology mainly inside larger grains with an un-directional solidification structure.

2.4.7 Segregation of alloying elements

Initially in the liquidus state there remain a homogenous distribution of alloying elements. During solidification a variation in chemical composition will emerge. With a larger heat input the dendritic size increase which gives an increase in distance which the elements must diffuse to compensate for the fluctuation in composition. Heavier alloying elements such as molybdenum and chromium have slow kinetics due to a low diffusion rate in austenite, this seclude the elements from the solidification front in the melt pool and force the elements to stay in liquid phase. As the melt pool continue to solidify a steady increase in concentration of the various alloys in the melt occur until it has been segregated to the edges of the grains where it solidifies. The low diffusion rate of molybdenum keeps it from diffusing back into the solid to balance the inhomogeneous element distribution in the material, the same can occur for the other compositional elements in SS316L. This can destitute some areas while the dendritic- and grain boundaries become enriched in the alloying elements. The segregation will lead to a clear display of the dendrites within the grains after etching [50, 51].

2.4.8 Heat Affected Zone

In the process of adding material to a component through DLD the region on the component adjacent to the fusion zone will experience alteration of the microstructure and subsequently the mechanical properties due to the heat input, this is also the case for each layer. The region is called the heat-affected zone, or HAZ. Figure 7 is a schematic illustration over the heat-affected zone and its microstructural variation from the fusion zone and into the base material. The possible alterations to the material are:

- Recrystallization and grain growth due to the heat input. This will lead to a decrease in hardness, strength and toughness.
- Due to high cooling rates residual stresses may form in the HAZ during solidification. This may increase hot crack formation and can be found as localized brittle zones.
- Sensitization of the material, leading to carbide formation especially $M_{23}C_6$, which will render the material susceptible to intergranular corrosion [35].
- Formation of unwanted phases such as the brittle σ -phase which transforms from the δ -ferrite.
- There is also the possibility of higher susceptibility to stress corrosion cracking [52].

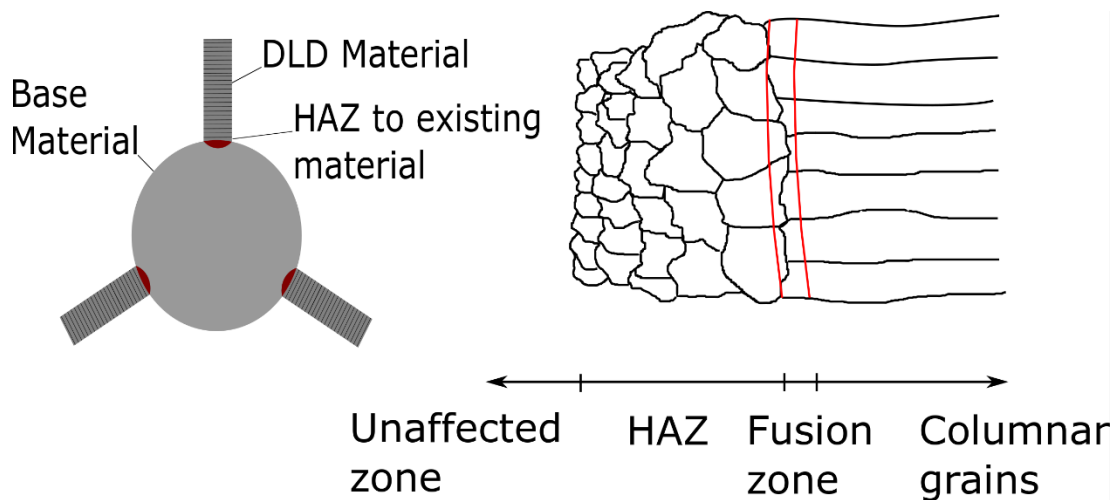


Figure 7: Schematic illustration over a base material with Direct Laser Deposited material. The fusion and heat-affected zones together with resulting microstructure is shown on the right side.

The heat-affected zone contains different regions. Immediately adjacent to a fusion zone there is a band of material heated above A_3 in the iron-carbon phase diagram in Figure 2. This gives a layer of coarse austenitic grains. As the distance from the fusion zone increase, the grain size will decrease sharply. This continues into a tempered region which stretches into the unaffected base material. HAZ appear as a result of thermal diffusivity into the surrounding material, thus it's a function depending on thermal conductivity of the material, density and specific heat capacity. If the thermal diffusivity is high, the HAZ will be reduced as the material cools faster. Regular structural 1%carbon-steel has a thermal diffusivity of $11.7\text{mm}^2/\text{s}$ while 304- and 316L graded stainless steel has almost a 3 times lower rate of $4.2\text{mm}^2/\text{s}$. Thus, it would be expected that the HAZ should extent to some degree into the base material [53], though this is highly dependent on the heat input.

2.5 Strengthening mechanisms

When a dislocation is allowed to move freely in the material, plastic deformation occurs due to slip. Therefore, understanding these linear crystalline defects, both edge and screw, and how to retard their movement is crucial to the mechanical properties of the material. The most important mechanisms that hinder movement of dislocation for a DLD manufactured 316L stainless steel are described in the following.

2.5.1 Dislocations

The dislocations cause lattice distortions in its immediate vicinity due to the nature of a dislocation being a line imperfection in the material. This distortion displaces the atoms from their normal lattice placement. There are two types of dislocations. An edge dislocation is an extra half-plane of atoms. This half-plane will move in response to a shear force. This results in atomic rearrangement in the lattice, or slip, perpendicular to the dislocation. A screw dislocation can be visualized as two planes in the material being displaced, by one atomic distance, relative to another due to a shear stress. This displacement generates a helical, a screw, extending through the crystalline material along a line. Or described with an analogy; the planes are connected in a manner similar to the levels of a spiralling parking ramp around the dislocation line [54]. The movement of a screw dislocation facilitates slip in the direction parallel to the dislocation. In both cases, the dislocation is the boundary between a slipped and a un-slipped region in the material.

The edge- and screw dislocations are extreme cases, and in most crystalline materials the dislocations do not occur as pure edge or pure screw, but rather as a combination of both. This is termed mixed dislocations and is schematically represented in Figure 8.

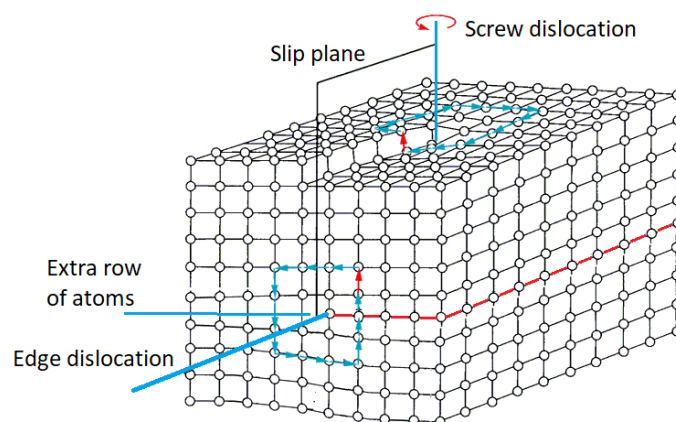


Figure 8: Schematic view of mixed dislocation. Red arrow indicating Burger's vector.

2.5.2 Solid solution strengthening by interstitial- and substitutional atoms

Solid solution strengthening involves introducing alloying elements to the lattice, which due to their relative size differences result in distortions in the matrix caused by tensile and compressive strains on the lattice. These distortions hinder the movement of dislocations and as a consequence increase the yield strength of the material.

The alloying elements can fill two different positions in the crystal structure, interstitial and substitutional. The interstitial placed atom is located in between the empty space throughout the matrix. These have greatest influence in a ferritic microstructure, as their location in the irregular octahedron interstice cause a tetragonal distortion. This has a dominant interaction with the shear component of a dislocations strain field. For austenitic microstructure the interstitial atoms form a regular octahedron, thus the atom behaves as a substitutional solute [35]. The substitutional atom is an atom different from the general matrix which occupy a vacant position in the lattice. Substitutional solute atoms create a spherically symmetric stress field in the matrix, thus it has no shear stress component to interact with the shear component from the dislocations as the interstitial does.

Increase in yield strength in the material due to solid solution strengthening can be described by the equation:

$$\Delta\sigma_{ss} = Gb\epsilon^{3/2}\sqrt{c} \quad (3)$$

Where G is the shear modulus of the material, b is the Burger's vector, ϵ is the strain in the lattice due to the solute given by $\epsilon = \Delta D/D$ where $\Delta D = D' - D$ is the difference in atomic diameter, D' represents a misplaced atom and D is for the general atomic diameter. While c denotes the concentration of solute atoms.

2.5.3 Refinement of grain size

The atomic mismatch, or grain boundaries in the crystalline material will work as an impediment to the movement of dislocations in the material due to the sudden change in crystallographic orientation. As a result, this demands energy from the dislocation as it needs to change direction when passing into the neighbouring grain. At high-misalignment angled grain boundaries dislocations may get piled up. This pile-up provokes the generation of new dislocations in the adjacent grains due to increased stress concentrations ahead of the slip plane [34].

According to the grain boundary strengthening theory, the grain size is the most important factor to the tensile strength. This is because a reduction in grain size leads to a higher count of grain boundaries to impede the movement of the dislocations [55]. The relationship between grain size and yield strength is expressed in the well-known Hall-Petch equation:

$$\sigma_y = \sigma_0 + \frac{k_y}{\sqrt{d}} \tag{4}$$

Where d is the average grain diameter, σ_y is the yield strength, σ_0 are a constant describing the friction stress required to move a free dislocation along a slip plane and k_y is a constant representing the slope of the plot $\sigma_y - d^{1/2}$ [35].

2.5.4 Solidification

As a consequence of the high cooling rates in DLD, the solidification of the melt pool happens quickly, this results in a complex microstructure comprised of a variety of dendritic structures generating equiaxed- and columnar grains depending on temperature gradient G , solidification velocity V_s and the cooling rate \dot{T} as illustrated in Figure 9.

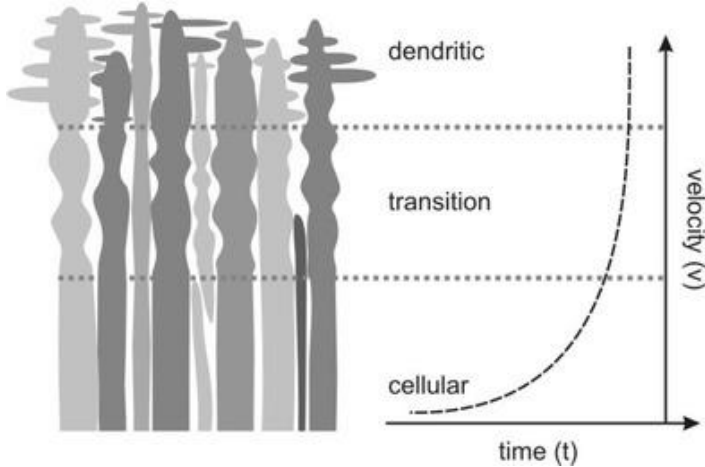


Figure 9: Illustration showing the dendritic development over time with respect to solidification velocity [56].

The deposited material experience initially a high temperature gradient in the melt pool which preserves a low solidification velocity. The slower solidification favours the growth of regular equiaxed cells perpendicular to the solid-liquid interface, as some of the heat flow is parallel to the previously deposited layer this can also initiate planar growth of the cells. As the temperature gradient decrease the solidification velocity increase which benefits further growth of the dendritic cells which eventually leads to side perturbations called secondary dendritic arms [56]. For cubic metals, such as FCC, the dendritic growth occurs

preferentially in the crystallographic direction $\langle 100 \rangle$. This happens as the $\{100\}$ family of planes has more voids for the atoms in the liquid to stick, than for example for $\{111\}$ planes which are more closely packed [57]. As the heat flow is highest perpendicular to the base material, the crystals with $\langle 100 \rangle$ direction along the heat flow grow at a higher rate than the surrounding material with a subordinate orientation for some degree of supercooling as illustrated in Figure 10. This happens as initially all dendrites, regardless of orientation, experience the same supercooling. As the solidification starts, the angled dendrites need to grow at a higher rate than the perpendicular ones as the angled has velocity components in two directions. Since they both experience the same solidification rate the non-angled dendrites will outgrow all others. The result is columnar grains consisting of multiple primary dendrite arms with $\langle 100 \rangle$ direction roughly parallel to the columnar direction and perpendicular to the base material. As the SS316L usually has a microstructure of single phased austenite, the secondary and tertiary arms of neighbouring dendrites can interconnect and lead to the formation of a continuous wall of primary dendrite arms [58].

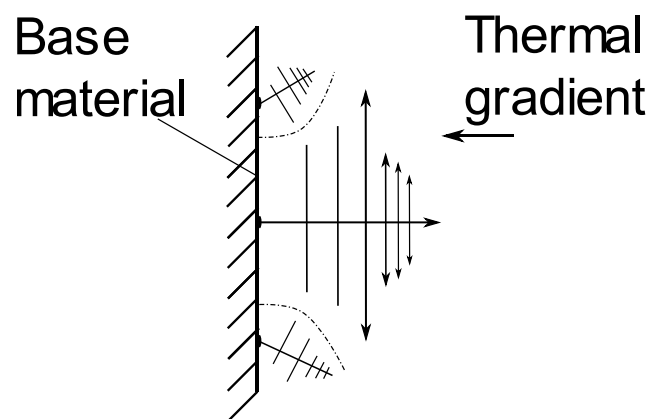


Figure 10: Schematic illustration over the dendritic growth during solidification of deposited material in the direction of thermal gradient.

For DLD which is a multipass process, the partially melted material in the previous layer can act as seed crystals for the new material resulting in epitaxial grain growth forming large columns stretching over multiple deposited layers [59]. These large columns with their preferential orientation can lead to a strong solidification texture in the material which will affect the mechanical properties generating anisotropy [34].

2.6 Equipment for constitutional analysis

To enable the possibility of microscopic investigation a whole arsenal of different tools and equipment is available. The equipment used in this thesis is described in the following:

2.6.1 Light optical microscope

The light optical microscope (LOM) uses optics and illumination as basic components of the system. For non-translucent materials such as metals, the microscope is used in a reflective manner. For the material to reflect as much light as possible, the surface must be ground and polished with the use of successively finer abrasives until it reaches a mirror-like surface finish. Further treating the material with a chemical reagent, an etching procedure which selectively attack and corrode material at different rates. The rate of corroding depends on crystallographic orientation, phase, and alloying elements. In turn these areas give contrast in the images due to differences in the how much light is reflected, thus revealing shape and size of grain boundaries, phases, inclusions, segregations, cracks and pores [34]. Figure 11 depict a schematic overview of a polished and etched surface, how it reflects light and the contrast it may give in the image.

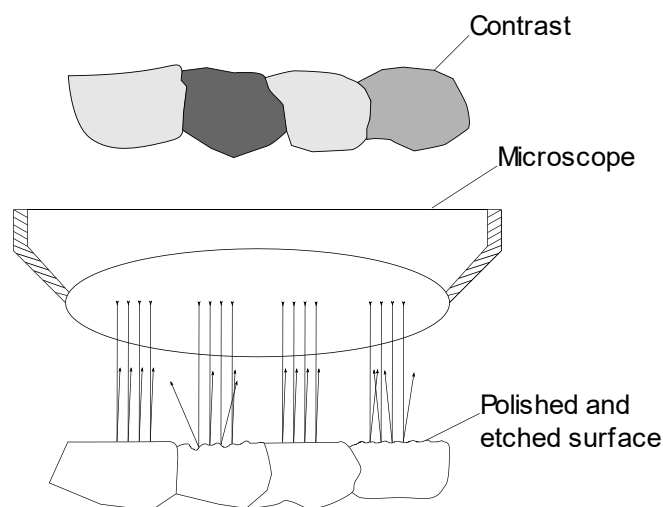


Figure 11: Schematic representation showing a polished and etched sample surface, how it reflects light and resulting contrast in micrograph.

The optical microscopes have a considerable limitation in using transmitted light as source for the observation. This restricts the magnification and resolving power of the microscope due to the wavelengths of light being 400-700 nm, and the numerical aperture of the objective lens. This restriction sets the maximum magnification in the range between 500x and 1500x [60]. In contrast electron microscopes has magnification possibilities exceeding 160.000x, while still maintaining good resolution.

2.6.2 Electron microscope

The major difference between an optical- and an electron microscope, is that the latter uses a beam of electrons to generate an image of the material. The benefit of using a high voltage accelerated electron, is the electrons wave properties which has a wavelength that is inverse proportional to its velocity. This can generate electrons with wavelength on the order of 0.003 nm, thus enabling the possibility of high magnification with good resolution [34]. The electron microscope uses a large set of magnetic lenses to focus the beam of electrons instead of optical lenses.

2.6.3 Scanning Electron Microscope

The scanning electron microscope (SEM) has a wide breadth of applicability for the study of solid materials. By focusing the beam of high-energized electrons onto the material surface it generates a variety of signals, due to the interactions between the electrons and the sample. The signals contain information about sample surface morphology, crystalline structure and orientation together with the chemical composition. Different detectors collect the signal data over a preselected surface area, this generates a 2-dimensional, high resolution image displaying the various and distinct discrepancies in the material.

After acceleration, the electrons travel at high velocity, thus carrying a considerable amount of kinetic energy. As the electrons interact with the material the energy is dissipated by deceleration in the sample, this interaction generates the signals, through both elastic and inelastic collisions. The signals consist of backscattered electrons, secondary electrons, diffracted backscattered electrons (EBSD) and photons in form of characteristic- (EDS) and continuum X-rays. For generating the images, backscattered – and secondary electrons are more commonly used. The backscattered electrons are valuable in depicting contrast between the different compositions in the multiphase sample, and the diffracted backscattered electrons generates important details about crystallographic orientations and the overall material structure. In contrast the secondary electrons are used to illustrate morphology and topology of the sample. While the characteristic X-rays are used to quantitative- and qualitative analyse the element composition of the sample surface [61].

Backscattered electrons are the result of elastic collisions between the electron beam and the material. As the incoming electron reach the first layers of atoms, its trajectory may be bent more than 90° in so-called Rutherford scattering, this happens due to the electron interacting with positive charged fields in the material originating from the atoms nucleus.

With two or more of these scatterings leading to a backscattered electron. The electron then leaves the sample surface in about the same direction it came from. Backscattered electrons may also be the result of multiple small angled scatterings. There is a direct correlation between the average atomic number and the amount of backscattered electrons [62]. These interactions are the cause of the good compositional contrast in the image. The secondary electrons are electrons originally in orbit around atoms in the sample that has been dislodged from the material after inelastic collisions, both between the primary electrons in the beam and the previously backscattered electrons on their way out. The secondary electrons have a low kinetic energy, which prevents electrons from deep inside the sample escaping the surface barrier of 2-6eV. This makes it only possible for electrons from the first layers of atoms to escape. Thus, resulting in good morphology and topology images. Figure 12 is a schematic example over the interactions between the primary electrons and the sample with the resulting backscattered- and secondary electrons.

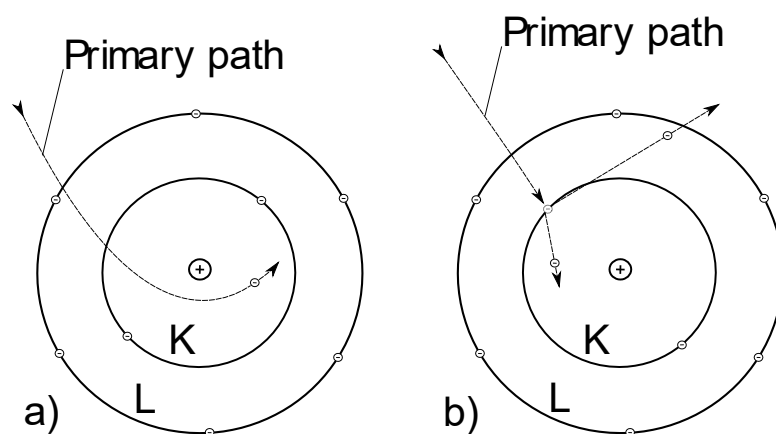


Figure 12: Schematic representation of interactions between the primary electron beam and the atoms in the sample resulting in; a) backscattered electron and b) secondary electron.

The characteristic X-rays are generated as photons with fixed wave-length are emitted from atoms in the sample. The incoming electron beam can collide inelastically with the electrons in the inner orbitals around the atom. This ionization excites the atom, making it obtain an unstable energy state. The excited atom returns to a lower energy state as an electron from an outer shell jumps down to the K- or L-shell, thus emitting a fixed wave-length photon to reduce the energy in its system, resulting in a signal corresponding to a specific element. As described by Moseleys law:

$$\lambda = \frac{K}{(Z - \sigma)^2} \quad (5)$$

Where λ is the wave length. Z is the atomic number. And K and σ are constants corresponding to specific X-ray emission lines such as K, L or M [63].

Figure 13 is a schematic over the interaction volume for each of the signals generated in the sample.

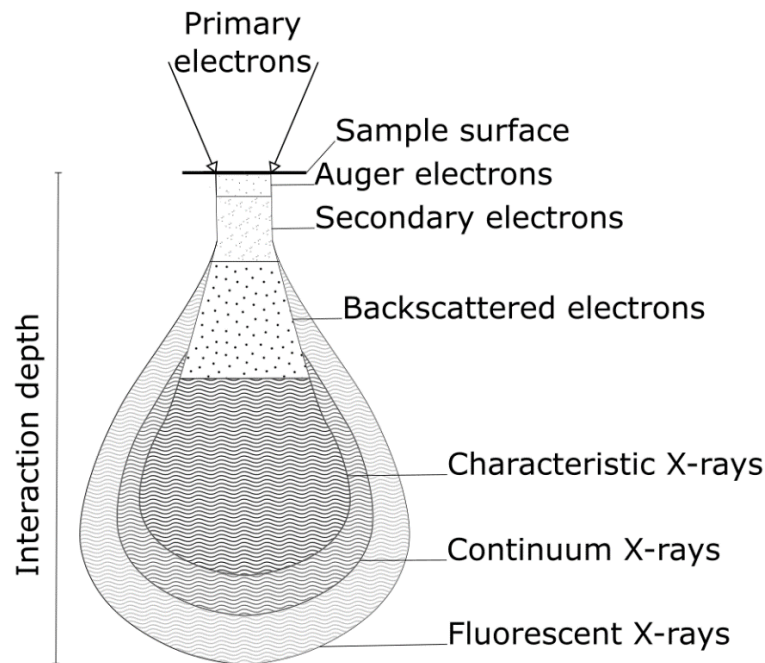


Figure 13: Schematic representation over interaction volume between the primary beam of electrons and the sample surface together with the resulting signals.

To detect the signals, the microscope is equipped with different detectors such as the Everhart-Thornley detector which is a scintillator photo-multiplier. This can detect both secondary- and backscattered electrons and uses high voltage to attract or screen the low energetic secondary electrons. Another is the solid state, semiconductor detector, this consists of four separate detectors placed in each quadrant surrounding the primary electron beam. This is used to detect the backscattered electrons, and since the detectors receive four independent signals it is possible to add and subtract the signals generating very good topology contrasts and 3-dimensional images of the sample surface.

2.6.3.1 Energy Dispersive Spectroscopy

To obtain a localized chemical analysis of a sample, the energy dispersive X-ray spectrometry (EDS) is used. As previously explained, when the primary electron beam interacts with the sample, X-rays will be emitted. The detector used is a solid-state silicon-

lithium energy-dispersive spectrometer. The detector absorbs the energy from the inbound X-rays through ionization. This energy is converted to a voltage of proportionate size which relates the photons wave-length to its characteristic signal. Figure 14 is a schematic representation over a typical interaction between primary electron and atoms in the sample followed by emission of a photon. By separating the emitted characteristic X-rays from the different elements in the sample into an energy spectrum, the EDAX software can be used to resolve the spectrum into the specific corresponding elements. EDS is used to generate fundamental compositional information of the sample by the use of spot size analysis of a few micrometres, line scans and by generating element composition maps over larger areas.

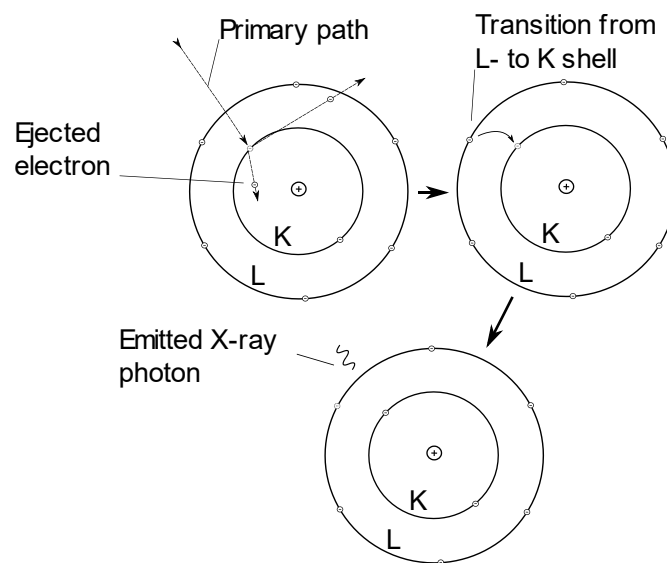


Figure 14: Illustration of ionization of inner shell electron, followed by electron transition from L- to K shell and a subsequent reduction in energy by photon emission.

With EDS it is possible to both quantitatively and qualitatively analyse the chemical composition of the sample. The qualitative analysis involves the straight forward identification of lines in the X-ray spectra. While the quantitative analysis involves measuring the intensity of these lines. For the qualitative analysis it is necessary to use corrections and standard samples of known composition to calibrate the equipment. The corrections used is denominated ZAF. *Z* stands for the correction of differences in scattering due to the atomic number of the elements. Since both the backscattered electrons and the retardation of electrons has a direct correlation to the average atomic number in the analysed area, some areas will emit larger quantities of photons due to the composition. *A* represents correction due to absorption of signal in the sample. As the signal is generated under the sample surface, the photons must travel some distance inside the material before it reaches the surface, thus being prone to absorption. *F* symbolize the correction for fluorescence.

Fluorescence correction is necessary as some elements has a characteristic X-ray with high enough energy to excite other elements, hence generating an excess of signal.

2.6.3.2 Electron Backscatter Diffraction

Electron backscatter diffraction, EBSD, is a highly reliable way to acquire data of the crystallographic orientation and structure. When the primary electron beam interacts with the solid sample, some of the electrons can be diffracted by the atomic layers. By using a phosphorous screen, the diffracted electrons create visible lines, Kikuchi bands, when interacting with the screen. The lines are projections of the orientation and geometry of the different lattice planes in the sample, thus generating a detailed map over the structure and crystallographic orientation of the sampled area. By applying a database consisting of previously known information about phases and their crystallographic parameters such as crystal plane spacing, angles between planes and crystal symmetry elements [64], together with software which process and index the bands with their corresponding Miller indices, the result can be used to identify the different phases in the sampled area. By extrapolating the result, it gives information about the global texture of the sample, while it also can be used to measure grain size and the surrounding boundaries.

The EBSD patterns are obtained when a highly tilted sample, $\sim 70^\circ$ relative to the incident electron beam. Figure 15 is a schematic overview for a typical experimental set up inside a SEM. As shown in the figure, the diffraction from the tilted sample creates a large angled flat cone of signal. The apex semi-angle is given by $90^\circ - \theta_B$, where θ_B is the angle when Bragg reflection occur, given by Bragg's equation (6).

$$n\lambda = 2d\sin\theta_B \quad (6)$$

Where n is an integer order of diffraction, 1, 2, 3, etc. λ is the wavelength of the electron, θ_B is the Bragg angle and d is the spacing of atomic planes.

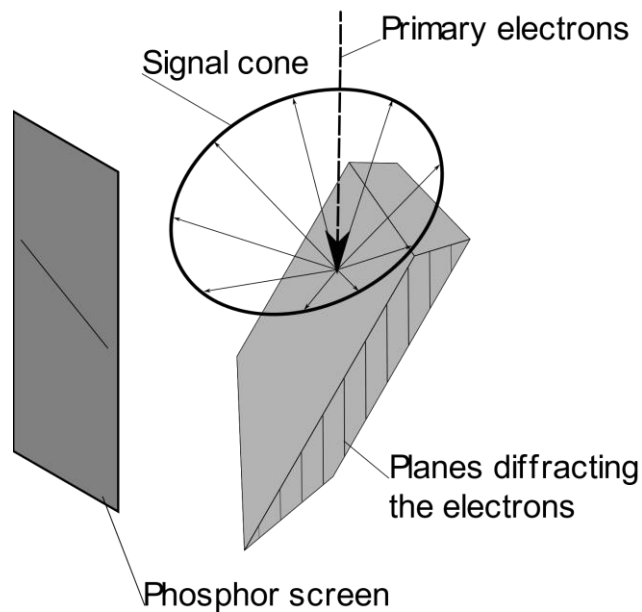


Figure 15: Schematic representation of the experimental set up of tilted sample, incoming electron beam, corresponding diffracted signal from first atomic layer and the phosphor screen.

Since the wavelength, λ , is very small for electrons, the Bragg angle is usually less than 2° . As the electrons are diffracted from the front and back of the atomic crystal, it generates two cones of signal. These signals can be seen as a pair of nearly straight lines separated by an angle of $2\theta_B$, as shown in Figure 16 [62].

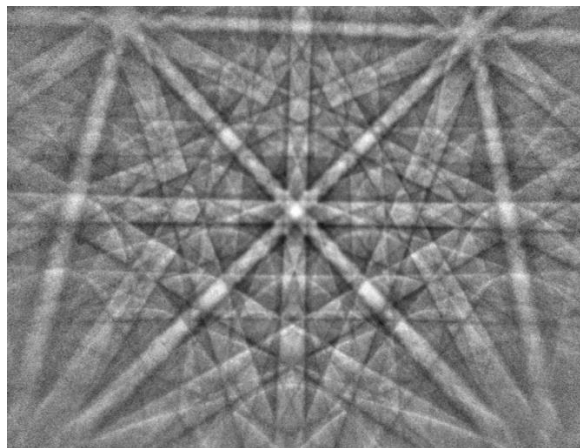


Figure 16: Typical Kikuchi bands from an austenitic steel. The intersecting bands in the centre of the image is generated by the $\langle 001 \rangle$ crystallographic direction [65].

2.6.4 Transmission Electron Microscope

The transmission electron microscope (TEM) is principally built in a similar manner as the optical microscope. Containing an electron canon, such as a lantanhexaborid crystal (LaB_6) together with a positive charged anode plate as a light source, two condenser lenses, an objective lens, two intermediate lenses, a multiple projection lenses and a fluorescent screen to absorb the electrons together with a digital image-producing system. This setup makes it

possible to study very fine details in the sample, yielding a resolving power close to one Ångstrom [66]. This makes the TEM suitable for studying the atomic arrangement near defects, dislocations, and other inhomogeneities such as precipitates along grain boundaries and inclusions. As the microscope uses transmission in the image generation, it is also highly suitable for diffraction analysis.

2.6.4.1 Diffraction

As the electrons “travel through” the sample, elastic- and inelastic collisions will occur. Where the latter result in undesirable diffusive effect in the diffraction images. Since the sample consists of periodically arranged planes of atoms, some of the electrons will travel parallel to- and thus undeviated through the atomic array, while most will be scattered or absorbed. As the electrons get scattered, considering their wave properties, they will interfere with each other constructive and destructive depending on the orientation of the sample relative to the incoming electron beam and the distances between the atomic planes in the sample. The constructive interference occur as the period of two successively scattered electrons are a whole number of wavelengths, as given by Braggs law in equation (6) [67].

The objective lens focuses parallel beams onto a plane, the back focal-plane, thus creating a diffraction pattern as it is projected to the fluorescent screen. Since this diffraction pattern is created by the orientation and periodicity of the atomic planes in the sample, the pattern can be used to determine the crystallographic orientation of the sample, from the general matrix to microscopic particles by the use of a selection aperture to only allow signal from certain areas in the sample [68]. The spots in the diffraction pattern is given Miller indices corresponding to the atomic plane which diffracted the incoming electron. Figure 17a) show an example of a diffraction pattern and its resulting indices for a cubic crystal with incident beam along $00\bar{1}$ direction. For a face-centred cubic crystal, because of its atomic periodicity, it is only possible to achieve a diffraction pattern for atomic positions with either odd- or even Miller indices simultaneously as it is given by the structure factor in equation (7). If the position is a mix of odd and even its intensity becomes zero, resulting in the pattern given in Figure 17b) for an FCC crystal with the incident beam along $00\bar{1}$ direction [67].

$$S(hkl) = \sum_j f_j \times e^{(-2\pi i(u_j h + v_j k + w_j l))} \quad (7)$$

Where u_j, v_j, w_j are the positional coordinates and f_j is the scattering factor for the j th atom while h, k, l are the Miller indices.

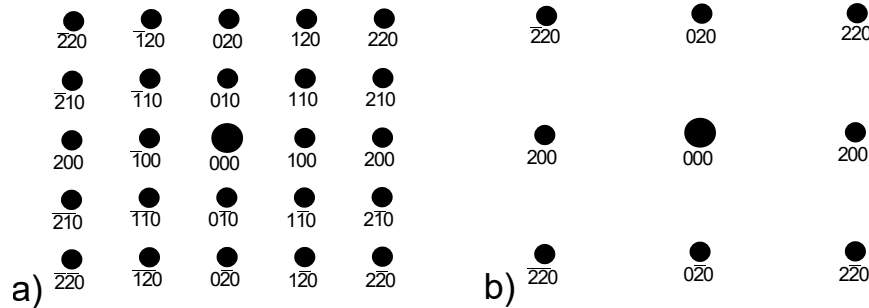


Figure 17: Diffraction pattern and its resulting Miller indices for incident beam along $00\bar{1}$ direction for a) simple cubic crystal, b) face-centred cubic crystal [67].

2.6.4.2 Imaging

While operating the TEM in microscopy-, or imaging mode, instead of diffractive it is possible to get high-resolution images of minute details by exploiting contrast. Contrast in the image occur mainly due to scattering and diffraction of the electrons, differences in sample mass-thickness, bending contour, dislocations and particles. If all the scattered and unscattered electrons were allowed to be focused onto the fluorescent screen an image of very poor contrast would appear. Since a crystalline specimen generate the previously described diffraction pattern, by using an objective aperture, it is possible to extract certain diffraction spots and thus improve the contrast in the image by creating so-called bright- and darkfield images.

The bright field image is created by allowing only the direct electron beam to pass through the aperture and occlude all scattered electrons. Since only a small portion of a samples area satisfies Braggs law at a given time, this technique generates images comprised of a high intensity background containing small areas of low intensity. Comparatively, the dark field image is created by shifting the aperture, so it obstructs the direct electron beam and allow a diffracted beam to pass through and onto the fluorescent screen. Thus, creating a small area of high intensity on a low intensity background. Because the electrons that is allowed to pass through the aperture is off-axis, these images experience a lot more aberrations and can occur with poor quality. By tilting the incoming beam sufficiently, the scattered electrons will be on-axis and the aberrations get eliminated [67].

2.6.5 Hardness measurement

A materials hardness is a characteristic, and not a physical property. The definition of hardness is the materials resistance to localized plastic deformation and is related through equation (8).

$$HV = 1.854 \frac{P}{d^2} \quad (8)$$

Where P is the loading and d is the mean value of both diagonals in the indentation.

The Vickers indentation test has great applicability to thin and small samples. The material is indented by a diamond indenter with a square base and 136° between opposing faces. The force used for indentation is standardised and can be found in ASTM- E-384, this also gives the information about the minimum distance between two successive indentations to be $2.5d$ which is the same for the distance between indentation and any edge [69].

CHAPTER 3

THE MATERIAL

3.1 Direct Laser Deposited material

The studied specimens were created by a TruLaser Cell 3000 AM machine and provided by Nordic Additive Manufacturing (NAM) and TechnipFMC. The machine uses the so-called Direct Laser Deposition technique to add material following a specified raster to pre-existing components. As the machine, when first presented 13th of June 2017, was the first of its kind in Norway, the process is still in its preliminary phase with respect to production parameters and how the resulting products compares to conventional parts. The main task of this investigation will be to analyse microstructural evolution and the binding between base- and deposited material. Assess defects such as brittle zones, pores, interlayered voids, carbide formation and measure how much the material resists localized plastic deformation through hardness testing.

The specimens are two 70 mm long conventionally manufactured and machined rods with an outer diameter of 10 mm in respectively 304- and 316L stainless steel. The rods have 3 wings deposited in 316L-Si stainless steel separated by $\sim 120^\circ$. The wings have dimension 50x10x4 mm in respectively length, height and width. Figure 18 show the specimens as they were before the analysed samples was cut out.

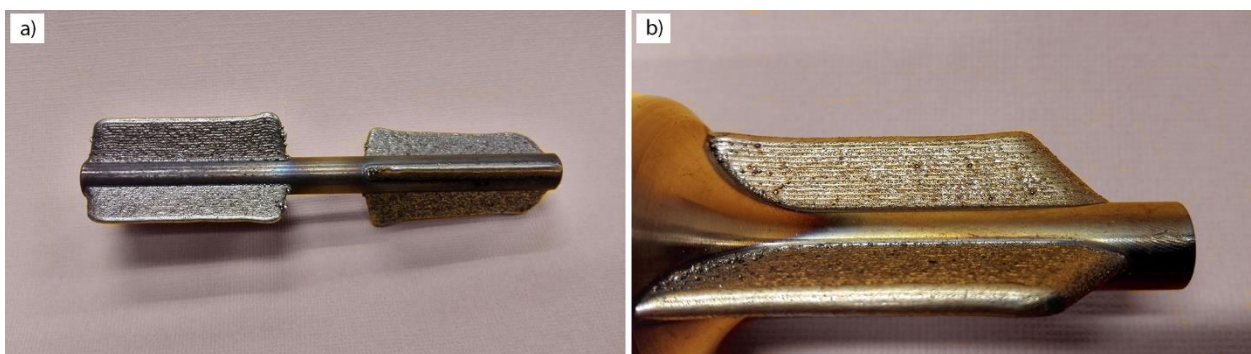


Figure 18: As-received specimens. a) SS316L-Si deposited on SS304, and b) SS316L-Si deposited on SS316L. The specimen 1, with deposited material on SS304 base material was initially not intended to be used for anything other than demonstrative purposes by the producer, thus for this specimen no cleaning procedure was performed prior to deposition and the production parameters used was not optimal. For these reasons, this specimen will be used as a

demonstration of how inadequate parameters and a lack of a pre-cleaned surface influence the components microstructural constitution. The production parameters for specimen 2 is given in Table 4.

Table 4: Production parameters for the SS316L-Si direct laser deposited components.

| Specimen | Laser power [W] | Laser feed rate [mm/s] | Spot diameter [mm] | Powder feed rate [g/s] | Layer thickness [mm] | Line spacing [mm] |
|----------|-----------------|------------------------|--------------------|------------------------|----------------------|-------------------|
| 1 | N/A | N/A | N/A | N/A | N/A | N/A |
| 2 | 840 | 12 | 2.5 | 0.1 | 0.52 | 1.3 |

Both components was produced with a TruDisk 3001 laser which consists of 3kW solid state Nd:YAG (Neodymium-doped Ytterium Aluminium Garnet) laser diodes. Carrier gas for the powder material was helium while argon was used to create an inert environment during production.

3.2 Powder material – MetcoClad SS316L-Si

The powder material used to create the specimens was MetcoClad SS316L-Si which is a gas-atomized, nickel-chromium stainless steel powder which is generally used as a laser cladding material. The material has the same chemical composition as regular 316L stainless steel, only with a higher content of silicon which acts as a fluxing agent and improves wetting, this facilitate a cleaner clad deposit. Table 5 gives the chemical composition of the powder material. The material has a spheroidal morphology which can be seen in Figure 19 [70].

Table 5: Chemical composition of MetcoClad SS316L-Si powder given in wt%.

| C | Mn | Si | Cr | Ni | Mo | Other | Fe |
|------|-----|-----|------|------|-----|-------|---------|
| 0.03 | 1.0 | 2.3 | 17.0 | 12.0 | 2.5 | ≤ 0.5 | Balance |

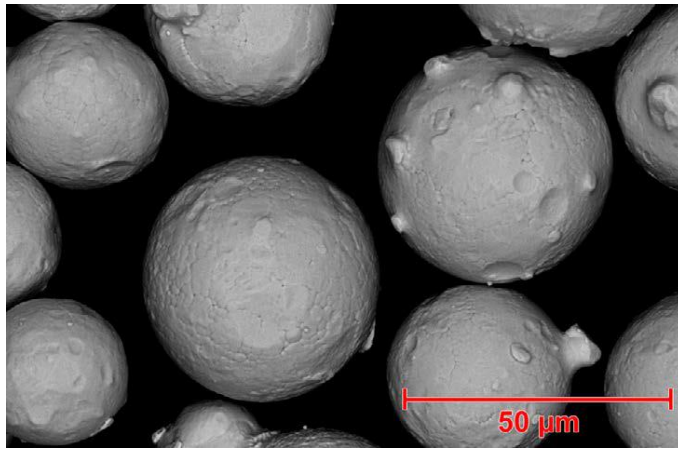


Figure 19: SEM micrograph showing the morphology of MetcoClad SS316L-Si powder material.

Apparent density of the material and the particle size distribution is given in Table 6.

Table 6: Nominal size range and apparent density of MetcoClad SS316L-Si powder material.

| MetcoClad SS316L-Si | Nominal size range | Apparent density |
|---------------------|--------------------|---------------------------|
| | 106-44 μm | 4.0-4.5 g/cm ³ |

CHAPTER 4

EXPERIMENTAL PROCEDURES

4.1 Sample extraction

In order to analyse the DLD manufactured material, it was essential to perform metallographic preparations.

The first task was to examine the material as delivered from TechnipFMC and evaluate the most efficient way to take out samples which would give the necessary insight in the solidification process, the material structure, the heat-affected zone and also hardness values. Table 7 lists the 4 different evaluated samples and their orientation with respect to the travel direction of the laser beam.

Table 7: Investigated material, orientation relative to laser travel direction (LTD) and corresponding sample number.

| Material | Sample number | Orientation w.r.t. LTD |
|---------------------|---------------|------------------------|
| SS316L-Si on SS304 | 1 | Cross section |
| | 2 | Plane |
| SS316L-Si on SS316L | 3 | Cross section |
| | 4 | Plane |

Figure 20 show an illustration over orientation and placement of the samples in the rod. The samples where cut using a Struers Discotom-5, the machine uses large amounts of coolant to avoid any unnecessary heating of the material. To avoid mechanical deformation the machine was setup to a feed-rate of 0.15mm/s.

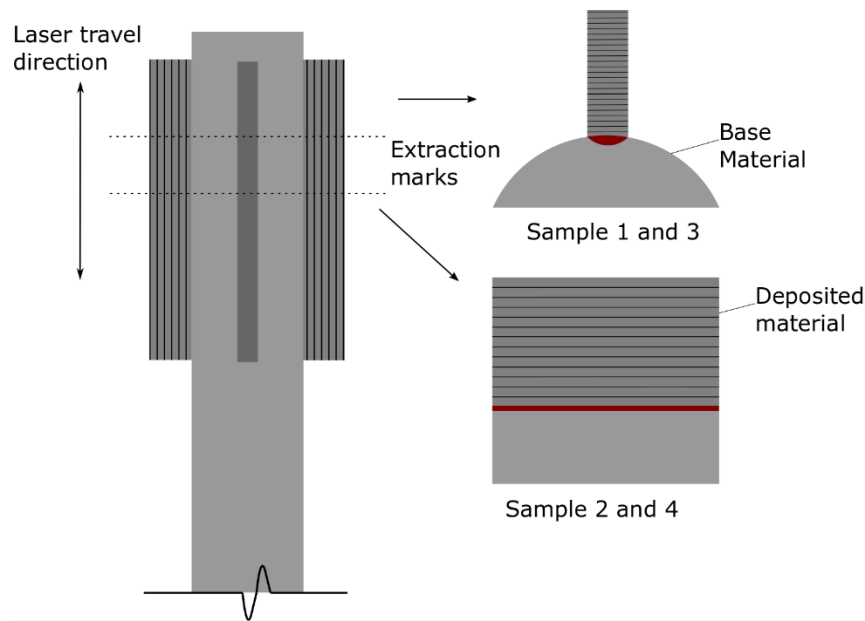


Figure 20: Schematic representation over machined rod, deposited wings and the orientation of the different samples with respect to the laser travel direction. Samples 1 and 3 are cross-sectional cuts, samples 2 and 4 are planes along the travel direction.

Specimen 2 and 4 needed further fine-cutting to remove excess material from the rod. This was performed on a Struers Acutom-2 with feed-rate of 0.01mm/s and sufficient amounts of coolant.

4.2 Constituent analysis

Since the DLD-material is produced by powder material, there are some considerations needed to be done prior to the metallurgical investigation. As the SS316L-Si is a relatively soft material, during grinding the abraded material will get pushed into pores and thus even out the existing crevices. To counteract this an extended polishing time is needed to get a correct and representative image of the surface porosity of the samples [71].

4.2.1 Light Optical Microscope

Prior to the light optical microscopic analysis, the specimens required further preparation. After the cutting procedure the samples were thoroughly cleaned and rinsed with both water and ethanol to remove contaminants and grease. The specimens were then casted using a Struers Citopress-30 in clear acryl, SpeciFast, which generated a flat surfaced cylinder that provided easy handling and mounting for grinding and polishing. Figure 21 show the samples post-grinding and polishing.

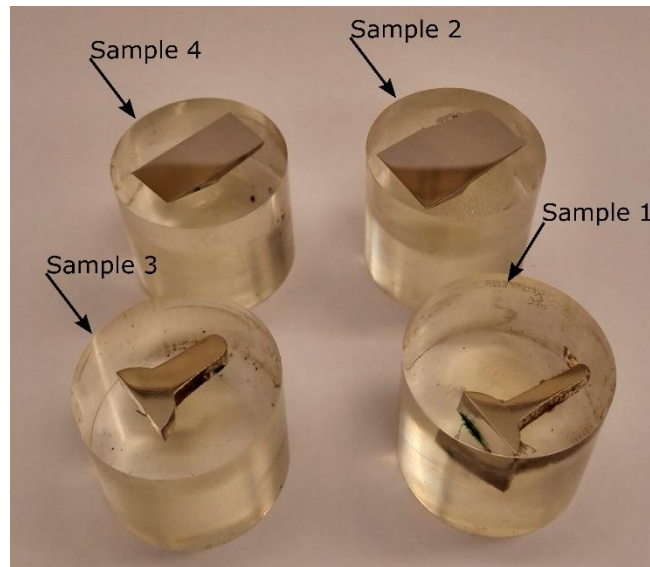


Figure 21: Samples 1-4 mounted in clear acrylic resin, Specifast, after grinding and polishing.

The grinding and polishing was executed on a Struers Pedemax-2. The procedure used for grinding and polishing followed the guidelines of the standard ASTM E03-11(2017) – Standard Guide for Preparation of Metallographic Specimens [72]. An 11-step procedure. After each step the specimens was thoroughly cleaned using hot water to rinse them from contaminating particles, followed by cleaning with ethanol to remove the water and hot-air blowing to get dry surfaces. The full procedure is presented in Table 8.

To reveal details in the material surface, an etching procedure proposed by Struers was followed. They proposed etching the specimens in 10% aqueous oxalic acid with 15V applied for 60 seconds [73]. This was also the procedure used in a previous master thesis which analysed selective laser melted SS316L and yielded very good microscopically results [74]. The procedure turned out to generate a quite corroded and dark tinted sample surface, after some trial and error the time was reduced to 24 seconds while keeping the voltage at 15V.

The micrographs were taken on an Olympus GX53 using an integrated software Olympus Stream to exploit various resolution, contrast and imaging options to reveal as much details about the general macro- and microstructure, fusion lines, the heat-affected zone and pores as possible.

Table 8: Procedure for grinding and polishing performed on a Struers Pedemax-2 with settings 1 kg and 150 rpm.

| Step | Grinding and polishing | Lubricant | Time [min] |
|------|---------------------------------------|------------------------------|-------------|
| 1 | 120P | Water | Until plane |
| 2 | 180P | " | 1 |
| 3 | 220P | " | 3 |
| 4 | 320P | " | 3 |
| 5 | 500P | " | 5 |
| 6 | 1000P | " | 5 |
| 7 | 2000P | " | 7 |
| 8 | 9 μm diamonds | Struers DP Lubricant-Blue | 10 |
| 9 | 3 μm diamonds | " | 12 |
| 10 | 1 μm diamonds | " | 10 |
| 11 | 0.04 μm OP-S Suspension | - | 4 |

4.2.2 Scanning Electron Microscope

The imaging-, orientation diffraction pattern- and spectroscopy were executed using a Gemini SUPRA 35VP equipped with an energy dispersive X-ray spectroscope from EDAX. The grinding and polishing procedure followed was similar to that used prior to LOM analysis, except it was not necessary to etch the surface as polishing with colloidal silica revealed all the necessary details. An ultrasound bath was performed to remove any contaminants to reach the vacuum chamber. The bath was performed in a Struers Lavamin, an automated ultrasound bather before each session in the SEM.

Since it is necessary to conduct the electrons that reach the sample surface, and the samples were mounted in acrylic resin a conductive carbon tape was used to complete the circuit. To reduce the influence of unwanted effects such as astigmatism and the resulting wobble of the electron beam, chromatic- and spherical aberrations and diffraction, the settings needed to be carefully adjusted depending on which type of detail that was to be evaluated with respect to acceleration voltage, working distance, aperture and detector.

For the EDS, the sample did not need any further preparation and could be analysed as it was during the microscopic analysis.

4.2.3 Electron Backscattered Diffraction

The EBSD data was collected using an orientation imaging microscope (OIM) system from TSL equipped on the SEM. Since the image quality is highly surface-sensitive, samples had the same surface preparation prior to the EBSD analysis as for the SEM only with an extended period of 2 minutes during polishing with OP-S to void the sample surface of any micro-scratches.

Preceding the EBSD imaging the casted samples needed an overall size reduction to enable the fitting onto the EBSD specimen holder. The height reduction was done by mounting the samples in a sample holder and grinding the acrylic cast from the opposite side of the specimen on a coarse grinding paper, P80, until the height was satisfactory at about 3 mm. This gave minimal risk of surface scratching and allowed for a continuous control of keeping the grinded surface planar. After grinding the samples were thoroughly washed and cleaned in alcohol, followed by an ultrasound bath in the automated Struers Lavamin.

4.2.4 Transmission Electron Microscope

To analyse dislocations, nanoparticles and carbides thorough investigation was performed on a Jeol 2100 transmission electron microscope with a LaB₆ filament operating with an acceleration voltage of 200kV. The microscope was equipped with high angle annular bright- and dark field detectors and an X-ray spectroscopic system from EDAX. Prior to the examination sample 2 and 4 was picked as suitable specimens for investigation, as these types of samples had a large enough surface area to collect the TEM specimen discs. The samples were cut on the Struers Acutom-2 to a <1mm thickness, mounted to a plexiglass block with adhesive tape and grinded manually with successively finer grit paper, from 120p to 1000p on both sides of the samples. This process was completed when the samples had become thin foils with thickness between 100-50 µm. After the foils was removed from the adhesive tape by the use of liquid nitrogen, they were cleaned with acetone to remove any remaining adhesive. A Gatan stamping tool was used to punch out discs with a diameter of 3 mm for further specimen preparation. In accordance with previous studies, an electrolyte was mixed containing 5% perchloric acid and 95% methanol and cooled to a temperature of -40 °C. The discs were then in turn fixed between two cathodes and placed inside a chamber for electropolishing using a Struers TenuPol-5 dual-jet polishing system. Two electrodes were

attached to the cathode plates and a voltage of 15 V was applied. This made the disc susceptible for polishing as it became an anode. The electrolyte was continuously jetted onto the disc surface until a small hole was formed which allowed enough light to reach a sensor which cut the jet system. Further the discs were washed and rinsed in three consecutive baths of ethanol to remove any remaining electrolyte and debris.

4.2.5 Hardness evaluation

The hardness testing was conducted on a Struers DuraScan using 10 kg HV force with a dwell time of 10 seconds for the indentation. To get an understanding of and investigate how the material resist plastic deformation, the hardness measurements was conducted both normal and parallel to the build direction for all samples. The parallel measurements were conducted from the deposited material, 1 mm from any edge with a 1 mm increment down toward the existing material and 3 mm into base material. The normal measurements were also conducted 1 mm from any edge with a 1 mm increment. Two sets of data were collected from all samples for the parallel measurements to get a more statistical accurate result that also would reveal if there was any large variation in the hardness from different areas in the sample, while three sets of data were collected from all samples for the normal measurements. Figure 22 is a schematic representation over the position for the extracted data for both a plane- and a cross sectional cut sample.

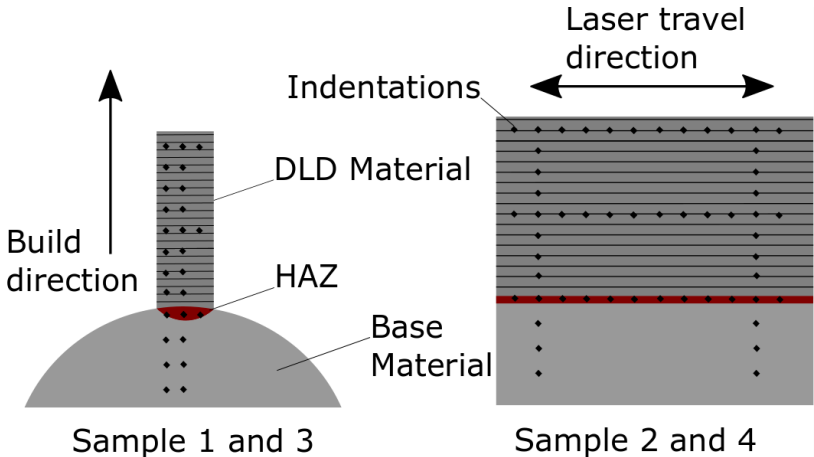


Figure 22: Schematic illustration over locations for the indentations for cross sectional and plane samples with indication of build- and laser travel direction.

The average hardness value was obtained by averaging a minimum of 8 indentations across the deposited material. Due to the width of sample 1’s cross section, it was conducted one column of indentations located at the centre of the cross section for the measurements parallel to deposition direction. And for the normal direction measurements was conducted

by two rows with two indentations in each. For sample 3, the normal to deposition direction measurements was conducted in three rows with three indentations in each.

Pre-hardness testing, the samples was grinded and polished following the same procedure as for the microscopic preparation. The Struers DuraScan is controlled by a computer and after each indentation the hardness values was calculated automatically. If the localized plastic deformation was to severe the machine opened for the possibility of manual measurement, this allowed for precise data collection.

4.2.6 Cross-sectional density calculation

To assess the amounts of pores present in the material, samples 1 and 3 was chosen for density measurements as these represents the total cross section of the parts. The investigation was done prior to the hardness measurements, thus the same sample preparation was followed.

Micrographs was taken for at least 50% of the sample cross section from the top all the way to the base material. Further the images were processed with a software tool called ImageJ. The image was loaded in the program and the software calibrated. After converting the micrograph into a grayscale image, the dense material was represented in white while the pores and defects in black as shown in Figure 23. The software then calculated the number of dark pixels, converting the results to corresponding surface area and supplied the outcome in a table. Full procedure is given in the appendix. After this, some additional calculations with respect to the results, analysed area and the overall sample area gave a representation over the total cross-sectional density of the samples.

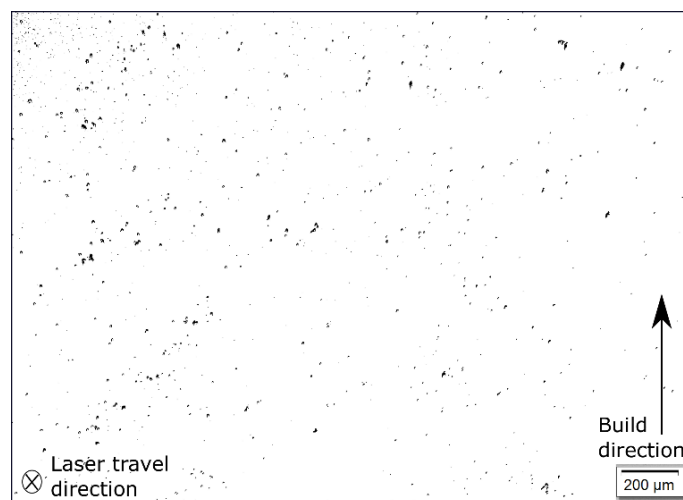


Figure 23: Grayscale image representation of pore content in the cross section of the sample 3. The white represents the solid material while the black is the pores.

CHAPTER 5

EXPERIMENTAL RESULTS AND DISCUSSION

5.1 Microstructure

5.1.1 General macro- and microstructure

The macroscopic overview of the samples 1, 3 and 4 are shown in Figure 24. Measurements show that each consecutive deposited layer penetrates the previous layer between 150-250 μm . The Figure 24a) and b) show a clear difference in penetration depth into the base material, indicating that the specimen 1 has received a lower energy input during the process.

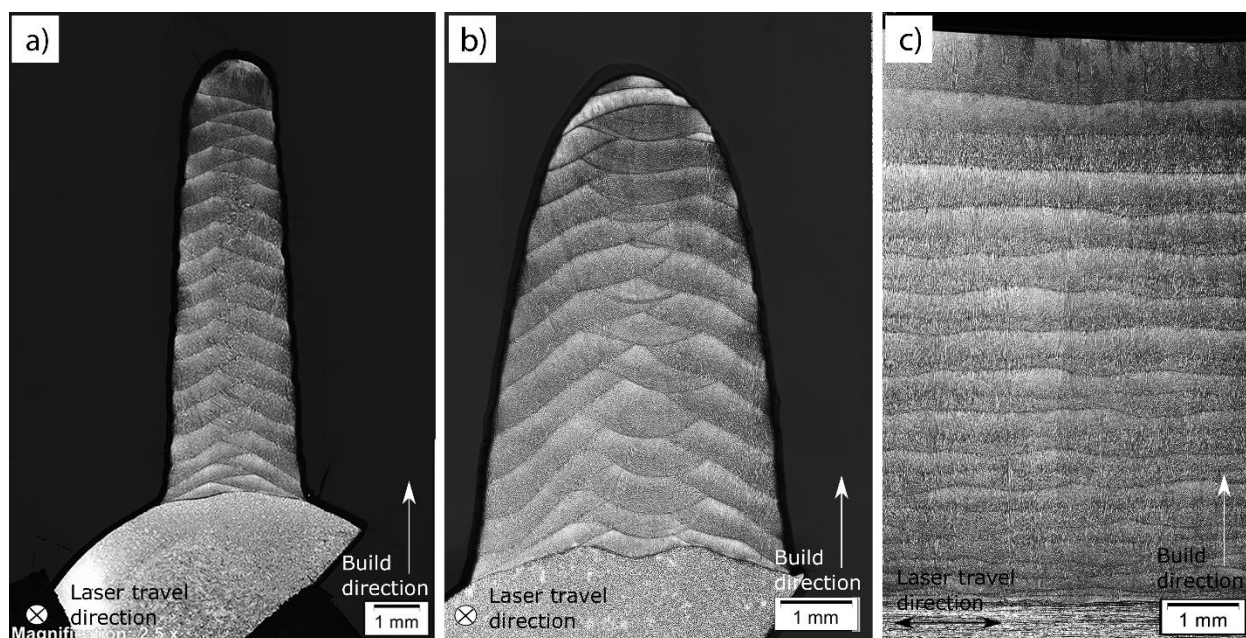


Figure 24: Macroscopic overview presenting the etched sample surfaces revealing fusion lines for a) sample 1, b) sample 3 and c) sample 4.

Figure 25 show the local variations in microstructure observed in all samples for the mechanical polished and chemically etched surfaces. The microstructure observed is contributed to the high temperature gradient and cooling rates resulting in rapid solidification and a refinement of the microstructure. The microstructure was found to be almost identical between the cross-sectional samples 1 and 3 and the plane samples 2 and 4. Figure 25a) show how each layer has its own local heat-affected zone of approximately 100 μm , containing a coarser microstructure. As a layer is deposited, the previous layer still maintains a higher temperature which voids the melt pool from rapidly dissipating heat into the

previously deposited- and surrounding material. This has favoured the forming of a 50 μm band containing cellular- and some planar dendrites between each layer as shown in Figure 25b), this continues into a regular directionally grown dendritic structure influenced by the thermal gradient.

The cooling rate experienced by the material was calculated by evaluating the secondary dendrite arm spacing (SDAS). The investigation show that the two different specimens has experienced slightly different cooling rates. By measuring the length of ten dendrites dispersed evenly throughout the samples, over as many dendritic arms as possible as shown in Figure 25c), the average SDAS was calculated.

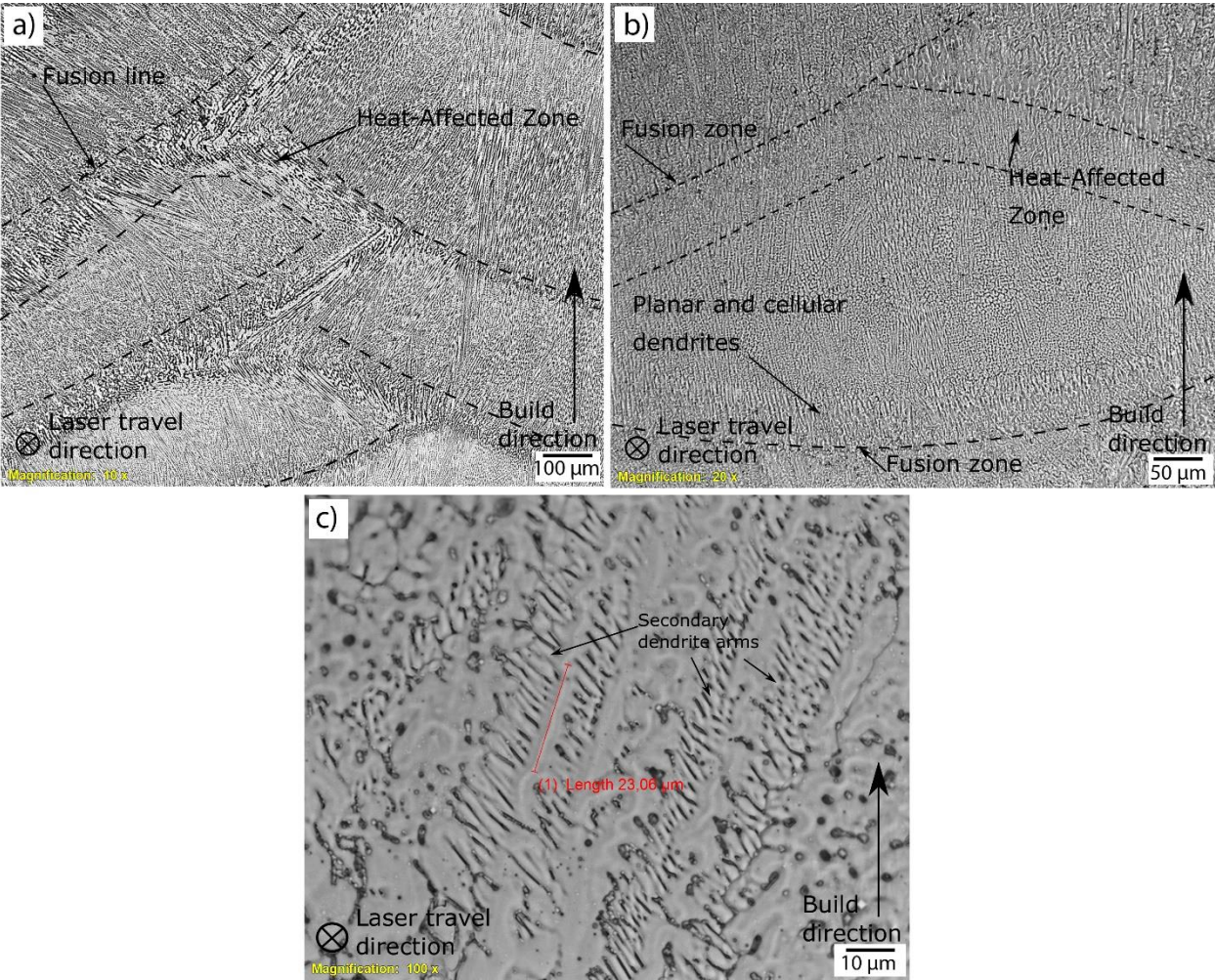


Figure 25: Micrographs of polished and etched surfaces. a) Sample 3 revealing fusion lines and local heat-affected zones between each layer. b) Higher magnification over a deposited layer showing the complex microstructure observed. Initial cellular and planar dendritic growth which continues into directional dendritic with a coarser structure in a local heat-affected zone due to the following layer on top. c) Optical micrograph over sample 1 showing a clear image of the dendritic structure in the DLD SS316L used for calculating cooling rates.

Averaging the results gave the SDAS; $\lambda_2 \sim 2.51 \mu\text{m}$ for samples 1-2 and $\lambda_2 \sim 2.39 \mu\text{m}$ for samples 3-4. Applying the relation between λ_2 and cooling rate \dot{T} as given by equation (9) which has been experimentally determined [75], and used on multiple austenitic stainless steels under similar conditions [76-78].

$$\lambda_2 = 25\dot{T}^{-0.28} \quad (9)$$

The average cooling rate was found to be 3700 K/s for samples 1-2 and 4400 K/s for samples 3-4, these values are consistent with the literature [24]. Measurements of the SDAS show that the cooling rate is varying throughout each deposited layer. Areas in close proximity to the surrounding material, just above the local heat-affected zone between two layers experience the highest cooling rate with a gradual reduction towards the middle of the melt pool and upward. This show that there is a varying temperature gradient in the solute which affect the microstructure in multiple ways;

The temperature gradient formed between the melt pool and the pre-deposited material is ordinarily largest perpendicular to the previous deposited layer, resulting in thermally guided growth of the dendrites. The ratio G/V_s between temperature gradient G and solidification velocity V_s , can be used to depict the microstructural morphology. Since at the bottom of a deposited layer the temperature gradient is high, the solidification velocity tends toward zero giving a high G/V_s ratio. This is beneficial for the cellular dendritic growth seen [79]. As the solid-liquid interface and heat accumulation migrate, the temperature gradient decrease accordingly in the deposited layer. As the heat flow is no longer primarily through the previous layer, but outward to the surroundings the solidification velocity increase as the temperature gradient decrease, then the solidification will favour columnar dendritic growth perpendicular to the previous layer with perturbations along its side which develop into the secondary dendritic arms. When G/V_s exceeds a critical value of 0.5 for SS316L the conditions accommodate equiaxed grain formation [80, 81]. Figure 26a) reveals how the dendrites has fused their secondary arms together forming columnar grains and that the next deposited material, upon cooling, arrange itself and grow epitaxially from the previous layer's dendrites. As seen in Figure 26b) which is a micrograph in the plane of laser travel direction, the epitaxially grown dendrites form columnar grains stretching over several layers. This is usual behaviour for welded stainless steel, and the large grains will influence the yield- and tensile strength of the material greatly. By adding inoculants to the powder material this would

facilitate heterogenous nucleation of equiaxed grains in front of the growing dendritic interface, and thus refine the columnar grain structure [59].

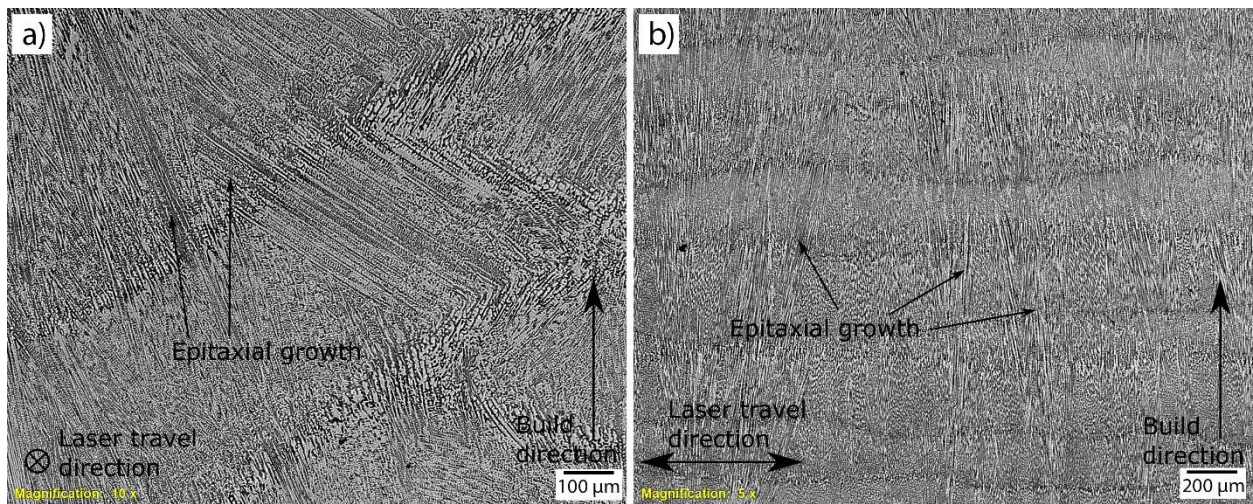


Figure 26: LOM-graphs showing directional growth of the dendrites. a) Epitaxial growth over a fusion zone in sample 3, secondary dendritic arms have fused together forming columnar grains. b) Lower magnification LOM-graph showing the epitaxial growth continuing over multiple layers, image from sample 4.

The comparison of the microstructure observed in different layer in the deposited SS316L-Si for sample 3 is given in Figure 27. The first layer, N1, is presented in Figure 27g) and h) showing respectively the centre and edge deposited line. The images show that N1 has solidified in a similar manner both at the centre and the edges. Due to the room temperature base material it has produced a high solidification rate and a heat flux pertaining mainly perpendicular to the base material surface. This has resulted in elongated and columnar dendrites. The centre and edge of N7 is shown in Figure 27e) and f). This layer shows signs of being deposited when bulk temperature of the part had risen significantly compared to the N1, resulting in a slower solidification rate. As the centre layer is the last of the three neighbouring lines to be deposited, it has been surrounded by excessive heat which has resulted in a coarser and clustered cellular dendritic structure without secondary arms on the dendrites and less columnar dendrites. Towards the edge (right side) in Figure 27f) a more clearly columnar dendritic structure with side perturbations can be seen. Indicating the occurrence of a high solidification rate due to more of the deposited material surface being towards the surrounding atmosphere. Higher magnification micrographs of the contrasting microstructure are given in Appendix B. N11 is presented in Figure 27c) and d), the figure shows a quite similar microstructure to N7 with a more predominant columnar structure towards the edge than at the centre of the component. The last layers, N13, N14 and N15 is presented in Figure 27b). N14 is comprised of a homogeneous variety of both clusters of

cellular- and columnar dendrites. While the last layer N15 consists almost entirely of columnar dendrites which has solidified perpendicular to the previous surface layer in the direction of thermal gradient giving a fan-like orientation of the grains.

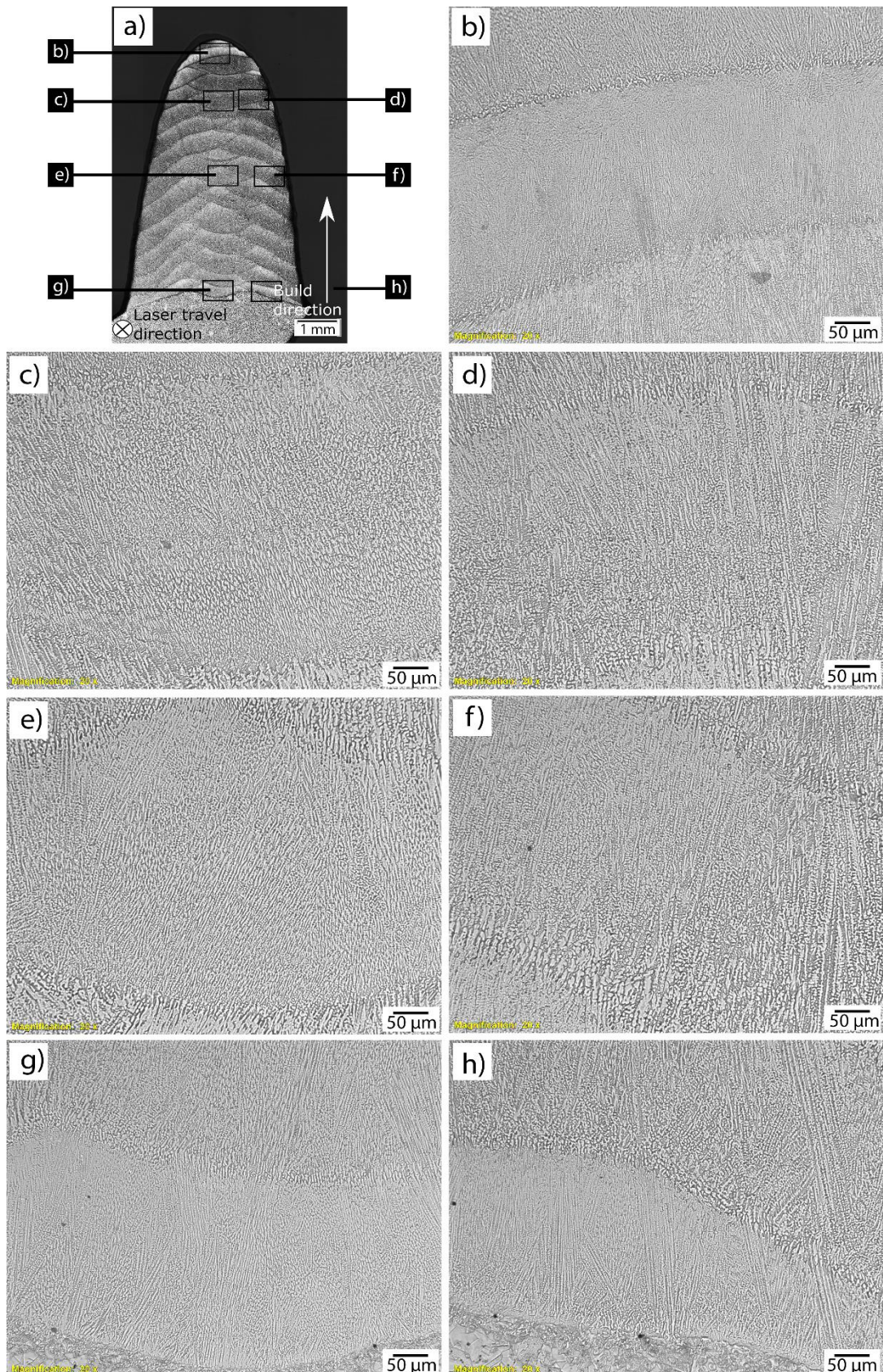


Figure 27: LOM-graphs showing the similarities and differences observed through the deposited layers. a) Sample 3 with indications for where the different micrographs are extracted. b) N13, N14 and N15 at the centre. N10 at c) centre and d) edge. N7 at e) centre and f) edge. N1 at g) centre and h) edge.

5.1.2 Fusion to base material

Due to comparatively (to welding) low heat input and rapid cooling the base material adjacent to the deposition is not kept at an elevated temperature for an extended period. This results in a band of approximately 100 μm of coarser grains in the base material as can be seen in Figure 28a) which is a micrograph from the SEM. The coarser austenitic band is followed by another layer with slightly finer grains which gradually blend into the unaffected base material. As expected a chill zone is formed to the base material, Figure 28b) which is a LOM-graph showing the good metallurgical fusion between the two materials and the slight increase in grain size in the heat-affected zone. A 50 μm band of cellular and planar dendrites has formed adjacent to the fusion zone in the deposited material as indicated in the figure. When the deposited material comes in contact with the base material, the super cooling is initially low. Similar to the layers in the deposited material, the heat accumulation favour cellular growth, while the columnar dendrites that manage to form grow in a planar manner following the heat dissipation growing parallel to the base material surface. Supplementary images are given in Appendix C.

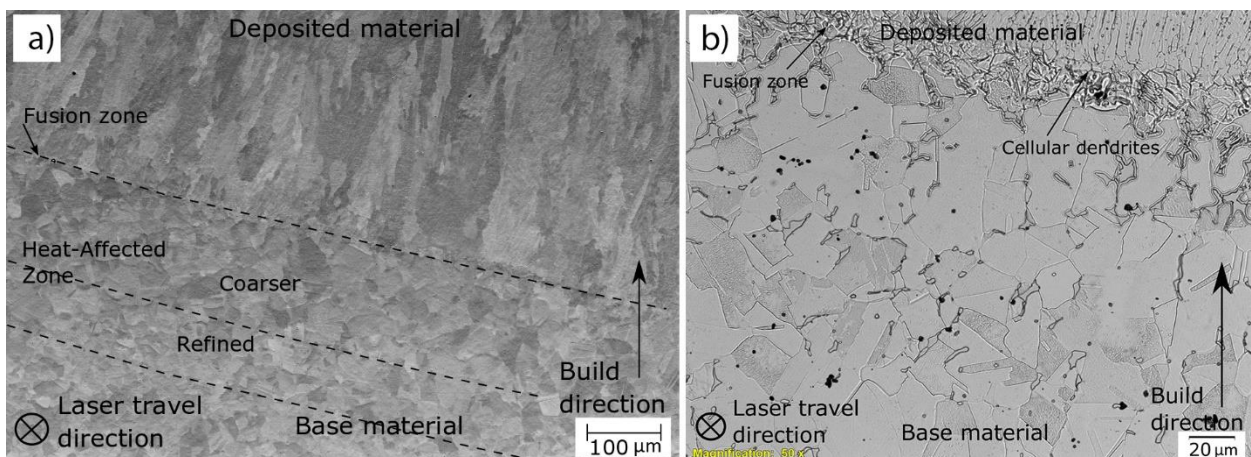


Figure 28: Micrographs over the heat-affected zone to base material for sample 3. a) SEM-graph taken with secondary electron detector showing the 100 μm band of coarser austenitic grains followed by a smaller layer of a slightly refined grain structure. b) LOM-graph showing higher magnification of the coarser grains together with the fusion zone and a layer of cellular and planar dendrites.

5.1.3 Quantitative analysis of microstructure

To get a quantitative understanding of the microstructure for the DLD material, EBSD was used to extract information about crystallographic texture, grain size and grain boundary misorientation. Figure 29a) show the inverse pole mapping for a region above the HAZ for sample 3. The grain orientation with respect to their $\langle hkl \rangle$ indices is indicated with the various colours, following the inverse pole figure located in the top right corner. The figure clearly shows the large columnar grains observed in LOM and SEM.

The length of the grain in elongated direction is 5-10 times larger than in the transverse direction. Being up to 430 μm long and 50 μm wide. Figure 29b) which is the image quality mapping revealing the grain boundary affiliated to Figure 29a), show how these large columnar grains contain smaller grains with length in the vicinity of 125 μm with an average width of 26 μm . The fraction of misorientation angles observed in the materials are represented in Figure 29d). The vast majority of the grain boundaries display a low misorientation angle in the region 1° - 4° , this low misorientation is attributed to the smaller grains visualized as minute colour variations within the grains in the inverse pole map. This is previously observed in a study done by Yadollahi et. al [13]. The pole figure shown in Figure 29c) reveal that the material has a preferential orientation generating solidification texture with the $\langle 001 \rangle$ direction along the build direction. This is previously observed in multiple studies [82, 83]. The pole figure does not show evidence of a fibre texture as one would expect with the columnar grains, and the vertical displacement of the pole clusters is assumed to be attributed to the grains growing with a slight angle in the laser travel direction (towards the reader). The texture observed indicate that the material exhibits some anisotropic mechanical properties, as the material reach its plastic deformation region during loading, less barriers would be needed to cross for the migrating dislocations [34, 47, 84]. This would reflect on the mechanical properties in the build direction, generating a lower strength if loading is applied here.

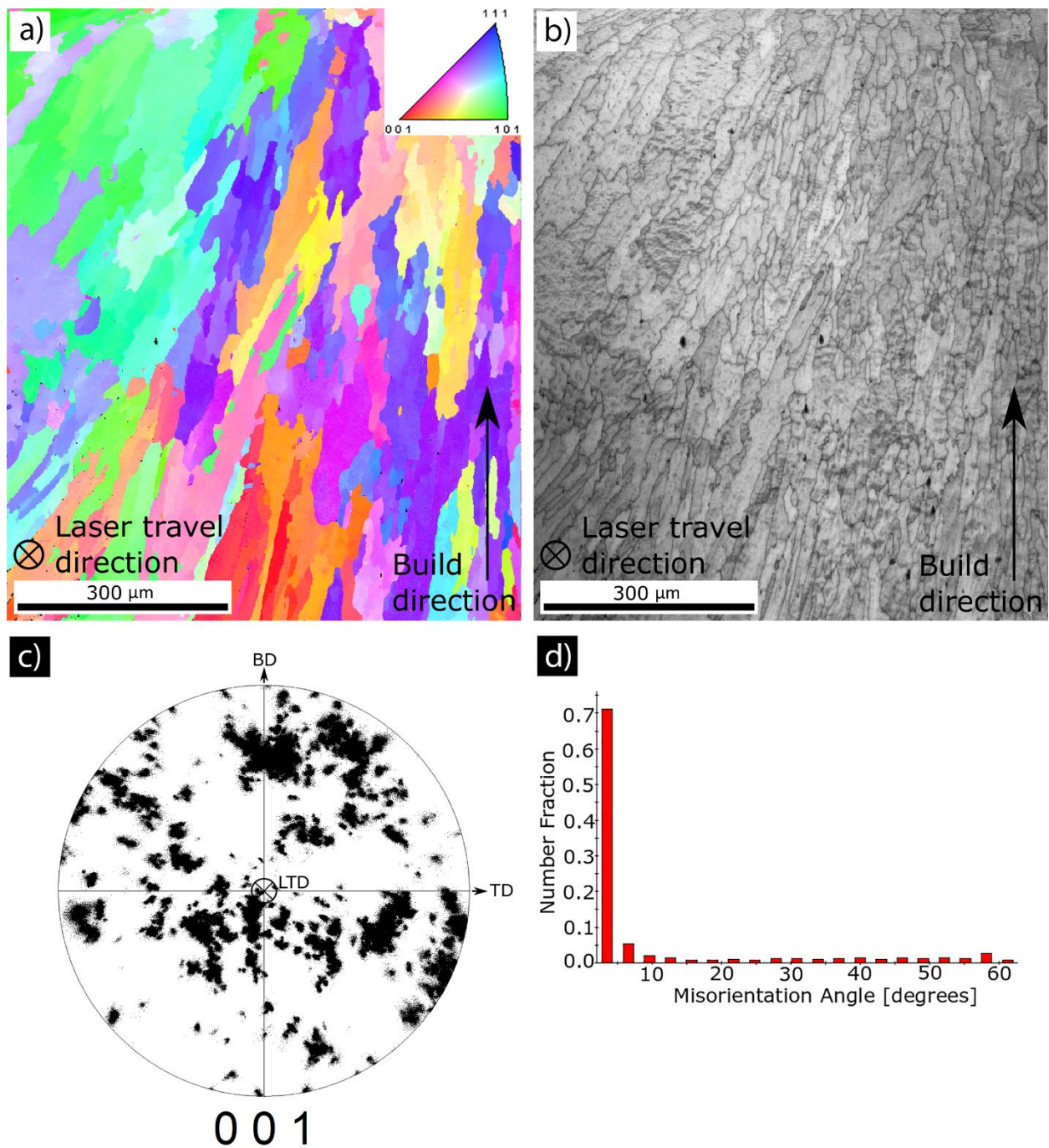


Figure 29: Quantitative data from EBSD mapping over sample 3 showing sub grains, texture and grain boundary misorientation. a) Inverse pole map, b) image quality map showing features such as grain boundaries, c) pole figure where BD, TD and LTD refers to respectively; Build direction, transverse direction and laser travel direction. d) The grain boundary misorientation.

Figure 30 show the EBSD mapping for sample 2 containing the fusion boundary between the base- and the first layer of deposited material, N1. Figure 30a) is the inverse pole mapping, it clearly reveals that some of the grains in the deposited material has formed epitaxially with the grains in the base material. The fusion zone to N2 also reveal some of the equiaxial grains in the local heat-affected zone between the layers as can be seen more evident in Figure 30b) which is the image quality map associated with Figure 30a).

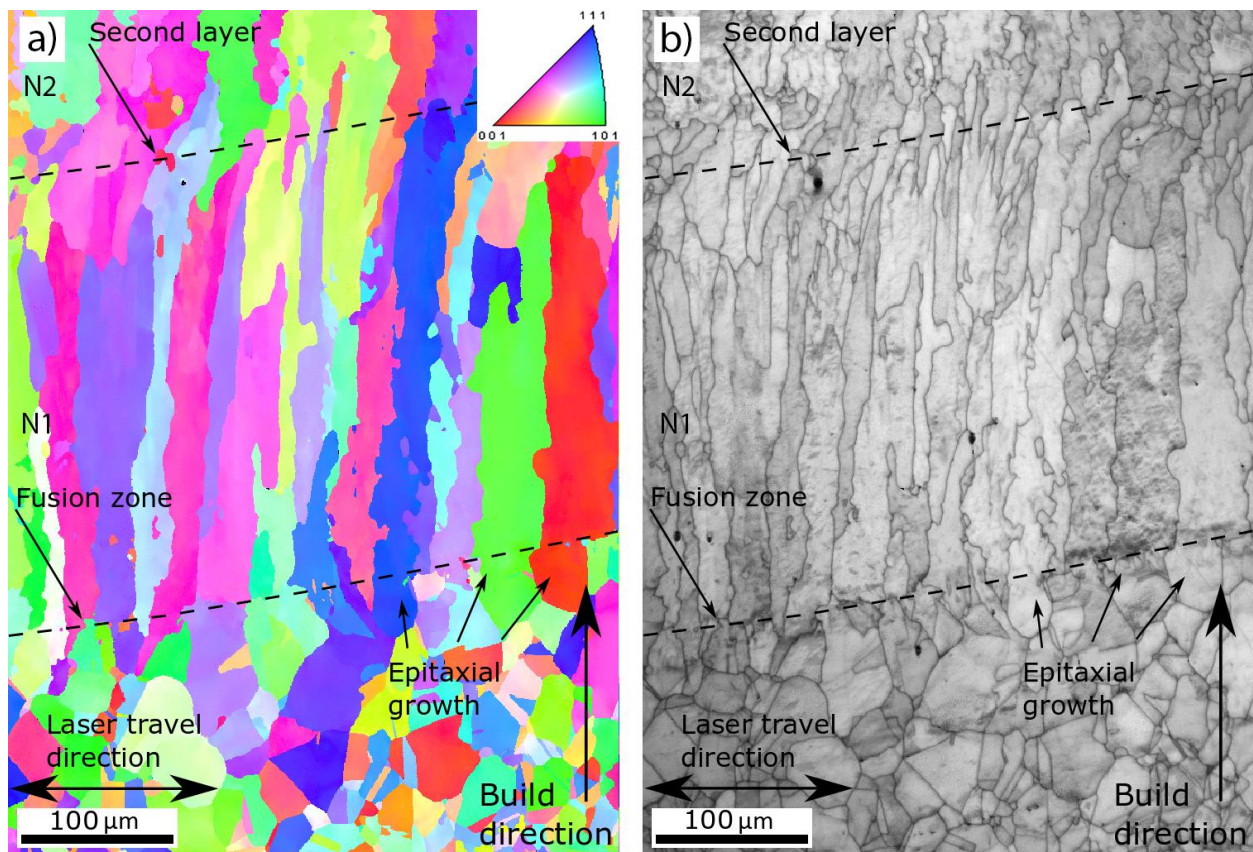


Figure 30: EBSD mapping over the HAZ for sample 2. Dashed lines separating base material, 1. and 2. layers. a) Inverse pole map and b) Image quality map showing the grain boundaries.

5.1.4 Secondary phase δ -ferrite

TEM was utilized to confirm the presence of the secondary phase δ -ferrite and examine its morphology. A 1 μm roundish, globular speck of δ -ferrite hanging out into a hole in the TEM sample was selected for investigation as shown in Figure 31. By orientating and tilting the sample the reciprocal room was rebuilt by the use of selected area diffraction (SAD) patterns. Figure 31b) show the first revealed projection $[111]$, by retaining the $\bar{1}01$ reflection and tilting the sample additionally gave the second SAD pattern $[131]$ as seen in Figure 31c). In the end a third clear diffraction pattern appeared, the $[010]$ projection presented in Figure 31d). Calculations showed that the first and last projections was separated by $\sim 54^\circ$ which gave the initial indication of the projections being $[111]$ and $[100]$. The next indication that the analysed speck had a BCC lattice structure came while examining the SAD patterns, calculating the lattice parameter which turned out to be $a = 2.951\text{\AA}$ and comparing this to the lattice parameter given in the literature, $a = 2.866\text{\AA}$ for ferrite [85].

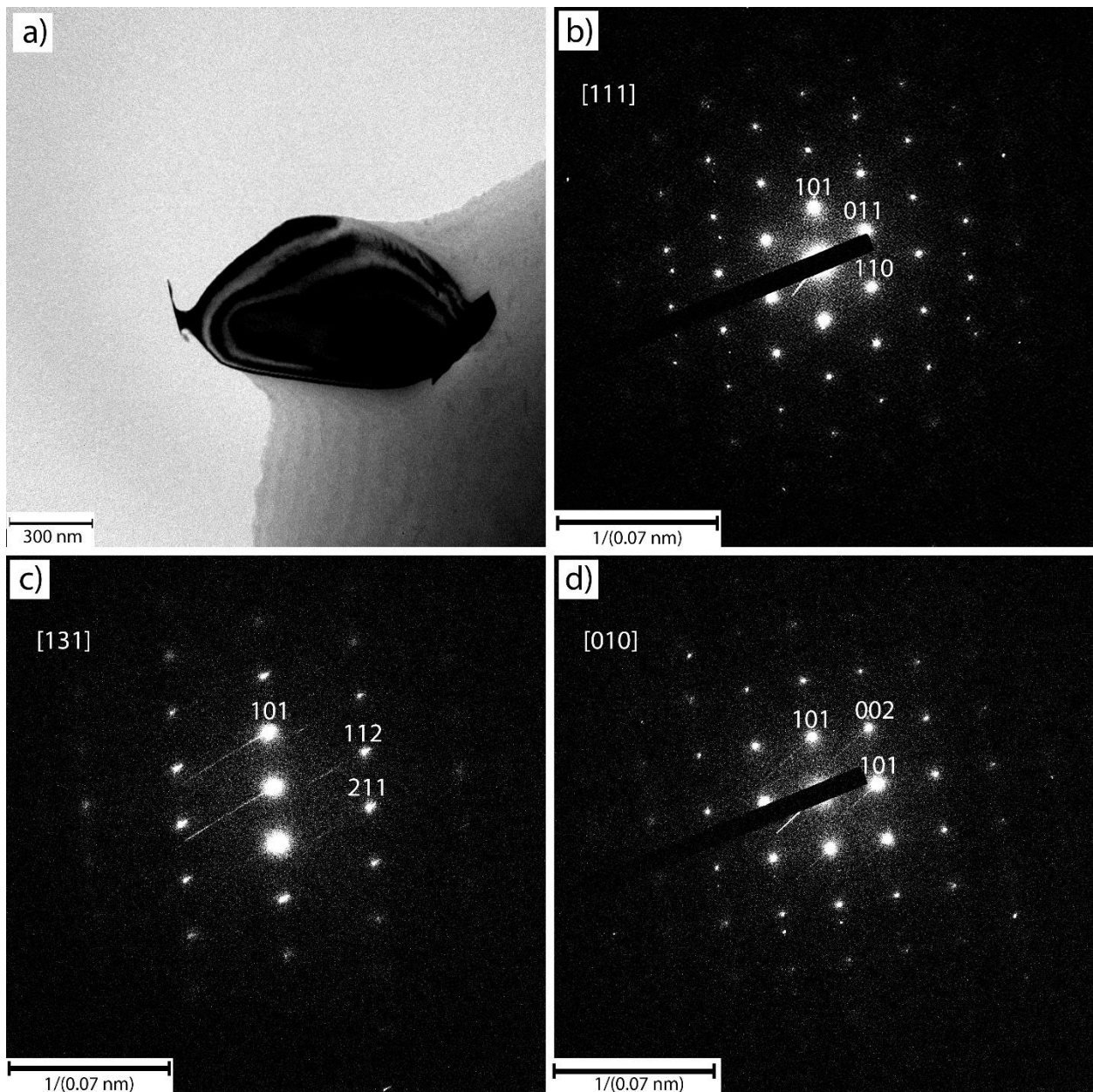


Figure 31: Images used to verify the presence of secondary δ -ferrite phase in the investigated DLD SS316L-Si. a) A speck of δ -ferrite with globular morphology, b) SAD pattern of [111] projection, c) SAD pattern of [131] projection and d) SAD pattern of [010] projection.

The secondary phase appeared with three different types of morphology: globular specks, lathy and vermicular, where the vermicular has a more soft and smooth appearance while the lathy is more needle shaped. The classification system proposed by Takalo et al. [48] which is described in the literature study in sub-chapter 2.4.6 can be applied, this place the DLD SS316L-Si in both “Microstructural type” A and B. Considering that the chromium-nickel equivalent ratio is 1.47 which lie right on the borderline between the classes this is not extraordinary. Closer to the base material the globular morphology prevails, and the δ -ferrite is located mainly at the cellular and dendritic boundaries. This morphology can be attributed to the repeated thermal cycling of the deposited material. This periodical heat input

dismembers the initial vermicular and lathy structures into smaller globular specks of δ -ferrite. This has been characterized by David et al. [86] to be a result of shape instabilities for lathy and thin δ -ferrite when exposed to high cyclic temperatures. Further from the base material, in areas that has received less cyclic temperature variation, the δ -ferrite has kept more of its initial lathy and vermicular morphology which underlines the assertion. Through the study of the SAD pattern there could not be found any distinct orientation relationship between the austenite and globular or vermicular δ -ferrite, while there seem to be an orientation relationship between the austenitic matrix and the lathy δ -ferrite. To get an idea of the quantity of- and where the secondary phase occurs, a high magnification EBSD phase map and its image quality map is presented in Figure 32. The figure display that the deposited SS316L-Si consist mainly of the austenitic phase, and that the secondary δ -ferrite with vermicular and globular morphology is located in the interdendritic regions and along sub-grain boundaries. Figure 32 clearly show an increase of δ -ferrite in the triple junctions. The phase map also reveals that the quantity of the secondary phase in this region is 2.5% which is in agreement with the ferrite concentration indicated by the Schaeffler diagram by the use of chromium- and nickel equivalents which indicated $\sim 5\%$ ferrite.

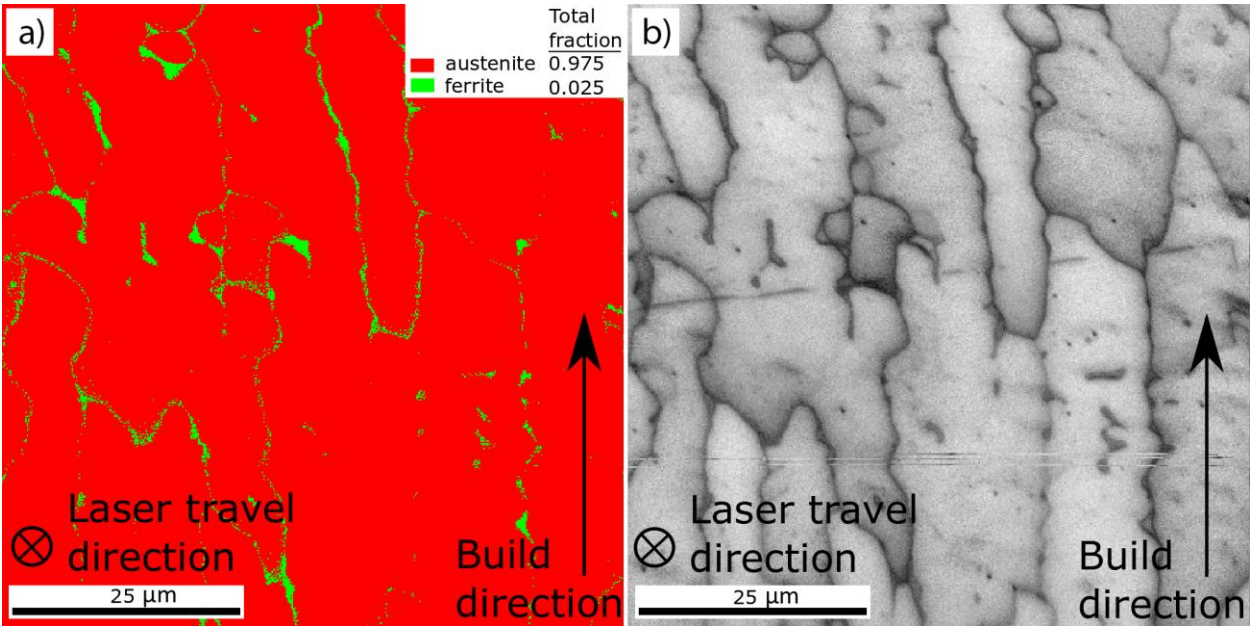


Figure 32: High magnification EBSD showing the location and total fraction of δ -ferrite in the austenitic matrix for sample 4. a) phase map with austenite presented in red and δ -ferrite in green and b) the corresponding image quality map.

Figure 33a) is a SEM-graph showing vermicular and some globular morphology of the δ -ferrite and an indication for point analysis of composition with number 1, while the point of compositional extraction over the general austenitic matrix is indicated with number 2. The

results together with the powder material are given in Table 9. The table reveal that the δ -ferrite is enriched in chromium, molybdenum and silicon all of which are strong ferrite stabilizers thus giving an indication of how the secondary phase has solidified and show a composition very similar to other studies of printed SS316L [7]. While the austenitic matrix has a composition more comparable to the powder material. Figure 33b) show the lathy morphology of the δ -ferrite as it appeared in TEM with high magnification, while Figure 33c) show a line scan close to a fusion boundary containing multiple dendrites with a continuous network of vermicular and globular δ -ferrite in the interdendritic- and sub-grain boundary region. The figure shows how the nickel and iron content drops between the dendrites, while the chromium, silicon and molybdenum increase.

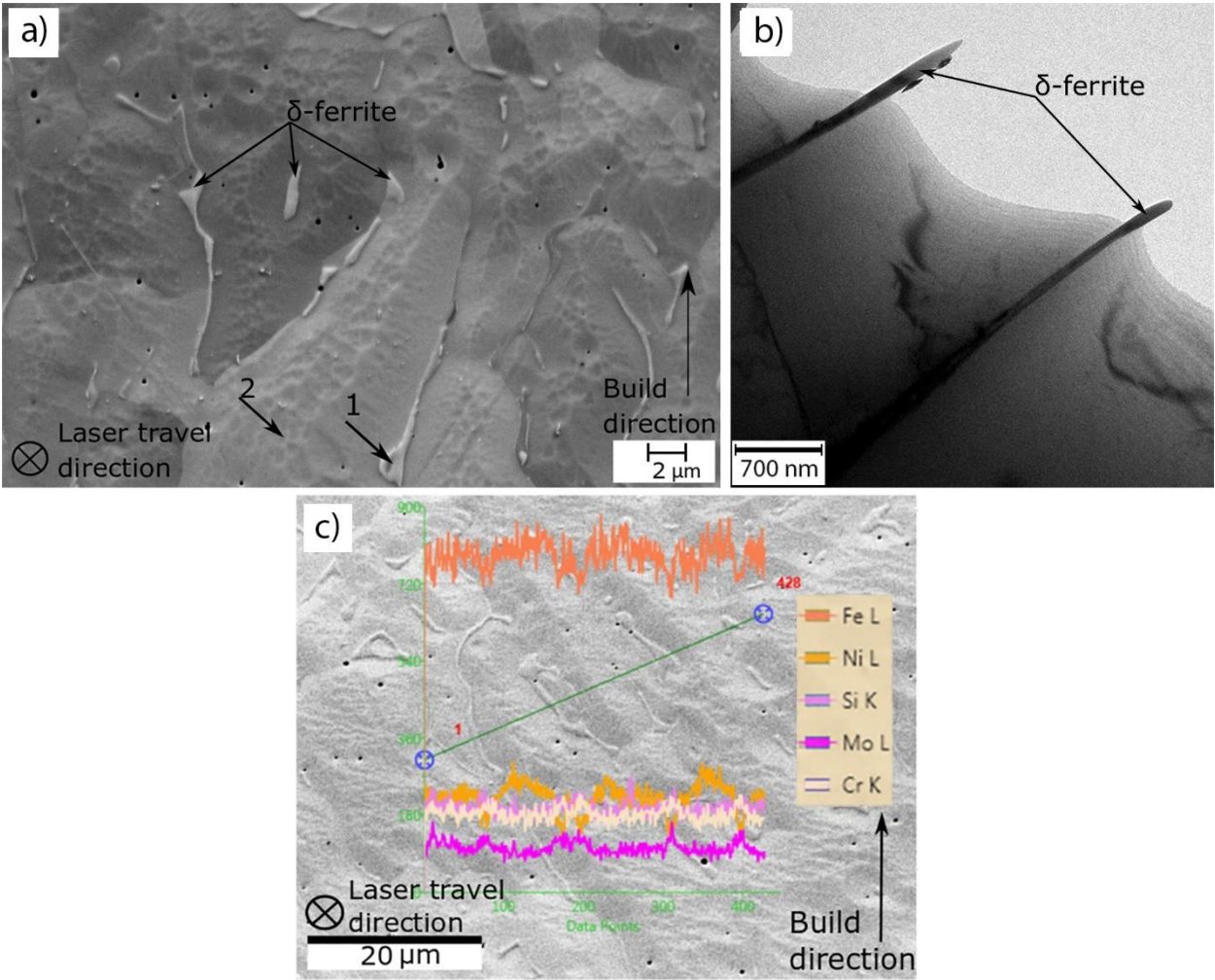


Figure 33: δ -ferrite found in deposited SS316L-Si. a) SEM-graph taken with secondary electron detector showing vermicular and globular morphologies of the δ -ferrite from sample 1. Arrow and numbering indicating location of point extraction of chemical composition presented in Table 9. b) TEM-graph showing δ -ferrite with lathy morphology in sample 3. c) EDS line scan done with EDAX in a fusion region between two layers showing the compositional fluctuations over vermicular and globular δ -ferrite in interdendritic and sub-grain boundary regions in sample 3.

Table 9: Chemical composition given in wt% for extraction points indicated in Figure 33a).

| # | C | Mn | Si | Cr | Ni | Mo | Fe |
|-----------------------|------|-----|-----|------|------|-----|---------|
| 1 [wt%] | N/A | 0.0 | 5.0 | 32.2 | 6.5 | 7.1 | 49.2 |
| 2 [wt%] | N/A | 0.4 | 2.1 | 18.0 | 12.5 | 1.7 | 65.1 |
| Powder material [wt%] | 0.03 | 1.0 | 2.3 | 17.0 | 12.0 | 2.5 | Balance |

As the initial austenitic dendrites grow some elemental segregation occurs. In the remaining melt in the interdendritic region at a point the chemical composition reaches a certain balanced value between austenitic and ferritic stabilizing elements which leaves the solid-liquid interface at a eutectic region in the phase diagram. Thus, as the austenitic dendrites grow some of the remaining melt in the cellular and interdendritic region contain higher concentrations of ferrite stabilizing elements from which the δ -ferrite is formed, placing it in the cellular and dendritic boundaries and giving it a eutectic character with austenite as primary phase [48]. The ferrite-to-austenite solid-state transformation is small in deposited SS316L-Si as the δ -ferrite has a stable composition due to the effects of segregated alloying elements [87]. Also, no variation in concentration of δ -ferrite was seen in the different layers indicating that the regular reheating does not initiate solid-state transformation, it only affects its morphology. The presence of δ -ferrite in the material has both advantageous and adverse effects. At higher temperatures the δ -ferrite has a higher ductility than the general austenitic matrix which helps the material to relieve some of the thermal stresses acquired during multipass deposition, which is beneficial to reduce hot cracking as demonstrated by Mozhi et al. [88]. Which might have been the case with the studied deposited SS316L-Si as no cracks were found. It will also assist to define grain boundaries during solidification. As deposited material tends to form excessively large grains this is beneficial to the mechanical properties. On the more negative side of the existence of a secondary phase in the deposited SS316L-Si is its influence on corrosion properties. The δ -ferrite/austenite boundary interfaces have a tendency to attract phosphor and sulphur due to the ferritic body-centred cubic structure which has more room to host such elements. These micro-heterogeneities in the matrix can result in advantageous sites for corrosive attacks [89].

5.1.5 Dislocations

A detailed analysis performed in TEM revealed the presence of dislocations in the proximity of sub-grain boundaries, and also within the sub-grains as can be seen in the representative bright-field TEM images in Figure 34a) and b) which respectively show sub-grain boundaries and a triple junction sub-grain boundary with δ -ferrite with globular morphology located in the connecting point. The sub-grains exhibit low-angle boundaries, and has dimensions ranging from a couple of microns to a few tens of microns, which was also seen in the inverse pole figures from the EBSD images in Figure 29 in sub-chapter 5.1.3 . Figure 34 present dislocation tangling and some clustering, especially surrounding the δ -ferrite. Nevertheless, the larger melt pool and subsequent slower cooling rate has voided the material from forming the large and intricate dislocation networks seen in SS316L printed by other methods with higher cooling rates [90, 91]. The lower density of dislocations found in the study indicate that the deposited material experience some relaxation of the residual stresses and localized strain during solidification and the following reheating during next deposited layer [92]. The amounts of dislocations seen is also a result of the low misorientation angles between the grains in the material, as higher misorientation angles leads to an increase in dislocation density [13].

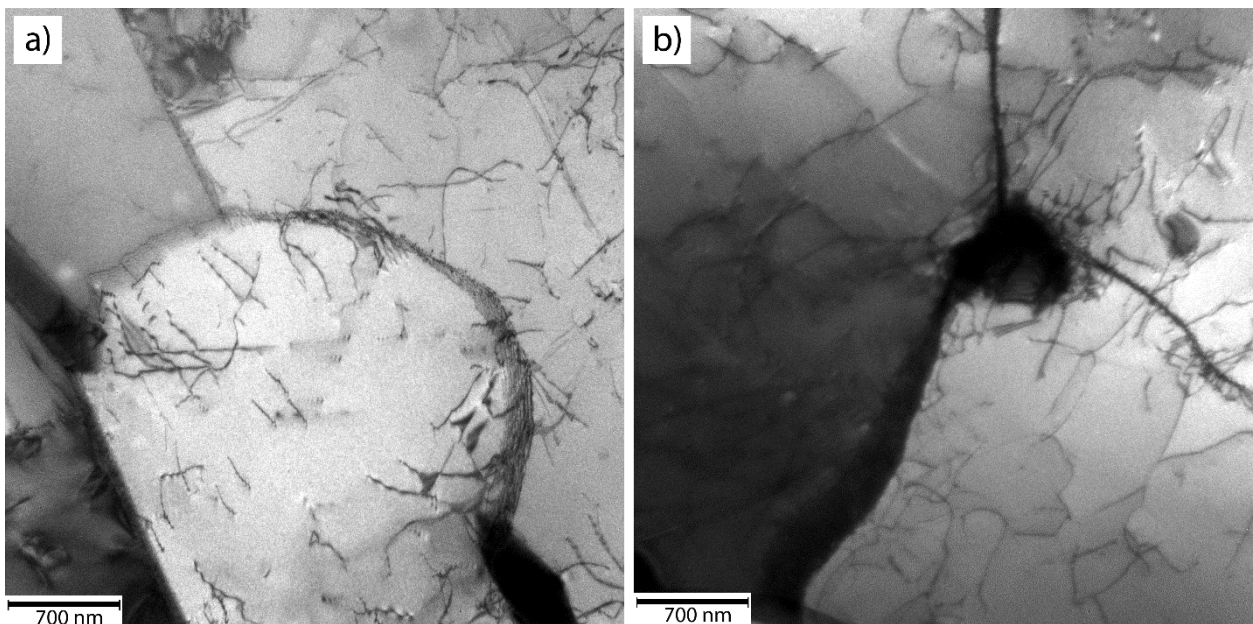


Figure 34: Bright field TEM-graphs from sample 3 showing: a) sub-grain boundaries and dislocations within the sub-grains. And b) a sub-grain triple junction with a speck of globular δ -ferrite which has formed in the middle surrounded by dislocations.

5.1.6 Silicate inclusions

When applying high magnification in the TEM it revealed circular nano-inclusions dispersed in the material. EDS area analysis while using scanning transmission electron microscope (STEM) showed that the circular inclusions are dominated by oxygen, silicon and aluminium. The morphology of the inclusions can be seen in Figure 35, while chemical composition is presented in Table 10. Here it must be noted that the thickness of the sample will have a significant influence on the revealed elemental quantities, and that the unknown thickness of the sample will give a measuring error which is hard to determine. Regardless Table 10 gives an indication of the chemical composition. Both Table 10 and Figure 35 reveal that the inclusion is a form of silicate in the size range of 300 nm in diameter. Silicates has a high viscosity in the melted state, thus to reduce its surface tension it forms the characteristic spherical shape. The silicate nano-inclusion does not dissolve in the steel as the surface tension gives it low wettability [14].

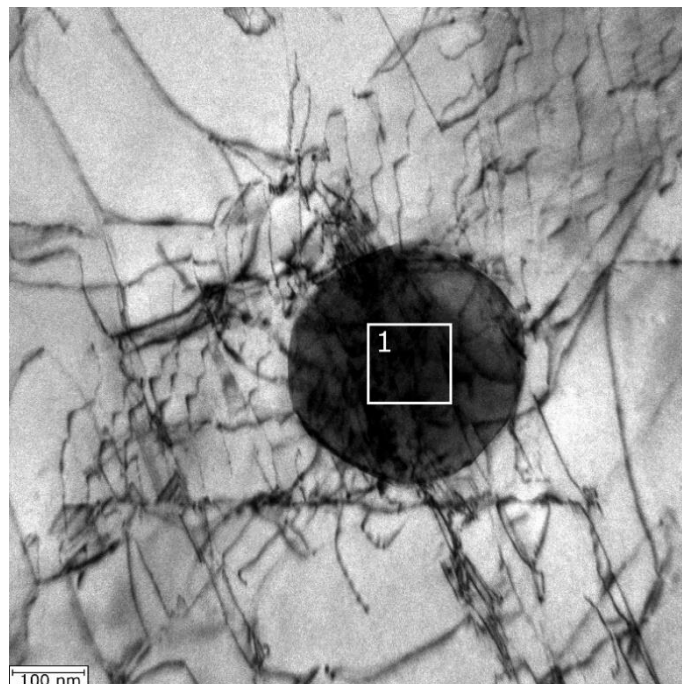


Figure 35: TEM-graph showing morphology of a nano-inclusion in the form of silicate found dispersed in the deposited material together with large dislocation concentrations surrounding the inclusions. The white square indicate area for extraction of chemical composition.

Table 10: Chemical composition of silicate shown in Figure 35.

| # | Si | O | Al | Cr | Fe | Ni |
|---------|------|------|-----|-----|-----|-----|
| 1 [wt%] | 18.1 | 63.8 | 7.0 | 1.8 | 8.0 | 1.3 |

The concentration of oxygen in the inclusion is peculiar, as the powder material used during the deposition process is generated by inert gas atomization and during deposition the inert gas is deployed to remove the possibility of oxygen reaching the melt pool. It is therefore speculated that the oxygen comes from the oxide layer formed around the powder particles before deposition by the chromium, and that during melting some of the oxygen binds to the silicon forming the observed silicates. When it comes to the aluminium it may be a result of contamination of the powder material. Figure 35 also show that the inclusion is surrounded by large amounts of dislocations. During solidification of the melt pool while the silicates form, they generate local stress in the steel matrix. Due to differences in coefficient of thermal expansion between the two, usually being $\sim 5.5 \times 10^{-7}/\text{C}^\circ$ for silicates and $1.6 \times 10^{-5}/\text{C}^\circ$ for the SS316L, this will generate a tensile stress on the steel matrix in close proximity to the inclusions and subsequently a compressive stress on the silicate [14]. These variational stress fields in the matrix may give rise to the large concentration of dislocations seen and consequently this contributes to an increase in hardness of the material and improve the mechanical properties [93]. The occurrence of silicates may initiate the possibility of generating in-situ dispersion-strengthened components by DLD [14]. When it comes to the downside of silicate inclusions in the material, their presence inoculates sites for possible pitting corrosion [94, 95].

5.2 Defects

5.2.1 Element segregation

Thorough study of the samples in SEM revealed segregated elements that formed smooth and irregular concentrations along grain boundaries, as presented in Figure 36. The arrows and numbering indicate points of composition extraction. The chemical composition is presented in Table 11. The table show how these areas contain large amounts of chromium and a smaller amount of molybdenum and silicon.

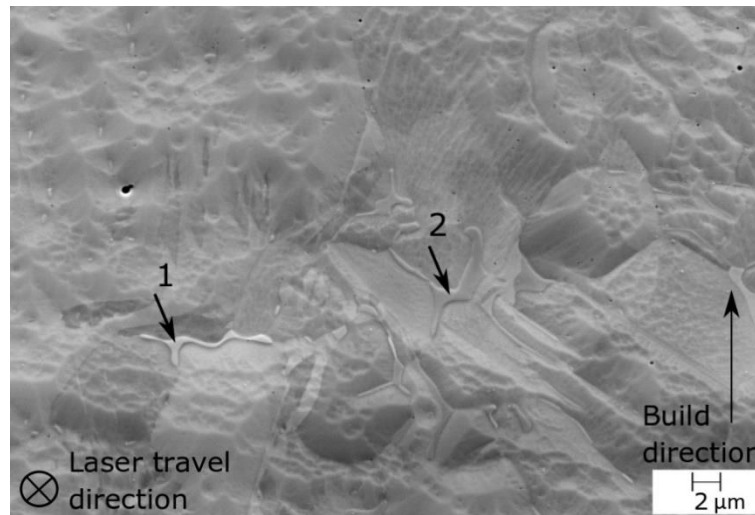


Figure 36: SEM graph taken with secondary electron detector showing segregation of alloying elements forming smooth and irregular concentrations along grain boundaries in sample 3.

Table 11: Chemical composition given in wt% for extracted points 1 and 2 indicated in Figure 36.

| # | Mn | Si | Cr | Ni | Mo | Fe |
|---------|-----|-----|------|-----|-----|------|
| 1 [wt%] | 0.2 | 1.6 | 35.8 | 2.9 | 0.9 | 58.6 |
| 2 [wt%] | 0.0 | 1.6 | 43.4 | 0.9 | 1.1 | 53 |

This reveals that during the solidification process, amounts of heavier alloying elements experience segregation. The seclusion of amounts of molybdenum and chromium, the two alloying elements responsible for 316L stainless steels impressive corrosive aptitude, will affect the materials ability to resist corrosion as the alloying elements are drained from the surrounding area. Segregation of heavy elements during solidification in additive manufacturing processes like selective laser melting and laser engineered net shaping® has been previously observed [7, 14], this is also a known problem in welding of 316L stainless steel [96]. Mechanisms for segregation in welds as described by Banovic et al. [51] can be applied here; when the heat input increase and the cooling rate decrease, the dendrite size

will increase. In the solute there will exist a fluctuation in element distribution. As the weld pool increase the distance which the elements must travel to compensate for the difference also increase. Molybdenum and chromium which has a low diffusion rate in face-centred cubic austenite compared to manganese and nickel, will be forced to segregate into the liquid phase in the gradually solidifying melt pool. As more and more of the solute solidifies, some areas will be left impoverished and some areas will be enriched as the low diffusion rate does not allow for the elements to diffuse back into the solid to compensate for this inhomogeneous distribution of alloying elements. Thus, as the dendrites continue to grow, it will be surrounded by some areas enriched in alloying elements. This also means that the element segregation can be reduced by reducing heat input or by concentrating the laser beam spot size as this will increase the cooling rate and solidification velocity locking the elements in place.

Extensive investigation did not reveal any carbide formation on the grain boundary interfaces. Showing that the continuous heat cycles did not leave the deposited material sensitized.

5.2.2 Pores and voids

The investigation revealed an even distribution of spherical pores throughout the samples as shown in Figure 37, which is an excerpt from the cross section of sample 1 and 3.

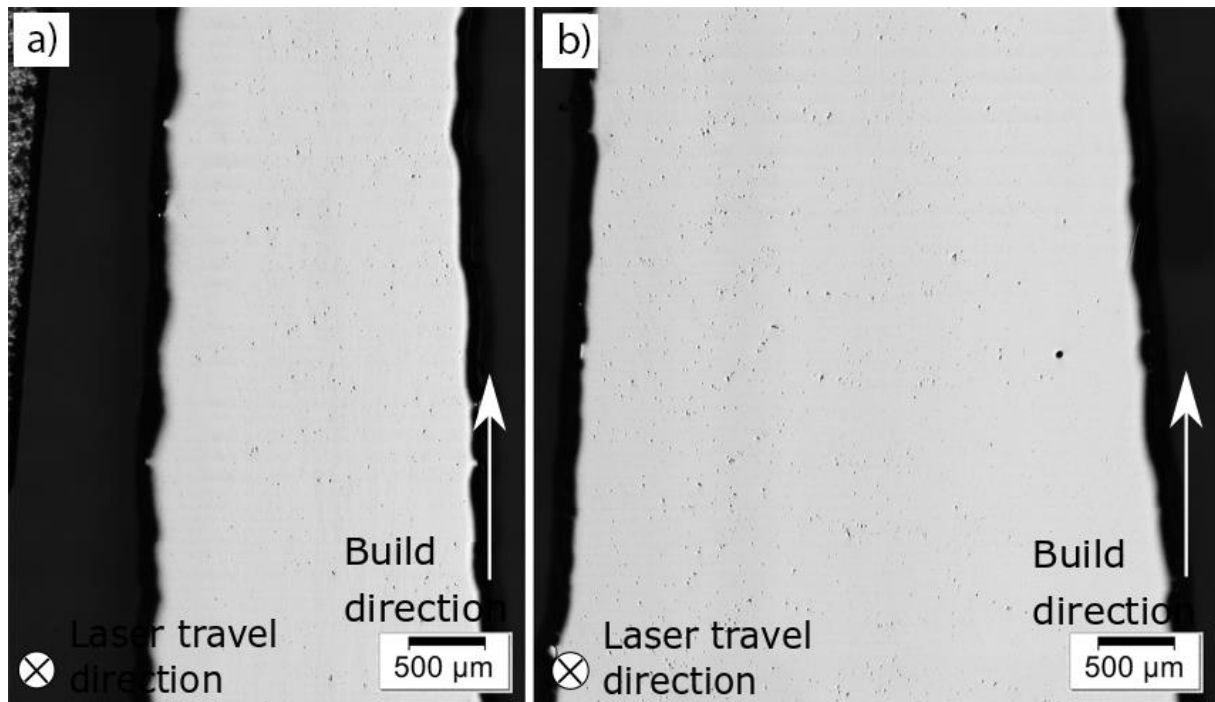


Figure 37: Micrographs showing a uniform distribution of spherical pores for cross-sectional cuts: a) sample 1, and b) sample 3.

Sample 1 exposed an area with elongated binding defects adjacent to the base material which would be detrimental to the mechanical properties as it would initiate crack formation due to high stress concentrations in this region during loading [97]. No such areas were found in sample 3, further indicating that sample 1-2 has received an improper heat input and also showing the negative effects of not carefully following cleaning procedures for the base material pre-deposition. Figure 38a) show the elongated binding defects found in sample 1.

The formation of pores and layered voids depend on the combination of process parameters, the thermal coefficient of base material and if the utilized powder material is porous [13]. As both samples contained a uniform distribution of spherical pores it would be possible to ascribe some of the pore formation to entrapped gas. As the argon gas used to create an inert environment for the process is non-soluble in steels, it would create spherical pores if it is caught up in the melt pool [98, 99]. A study of the plane cut along the laser travel direction of sample 4 revealed layered voids, as shown in Figure 38b), this was also the case for sample 2. While no layered voids were found in the cross-sectional samples.

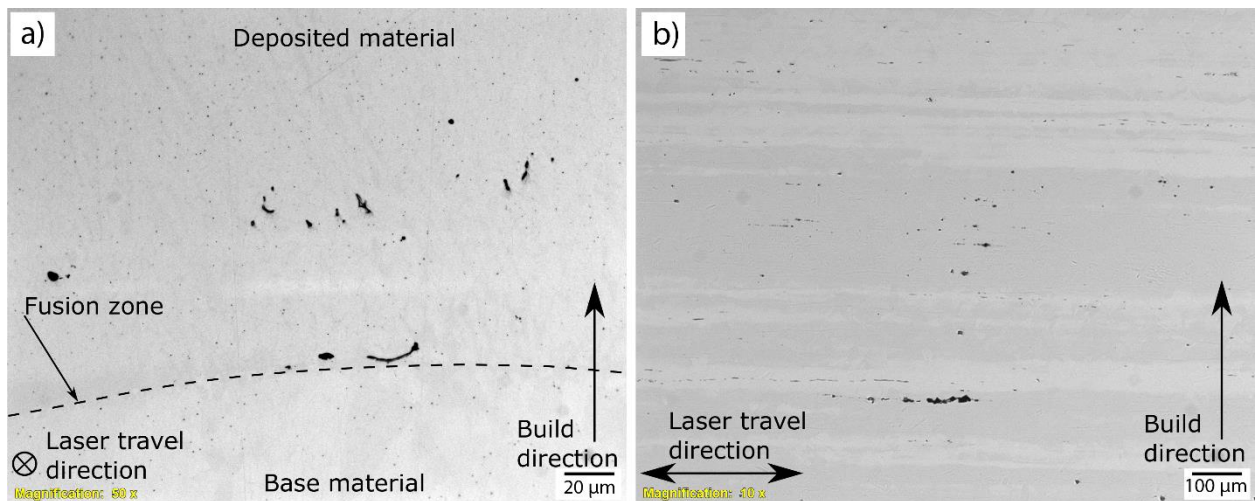


Figure 38: Non-spherical voids observed. a) Elongated and sharp voids found adjacent to fusion zone between deposited- and base material in the non-cleaned sample 1. b) Layered voids following laser travel direction as seen in sample 4.

According to a study done on clad material by Sun et al. [100] such inter-track porosity, as they called it, has a higher tendency of forming with fine powder material in the range of 40-140 μm . And that the voids will start to appear if the laser energy input is insufficient to melt all the powdered material captured in the melt pool. A study done by Yu et al. [101] on laser deposition using a fractal deposition pattern showed that the overlap between each deposited layer should be at least 50% to avoid pore defects.

Analysis of the pore content done on micrographs in ImageJ presented a low porosity percentage for the cross sections. The software eased the pore inspection through grayscale images. Results of the calculations are given in Table 12 and indicate a material density above 99.5% for both samples. As the analysed surface area is at least 50% of the total cross-sectional area this is a sufficient indication of the entire sample porosity.

Table 12: Sample density results over total pore area given from software ImageJ for the cross-sectional samples 1 and 3.

| Sample # | Density [%] | Porosity [%] |
|----------|-------------|--------------|
| Sample 1 | 99.61 | 0.39 |
| Sample 3 | 99.54 | 0.46 |

5.3 Hardness evaluation

To investigate the influence that build direction has on the hardness of the deposited SS316L-Si, hardness measurements were performed. The results from the measurements normal- and parallel to the build direction for all four samples is given in Figure 39, while the complete hardness results are given in Appendix D. The results revealed small variations in hardness value for either measuring direction. Samples 1 and 2 had the largest variation in hardness value of 6HV between the parallel and normal measurements, with highest values for parallel direction. While sample 3 and 4, which is produced with more optimized process parameters show almost no variation for both the normal- and parallel measurements to build direction.

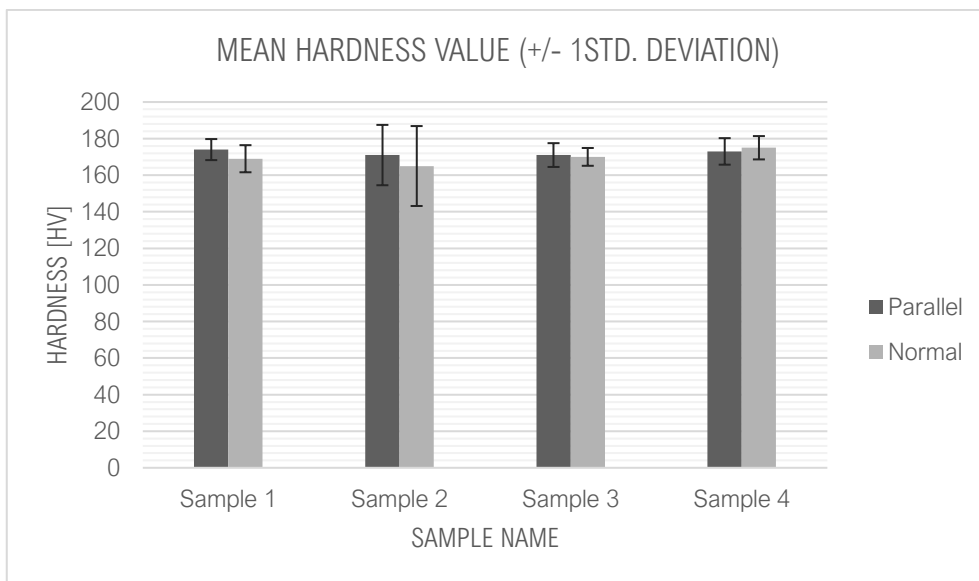


Figure 39: Plot over average hardness measurements for all four samples normal- and parallel to build direction with +/- 1 standard deviation.

The highest average hardness value was found in sample 4 in the normal direction with a value of 175 ± 6 HV, the lowest average hardness value was 165 ± 22 HV for sample 2 also in the normal direction. The lowest of these extremal points is higher than the average hardness value for conventionally manufactured SS316L which has a value of 155 HV [31]. This increase in hardness is assumed to be attributed to the δ -ferrite, the silicate inclusions and their resulting dislocations and the segregated alloying elements found in the material. As their presence inside grains and along grain boundaries acting like road-blocks, they have the possibility to repress and pin the dislocation movement during plastic deformation forming dislocation pile-ups. Thus, their existence leads to the need of increased force to achieve deformation [102, 103]. The large standard deviation seen in sample 2 is attributed

to the values extracted from the top of the deposited material, as this area was thinner than the rest of the sampled material due to the geometry of the specimen. This may have influenced the indentation as a result of more plastic deformation and a lower hardness value. The proportional hardness values for parallel to- and normal to build direction is attributed to the rather uniformity seen in the microstructure. Regardless of the complexity, the lack of severe dislocation networks and the homogeneous distribution of δ -ferrite has given the material a more coherent resistance to plastic deformation in all directions than seen with other printing techniques [7].

Figure 40 show the hardness value profile measured parallel to build direction for all four samples crossing the heat-affect zone and going 3 mm into the base material. The profile clearly shows the sudden decrease in hardness value for sample 2 which resulted in the large standard deviation.

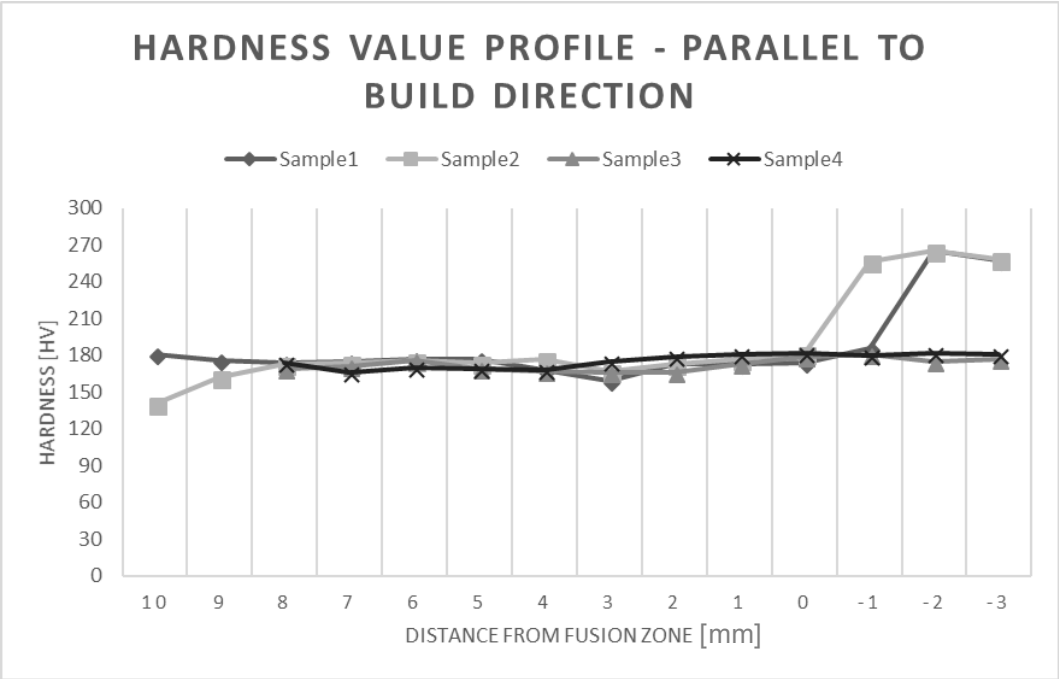


Figure 40: Plot of hardness value vs. distance from heat-affected zone for all four samples parallel to build direction. Base material located on the right side of 0.

The figure show that no local brittle zone was found even though each layer had a local heat-affected zone. The small fluctuations in hardness value is contributed to variations in indentation force from the machine, local variations in microstructure and defects. There is a slight increase in hardness value starting in the deposited material about 3 mm from the fusion zone towards the base material, this increase would be the result of the base material having room temperature in the beginning of the deposition process resulting in thermal

stresses which has not been completely eradicated during the subsequent deposited layers. The decrease in hardness seen for sample 3 and 4 after the fusion zone is due to the increase in grain size in HAZ and also the larger size of the equiaxial grains in the base material than in the deposited material. The increase in hardness seen after HAZ for sample 1 and 2 is due to the SS304 base material.

The results from the hardness measurements describes the microstructural homogeneity of the deposited material, while the hardness values found in the investigation is in accordance with the results found in earlier studies and literature for direct laser deposited 316L stainless steel [104, 105].

5.4 Further research

For future studies it would be of great interest to investigate the mechanical properties and compare ductility and tensile strength to conventionally manufactured SS316L. To assess the material anisotropy in all three dimensions would also be of interest, to investigate how much the mechanical properties are affected by the solidification texture and inter-track porosity. There is work to be done in analysis of corrosion resistance of the DLD SS316L-Si parts as it is of significance to determine the corrosion resistance and compare it to both conventionally manufactured- and welded SS316L to see how the secondary phase, the silicates and element segregation has influence the corrosion properties.

As a final point, the production parameters should be studied. It is highly relevant for the mechanical properties to determine the optimum production parameters which abrogate the shown inter-track porosity.

CHAPTER 6

SUMMARY AND CONCLUSIONS

The general macrostructure of the Direct Laser Deposited SS316L-Si on base material SS304 and SS316L is comprised of respectively 18 and 15 layers and 2 and 3 lines in latitudinal direction. Two main samples were extracted by each as given in Table 13.

Table 13: Table describing orientation and sample number of extracted samples from the deposited material with respect to the laser travel direction.

| Material | Sample number | Orientation w.r.t. LTD |
|---------------------|---------------|------------------------|
| SS316L-Si on SS304 | 1 | Cross section |
| | 2 | Plane |
| SS316L-Si on SS316L | 3 | Cross section |
| | 4 | Plane |

Measurements of the secondary dendritic arm spacings revealed cooling rates of 3700 K/s for samples 1 and 2 and 4400 K/s for samples 3-4. SDAS also revealed a variation in cooling rate within each melt pool which has given rise to a complex microstructure for each layer resulting in three main zones; an approximately 50 μm band of cellular- and planar dendrites occurs due to a slower solidification rate initially as the pre-deposited material still contains excess heat. This continues into the main zone which contains temperature gradient guided columnar dendrites. The last zone on top is a local heat-affected zone of approximately 100 μm comprised of a coarser microstructure. Investigation of each layer revealed that the deposited centre line, due to being surrounded by high temperature material has developed more clusters of cellular dendrites than the material deposited along the edges. This difference starts from N5 and continues until the penultimate layer N14 where it again contains a more homogenous mixture of cellular- and columnar dendrites. The columnar dendrites have fused its secondary dendritic arms together forming large columnar grains which continuous epitaxially in some cases over several layers. The grains are on average 430 μm in longitudinal- and 50 μm in latitudinal directions containing multiple low angled sub-grains. The dendrites have formed preferentially in $\langle 001 \rangle$ direction giving rise to a textured material which will result in some anisotropy. The investigation confirmed the existence of

under 5% δ -ferrite in the deposited and regularly austenitic SS316L-Si which has solidified under eutectic conditions in the interdendritic and in the sub-grain boundary areas. The δ -ferrite revealed higher concentrations of chromium, molybdenum and silicon than the matrix, all of which are strong ferrite stabilizers. The secondary phase has voided the continuous heat cycles of the material from hot cracking. The samples can be categorized in "Microstructural type" A and B simultaneously having δ -ferrite with globular, vermicular and lathy morphologies. The initial vermicular and lathy configuration has been broken into more globular pieces by the cyclic heating. Study of deeper microstructural features revealed none of the severe dislocation networks seen in other printing techniques with more rapid solidification, indicating that the larger melt pool and the protracted heating has relaxed some of the residual stresses commonly seen in additive manufacturing of 316L stainless steel.

Grain boundaries containing smooth and irregular clusters of segregated alloying elements such as chromium, molybdenum and silicon was observed. While circular nano-sized oxygen-, silicon- and aluminium rich silicates was observed dispersed in the material, no carbides was found along grain- and sub-grain boundaries. The deposition process has yielded >99.5% dense material containing mainly spherical pores due to entrapped non-soluble gas. In the plane of laser travel direction and as a result of low energy input and powder particle size, inter-track- and bonding defects was observed.

Bonding to the base material is strong in the case of SS316L-Si on SS316L. While some binding defects was observed for SS316L-Si on SS304 as this base material had not received a proper cleaning procedure prior to the material deposits. Both cases resulted in solid epitaxially growth of some grains to the base material. The relatively low and concentrated heat input has given a small HAZ in the base material with only a slight grain coarsening in a 100 μm band followed by finer grains which gradually blend with the unaffected material. Hardness measurements showed little variation in the deposited materials ability to resist plastic deformation normal- and parallel to build direction, and gave results conforming to previously reported studies of deposited SS316L.

The study has led to the following conclusions:

1. The Direct Laser Deposition of SS316L-Si resulted in almost fully dense (>99.5%) components containing a complex microstructure of a duplex nature with primary austenite- and secondary δ -ferrite phases in the interdendritic and sub-grain boundaries. The δ -ferrite has been beneficial and voided the material from hot cracking during the thermal cycles.
2. The fusion zone was found to be defect free, when the cleaning procedure was followed, and the deposited material formed a solid metallurgical bond with epitaxial grain growth to the base material.
3. Results of hardness testing are comparable to previous studies on deposited SS316L and are slightly elevated compared to commercially available annealed 316L stainless steel. While the hardness profile parallel to build direction showed little fluctuations and thus did not reveal any brittle zones.
4. The lack of material for mechanical- and corrosion testing makes it difficult to exactly conclude how the Direct Laser Deposited material will behave in a stressed environment. It can still be concluded that the DLD SS316L-Si contains anisotropic mechanical properties due to preferential grain growth leading to a textured material, together with inter-track porosity in the laser travel direction. Additionally, the enrichment of molybdenum and chromium in the interdendritic and sub-grain boundaries due to the duplex solidification, together with element segregation will have an adverse effect on the components ability to resist pitting corrosion.
5. The results of the investigation may serve as a guide to improve the process parameters to generate fully dense components without any inter-track porosity.
6. Occurrence of silicate nano-inclusions may initiate the possibility of generating in-situ dispersion-strengthened Direct Laser Deposited components.

CHAPTER 7

REFERENCES

- [1] J. P. Kruth, M. C. Leu, and T. Nakagawa, "Progress in Additive Manufacturing and Rapid Prototyping," *CIRP Annals*, vol. 47, no. 2, pp. 525-540, 1998/01/01/ 1998.
- [2] J. Giannatsis and V. Dedoussis, "Additive fabrication technologies applied to medicine and health care: a review," *The International Journal of Advanced Manufacturing Technology*, journal article vol. 40, no. 1, pp. 116-127, January 01 2009.
- [3] L. Nickels, "AM and aerospace: an ideal combination," *Metal Powder Report*, vol. 70, no. 6, pp. 300-303, 2015/11/01/ 2015.
- [4] Y. Song, Y. Yan, R. Zhang, D. Xu, and F. Wang, "Manufacture of the die of an automobile deck part based on rapid prototyping and rapid tooling technology," *Journal of Materials Processing Technology*, vol. 120, no. 1, pp. 237-242, 2002/01/15/ 2002.
- [5] N. Guo and M. C. Leu, "Additive manufacturing: technology, applications and research needs," *Frontiers of Mechanical Engineering*, journal article vol. 8, no. 3, pp. 215-243, September 01 2013.
- [6] T. J. Prater *et al.* (2016, 01.06). *Summary Report on Phase I Results from the 3D Printing in Zero G Technology Demonstration Mission, Volume I*. Available: <https://ntrs.nasa.gov/search.jsp?R=20160008972>
- [7] M. Ziętała *et al.*, "The microstructure, mechanical properties and corrosion resistance of 316L stainless steel fabricated using laser engineered net shaping," *Materials Science and Engineering: A*, vol. 677, pp. 1-10, 2016/11/20/ 2016.
- [8] K. Zhang, W. Liu, and X. Shang, "Research on the processing experiments of laser metal deposition shaping," *Optics & Laser Technology*, vol. 39, no. 3, pp. 549-557, 2007/04/01/ 2007.
- [9] G. Yang *et al.*, "Laser solid forming Zr-based bulk metallic glass," *Intermetallics*, vol. 22, pp. 110-115, 2012/03/01/ 2012.
- [10] S. M. Thompson, L. Bian, N. Shamsaei, and A. Yadollahi, "An overview of Direct Laser Deposition for additive manufacturing; Part I: Transport phenomena, modeling and diagnostics," *Additive Manufacturing*, vol. 8, pp. 36-62, 2015/10/01/ 2015.
- [11] G. Kalinin *et al.*, "Assessment and selection of materials for ITER in-vessel components," *Journal of Nuclear Materials*, vol. 283-287, pp. 10-19, 2000/12/01/ 2000.

- [12] S. Ford and M. Despeisse, "Additive manufacturing and sustainability: an exploratory study of the advantages and challenges," *Journal of Cleaner Production*, vol. 137, pp. 1573-1587, 2016/11/20/ 2016.
- [13] A. Yadollahi, N. Shamsaei, S. M. Thompson, and D. W. Seely, "Effects of process time interval and heat treatment on the mechanical and microstructural properties of direct laser deposited 316L stainless steel," *Materials Science and Engineering: A*, vol. 644, pp. 171-183, 2015/09/17/ 2015.
- [14] K. Saeidi, X. Gao, Y. Zhong, and Z. J. Shen, "Hardened austenite steel with columnar sub-grain structure formed by laser melting," *Materials Science and Engineering: A*, vol. 625, pp. 221-229, 2015/02/11/ 2015.
- [15] J. D. Majumdar, A. Pinkerton, Z. Liu, I. Manna, and L. Li, "Microstructure characterisation and process optimization of laser assisted rapid fabrication of 316L stainless steel," *Applied Surface Science*, vol. 247, no. 1, pp. 320-327, 2005/07/15/ 2005.
- [16] A. J. Sedriks, *Corrosion of stainless steels*, 2nd ed. ed. (Corrosion monograph series). New York: Wiley, 1996.
- [17] S. V. Muley, A. N. Vidvans, G. P. Chaudhari, and S. Udainiya, "An assessment of ultra fine grained 316L stainless steel for implant applications," *Acta Biomaterialia*, vol. 30, pp. 408-419, 2016/01/15/ 2016.
- [18] G. K. Lewis and E. Schlienger, "Practical considerations and capabilities for laser assisted direct metal deposition," *Materials & Design*, vol. 21, no. 4, pp. 417-423, 2000/08/01/ 2000.
- [19] B. Shyam, L. Frank, N. Joseph, and S. Todd, "Vision-based defect detection in laser metal deposition process," *Rapid Prototyping Journal*, vol. 20, no. 1, pp. 77-85, 2014.
- [20] G. J. Peacock, "Method of making composition horseshoes," United States of America, 1902. Available: <https://patents.google.com/patent/US746143#citedBy>.
- [21] L. Yang, *Additive manufacturing of metals : the technology, materials, design and production* (Springer series in advanced manufacturing). Cham: Springer, 2017.
- [22] K. B. Vamsi, R. L. B., O. C. G. W., T. Steven, B. Susmita, and B. Amit, "First demonstration on direct laser fabrication of lunar regolith parts," *Rapid Prototyping Journal*, vol. 18, no. 6, pp. 451-457, 2012.
- [23] P. Guo, B. Zou, C. Huang, and H. Gao, "Study on microstructure, mechanical properties and machinability of efficiently additive manufactured AISI 316L stainless steel by high-power direct laser deposition," *Journal of Materials Processing Technology*, vol. 240, pp. 12-22, 2017/02/01/ 2017.
- [24] J. Mazumder, "1 - Laser-aided direct metal deposition of metals and alloys A2 - Brandt, Milan," in *Laser Additive Manufacturing*: Woodhead Publishing, 2017, pp. 21-53.

- [25] J. O. Milewski, *Additive manufacturing of metals : from fundamental technology to rocket nozzles, medical implants, and custom jewelry* (Springer series in materials science). Cham: Springer, 2017.
- [26] T. S. Srivatsan and T. S. Sudarshan, *Additive manufacturing : innovations, advances, and Applications*. Boca Raton: CRC Press, 2016.
- [27] P. Rangaswamy *et al.*, "Residual stresses in LENS[®] components using neutron diffraction and contour method," *Materials Science and Engineering: A*, vol. 399, no. 1, pp. 72-83, 2005/06/15/ 2005.
- [28] I. Gibson *et al.*, *Additive Manufacturing Technologies 3D Printing, Rapid Prototyping, and Direct Digital Manufacturing*, 2nd ed. 2015. ed.: Springer New York : Imprint: Springer, 2015. [Online]. Available.
- [29] K. Kellens, M. Baumers, T. G. Gutowski, W. Flanagan, R. Lifset, and J. R. Duflou, "Environmental Dimensions of Additive Manufacturing: Mapping Application Domains and Their Environmental Implications," *Journal of Industrial Ecology*, vol. 21, no. S1, pp. S49-S68, 2017.
- [30] A. S. Metals. (15.01). *Stainless Steel - Grade 316L - Properties, Fabrication and Applications*. Available: <https://www.azom.com/article.aspx?ArticleID=2382>
- [31] A. A. S. M. Inc. (2018, 26.02). *AISI Type 316L Stainless Steel, annealed plate*. Available: <http://asm.matweb.com/search/SpecificMaterial.asp?bassnum=mq316p>
- [32] V. Narayanan, R. Sellamuthu, and R. Saravanan, "An Investigation on the Hardness and Wear Rate of Surface Alloyed AISI304 Stainless Steel with Ti using GTA as Heat Source," *Indian Journal of Science and Technology*, vol. 9, no. 34, 2016.
- [33] T. W. Institute. (2018, 18.01). *Weldability of materials*. Available: <https://www.twi-global.com/technical-knowledge/job-knowledge/weldability-of-materials-stainless-steel-020/>
- [34] W. D. Callister and D. G. Rethwisch, *Materials science and engineering*, 9th ed., SI Version. ed. Hoboken, N.J: Wiley, 2015.
- [35] H. K. D. H. Bhadeshia and R. W. K. Honeycombe, *Steels : microstructure and properties*, 3rd ed. ed. Amsterdam: Elsevier, 2006.
- [36] C.-C. Hsieh and W. Wu, "Overview of Intermetallic Sigma () Phase Precipitation in Stainless Steels," *ISRN Metallurgy*, vol. 2012, p. 16, 2012, Art. no. 732471.
- [37] J. H. Potgieter, P. A. Olubambi, L. Cornish, C. N. Machio, and E.-S. M. Sherif, "Influence of nickel additions on the corrosion behaviour of low nitrogen 22% Cr series duplex stainless steels," *Corrosion Science*, vol. 50, no. 9, pp. 2572-2579, 2008/09/01/ 2008.
- [38] Outokumpu, "Handbook of Stainless Steel," ed: Outokumpu Oyj, 2013.
- [39] T. S. S. I. Center. (2018, 10.01). *CORROSION: Chloride Stress Corrosion Cracking*. Available: <http://www.ssina.com/corrosion/stress-corrosion-cracking.html>

- [40] C. Thermodynamics. (2018, 14.01.2018). *Iron-Chromium (Fe-Cr) Phase Diagram*. Available: <http://www.calphad.com/iron-chromium.html>
- [41] T. I. M. Association, *Practical Guidelines for the Fabrication of Duplex Stainless Steels*. London, UK: the International Molybdenum Association (IMOA), 2014.
- [42] Sandvik. (2018, 18.01). *Ferrite content diagrams - Schaeffler diagram*. Available: <https://www.materials.sandvik/en/products/welding-products/welding-handbook3/ferrite-content-diagrams/#send-feedback>
- [43] X. Chen, J. Li, X. Cheng, B. He, H. Wang, and Z. Huang, "Microstructure and mechanical properties of the austenitic stainless steel 316L fabricated by gas metal arc additive manufacturing," *Materials Science and Engineering: A*, vol. 703, pp. 567-577, 2017/08/04/ 2017.
- [44] W. T. DeLong, "Ferrite in Austenitic Stainless Steel Weld Metal," *Welding Journal*, pp. 273-286, 1974.
- [45] T. W. Institute. (2018, 17.01). *Welding of austenitic stainless steels*. Available: <https://www.twi-global.com/technical-knowledge/job-knowledge/welding-of-austenitic-stainless-steel-103/>
- [46] N. Suutala, T. Takalo, and T. Moio, "Ferritic-austenitic solidification mode in austenitic stainless steel welds," *Metallurgical Transactions A*, journal article vol. 11, no. 5, pp. 717-725, May 01 1980.
- [47] M. Marya, V. Singh, S. Marya, and J. Y. Hascoet, "Microstructural Development and Technical Challenges in Laser Additive Manufacturing: Case Study with a 316L Industrial Part," *Metallurgical and Materials Transactions B*, journal article vol. 46, no. 4, pp. 1654-1665, August 01 2015.
- [48] T. Takalo, N. Suutala, and T. Moio, "Austenitic solidification mode in austenitic stainless steel welds," *Metallurgical Transactions A*, journal article vol. 10, no. 8, pp. 1173-1181, August 01 1979.
- [49] Sung-Yu Kim, Hyuk-Sang Kwon, and H. Kim, "Effect of delta ferrite on Corrosion Resistance of Type 316L Stainless Steel in Acidic Chloride Solution by Micro-droplet Cell," *Solid State Phenomena*, vol. 124-126, pp. 1533-1536, June 2007 2007.
- [50] A. Almar-Næss, *Metalliske materialer : struktur og egenskaper*, 4. utg. ed. Trondheim: Tapir, 2003.
- [51] S. W. Banovic, J. N. Dupont, and A. R. Marder, "Dilution and microsegregation in dissimilar metal welds between super austenitic stainless steel and nickel base alloys," *Science and Technology of Welding and Joining*, vol. 7, no. 6, pp. 374-383, 2002/12/01 2002.
- [52] S. G. Shiri, M. Nazarzadeh, M. Sharifitabar, and M. S. Afarani, "Gas tungsten arc welding of CP-copper to 304 stainless steel using different filler materials," *Transactions of Nonferrous Metals Society of China*, vol. 22, no. 12, pp. 2937-2942, 2012/12/01/ 2012.
- [53] A. BUSTREO. (2016, 18.01.2018). *All you need to know about the heat-affected zone*. Available:

<https://www.thefabricator.com/article/shopmanagement/all-you-need-to-know-about-the-heat-affected-zone>

- [54] W. F. Hosford, *Physical metallurgy*, 2nd ed. ed. Boca Raton, Fla: CRC Press, 2010.
- [55] X. H. Chen, J. Lu, L. Lu, and K. Lu, "Tensile properties of a nanocrystalline 316L austenitic stainless steel," *Scripta Materialia*, vol. 52, no. 10, pp. 1039-1044, 2005/05/01/ 2005.
- [56] D. M. Rosa, J. E. Spinelli, I. L. Ferreira, and A. Garcia, "Cellular/Dendritic Transition and Microstructure Evolution during Transient Directional Solidification of Pb-Sb Alloys," *Metallurgical and Materials Transactions A*, journal article vol. 39, no. 9, pp. 2161-2174, September 01 2008.
- [57] S. Suwas and R. K. Ray, *Crystallographic Texture of Materials* (Engineering Materials and Processes). London: Springer-Verlag, 2014.
- [58] D. A. Porter, K. E. Easterling, and M. Y. Sherif, *Phase transformations in metals and alloys*, 3rd ed. ed. Boca Raton, Fla: CRC Press, 2009.
- [59] Ø. Grong, *Metallurgical modelling of welding* (Materials modelling series). London: Institute of Materials, 1994.
- [60] Y. Smith. (2017, 25.01). *Limitations of Optical Microscopy*. Available: <https://www.news-medical.net/life-sciences/Limitations-of-Optical-Microscopy.aspx>
- [61] S. Swapp. (2017, 26.01). *Scanning Electron Microscopy (SEM)*. Available: https://serc.carleton.edu/research_education/geochemsheets/techniques/SEM.html
- [62] J. Hjelen and Sintef, *Scanning elektron-mikroskopi*. Trondheim: SINTEF, 1989.
- [63] F. G. Banica. (2009, 26.01). *Moseleys Law*. Available: <http://folk.ntnu.no/floban/KJ%20%203055/X%20%20Ray/Moseley/Moseley%20law.htm>
- [64] J. I. Goldstein, *Scanning electron microscopy and X-ray microanalysis*, 3rd ed. ed. New York: Kluwer Academic/Plenum Publishers, 2003.
- [65] O. I. Plc. (2018, 31.01). *EBSD Detector Setings*. Available: <http://www.ebsd.com/8-hints-tips-for-ebsd-data-collection>
- [66] D. B. Williams and C. B. Carter, *Transmission electron microscopy : a textbook for materials science : Part 1 : Basics*, 2nd ed. ed. New York: Springer, 2009.
- [67] J. K. Solberg and V. Hansen, *Innføring i transmisjon elektronmikroskopi*. S.l.: s.n., 2007.
- [68] P. E. Champness, *Electron diffraction in the transmission electron microscope* (Microscopy handbooks). Oxford: BIOS Scientific Publ., 2001.
- [69] *ASTM E384-17 Standard Test Method for Microindentation Hardness of Materials*, 2017.
- [70] O. Metco, "Material Product Data Sheet Austenitic Stainless Steel Powder for Laser Cladding," ed: Oerlikon Metco, 2014.
- [71] *Struers Metallographic preparation of powder metallurgy parts*, 2008.

- [72] *ASTM E3-11(2017), Standard Guide for Preparation of Metallographic Specimens*, 2017.
- [73] *Struers Metallographic preparation of stainless steel*, 2016.
- [74] V. H. Lysne, "Microstructural and physical investigation on the effect of process parameters on stainless steel 316L prepared by Selective Laser Melting," Master, Department of Mechanical and Structural Engineering and Materials Science University of Stavanger, 2016.
- [75] S. Katayama and A. Matsunawa, in *ICALEO*, Boston, 1984, pp. 60-67: Toledo Ohio : LIA-the Laser Institute of America.
- [76] M. Ma, Z. Wang, and X. Zeng, "A comparison on metallurgical behaviors of 316L stainless steel by selective laser melting and laser cladding deposition," *Materials Science and Engineering: A*, vol. 685, pp. 265-273, 2017/02/08/ 2017.
- [77] J. W. Fu, Y. S. Yang, J. J. Guo, and W. H. Tong, "Effect of cooling rate on solidification microstructures in AISI 304 stainless steel," *Materials Science and Technology*, vol. 24, no. 8, pp. 941-944, 2008/08/01 2008.
- [78] J. W. Elmer, S. M. Allen, and T. W. Eagar, "Microstructural development during solidification of stainless steel alloys," *Metallurgical Transactions A*, journal article vol. 20, no. 10, pp. 2117-2131, October 01 1989.
- [79] M. Gäumann, S. Henry, F. Cléton, J. D. Wagnière, and W. Kurz, "Epitaxial laser metal forming: analysis of microstructure formation," *Materials Science and Engineering: A*, vol. 271, no. 1, pp. 232-241, 1999/11/01/ 1999.
- [80] K. Zhang, S. Wang, W. Liu, and X. Shang, "Characterization of stainless steel parts by Laser Metal Deposition Shaping," *Materials & Design*, vol. 55, pp. 104-119, 2014/03/01/ 2014.
- [81] L. Song, G. Zeng, H. Xiao, X. Xiao, and S. Li, "Repair of 304 stainless steel by laser cladding with 316L stainless steel powders followed by laser surface alloying with WC powders," *Journal of Manufacturing Processes*, vol. 24, pp. 116-124, 2016/10/01/ 2016.
- [82] Y. Zhang, L. Yang, J. Dai, Z. Huang, and T. Meng, "Grain growth of Ni-based superalloy IN718 coating fabricated by pulsed laser deposition," *Optics & Laser Technology*, vol. 80, pp. 220-226, 2016/06/01/ 2016.
- [83] L. L. Parimi, R. G. A. D. Clark, and M. M. Attallah, "Microstructural and texture development in direct laser fabricated IN718," *Materials Characterization*, vol. 89, pp. 102-111, 2014/03/01/ 2014.
- [84] T. Niendorf, S. Leuders, A. Riemer, H. A. Richard, T. Tröster, and D. Schwarze, "Highly Anisotropic Steel Processed by Selective Laser Melting," *Metallurgical and Materials Transactions B*, journal article vol. 44, no. 4, pp. 794-796, August 01 2013.
- [85] P. Liu and T. Sandvik Materials, *Phase analysis in steel using analytical transmission electron microscopy*. Sandviken: Sandvik Materials Technology, 2004.

- [86] S. A. David, S. E. Hanzelka, and C. P. Haltom, "Ferrite morphology and variations in ferrite content in austenitic stainless steel welds,"; Oak Ridge National Lab., TN (USA)ORNL/TM-7810; Other: ON: DE81027826 United States Other: ON: DE81027826 NTIS, PC A03/MF A01. ORNL English, 1981.
- [87] J. C. Lippold and W. F. Savage, "Solidification of Austenitic Stainless Steel Weldments: Part 1-A Proposed Mechanism," *Welding Journal*, vol. 58, pp. 362-374, 1979.
- [88] T. A. Mozhi, W. A. T. Clark, and B. E. Wilde, "The effect of nitrogen and carbon on the stress corrosion cracking performance of sensitized AISI 304 stainless steel in chloride and sulfate solutions at 250°C," *Corrosion Science*, vol. 27, no. 3, pp. 257-273, 1987/01/01/ 1987.
- [89] D. H. Kumar. and A. S. Reddy, "Study of Mechanical Behavior in Austenitic Stainless Steel 316 LN Welded Joints," *International Journal of Mechanical Engineering and Robotics Research*, vol. Vol.2, no. No.1, pp. pp. 37-56, 2013.
- [90] L. Liu *et al.*, "Dislocation network in additive manufactured steel breaks strength–ductility trade-off," *Materials Today*, 2017/12/06/ 2017.
- [91] K. Saeidi, X. Gao, F. Lofaj, L. Kvetková, and Z. J. Shen, "Transformation of austenite to duplex austenite-ferrite assembly in annealed stainless steel 316L consolidated by laser melting," *Journal of Alloys and Compounds*, vol. 633, pp. 463-469, 2015/06/05/ 2015.
- [92] C. Qiu, M. A. Kindi, A. S. Aladawi, and I. A. Hatmi, "A comprehensive study on microstructure and tensile behaviour of a selectively laser melted stainless steel," *Scientific Reports*, vol. 8, no. 1, p. 7785, 2018/05/17 2018.
- [93] D.-R. Eo, S.-H. Park, and J.-W. Cho, "Inclusion evolution in additive manufactured 316L stainless steel by laser metal deposition process," *Materials & Design*.
- [94] P. Ganesh *et al.*, "Studies on pitting corrosion and sensitization in laser rapid manufactured specimens of type 316L stainless steel," *Materials & Design*, vol. 39, pp. 509-521, 2012/08/01/ 2012.
- [95] H. S. Khatak and B. Raj, *Corrosion of austenitic stainless steels : mechanism, mitigation and monitoring*. Cambridge: Woodhead Publ., 2002.
- [96] A. Kourdani and R. Derakhshandeh-Haghighi, "Evaluating the Properties of Dissimilar Metal Welding Between Inconel 625 and 316L Stainless Steel by Applying Different Welding Methods and Consumables," *Metallurgical and Materials Transactions A*, journal article vol. 49, no. 4, pp. 1231-1243, April 01 2018.
- [97] T. L. Anderson, *Fracture mechanics : fundamentals and applications*, 3rd ed. ed. Boca Raton, Fla: Taylor & Francis, 2005.
- [98] A. Röttger, K. Geenen, M. Windmann, F. Binner, and W. Theisen, "Comparison of microstructure and mechanical properties of 316L austenitic steel processed by selective laser melting with hot-isostatic pressed and cast

- material," *Materials Science and Engineering: A*, vol. 678, pp. 365-376, 2016/12/15/ 2016.
- [99] C. Jing, L. Xin, W. Tao, Y. Haiou, and H. Weidong, "The Hot Cracking Mechanism of 316L Stainless Steel Cladding in Rapid Laser Forming Process," *Rare Metal Materials and Engineering*, vol. 32, no. 3, pp. 183-186, 2003.
- [100] S. Sun, M. Brandt, J. Harris, and Y. Durandet, "The influence of stellite 6 particle size on the inter-track porosity in multi-track cladding," *Surface and Coatings Technology*, vol. 201, no. 3, pp. 998-1005, 2006/10/05/ 2006.
- [101] J. Yu *et al.*, "Influence of laser deposition patterns on part distortion, interior quality and mechanical properties by laser solid forming (LSF)," *Materials Science and Engineering: A*, vol. 528, no. 3, pp. 1094-1104, 2011/01/25/ 2011.
- [102] M. Akbari-Garakani and M. Mehdizadeh, "Effect of long-term service exposure on microstructure and mechanical properties of Alloy 617," *Materials & Design*, vol. 32, no. 5, pp. 2695-2700, 2011/05/01/ 2011.
- [103] N. Moslemi, N. Redzuan, N. Ahmad, and T. N. Hor, "Effect of Current on Characteristic for 316 Stainless Steel Welded Joint Including Microstructure and Mechanical Properties," *Procedia CIRP*, vol. 26, pp. 560-564, 2015/01/01/ 2015.
- [104] M. O. Sklyar, G. A. Turichin, O. G. Klimova, O. G. Zotov, and I. K. Topalov, "Microstructure of 316L stainless steel components produced by direct laser deposition," *Steel in Translation*, journal article vol. 46, no. 12, pp. 883-887, December 01 2016.
- [105] A. A. Bayode, ET; Pityana, S, "Characterization of laser metal deposited 316L stainless steel," Accessed on: 26.02.2018 Available: <https://researchspace.csir.co.za/dspace/handle/10204/8999>

Appendix A *ImageJ procedure*

Procedure for surface porosity analysis in ImageJ.

2. Select an image in software ImageJ
3. Menu bar: *Analyse -> Set scale -> Remove scale -> ok*
4. Zoom in on scale bar -> draw a line with length of the scale bar, *hold shift* while drawing to generate vertical line
5. Menu bar: *Analyse -> Set scale -> Insert length of scale bar in "known distance" -> Insert units in "unit length"*
6. Image is now calibrated for porosity measurements
7. Use "Rectangular" to mark an area for analysis: Menu bar: *Image -> Duplicate-> Title -> ... -> ok*
8. *Image -> Adjust -> Threshold -> B&W -> Apply -> Exit*
9. *Analyse -> Analyse particles -> Settings:*
 - Size (μm^2): 0-infinity
 - Circularity 0.00-1.00
 - Show: Outlines
 - Display results: yes
 - Clear results: yes
 - Exclude on edges: yes
10. *Save results -> Open data in excel for calculation of porosity*

Appendix B *Microstructural contrasts*

Supplemental images with higher magnification from the light optical microscope for the differences observed in the layers, Figure 27.

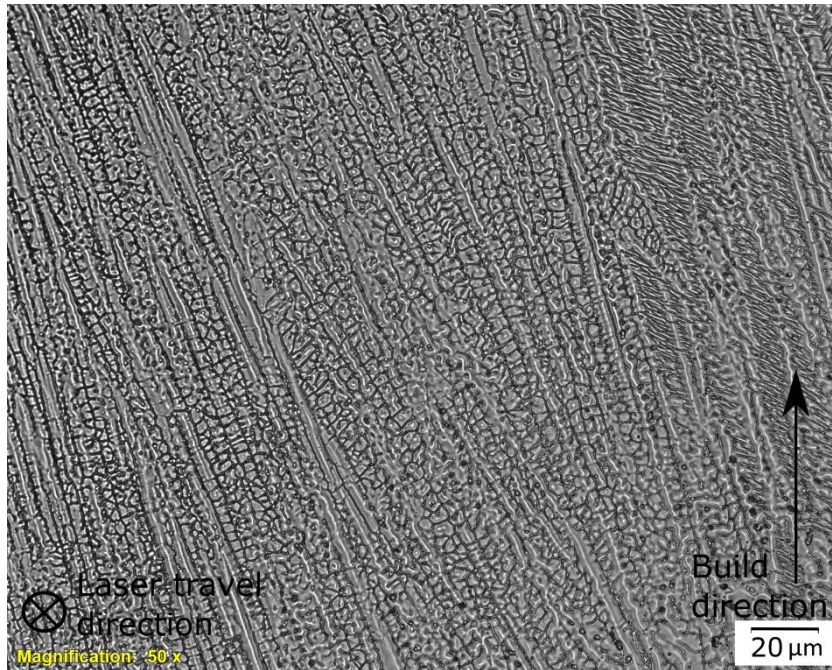


Figure A. 1: Cellular dendrites observed in centred line-deposit in layer N7 for sample 3.

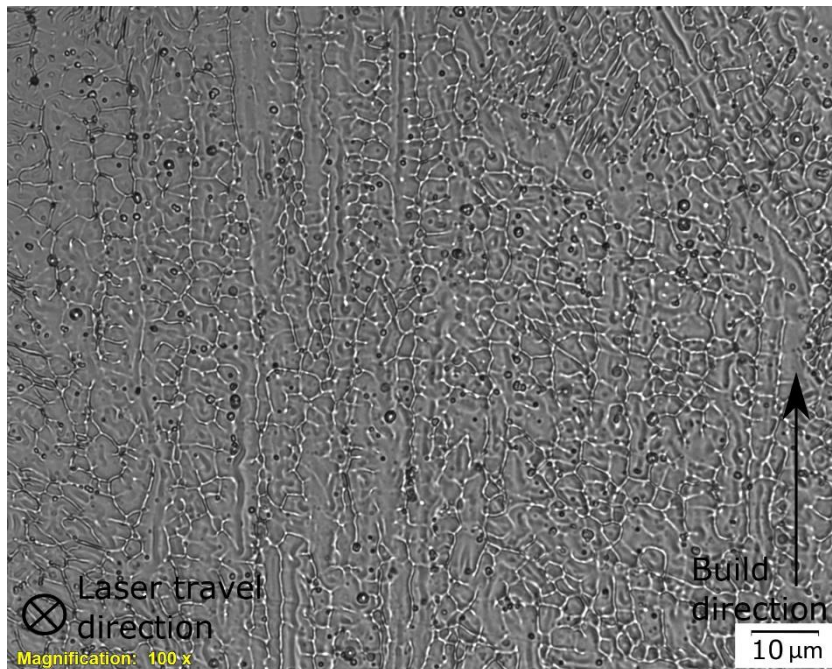


Figure A. 2: Higher magnification of the cellular dendrites observed in centred line-deposit in layer N7 for sample 3.

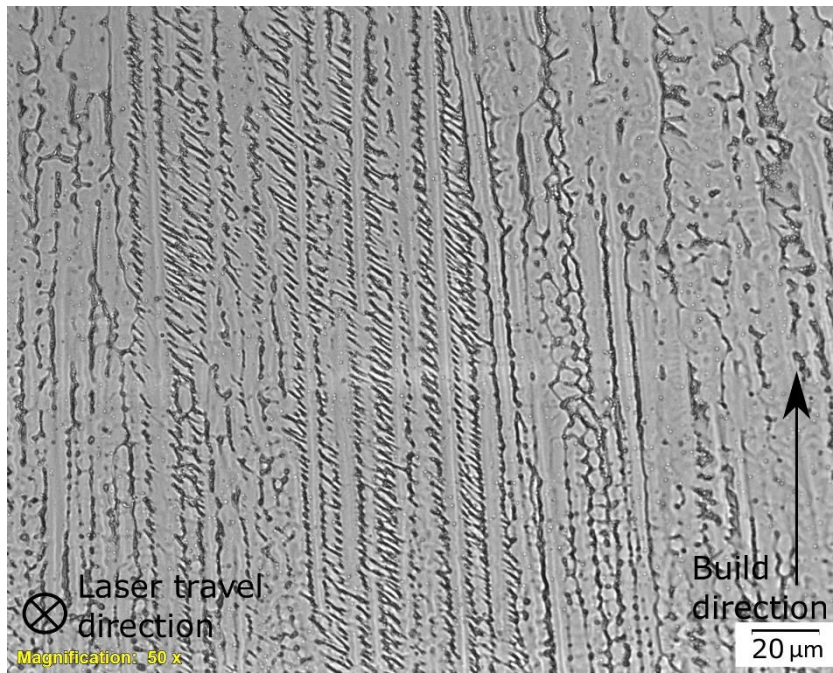


Figure A. 3: Columnar dendrites with secondary dendritic arms observed towards the edge in layer N7 for sample 3.

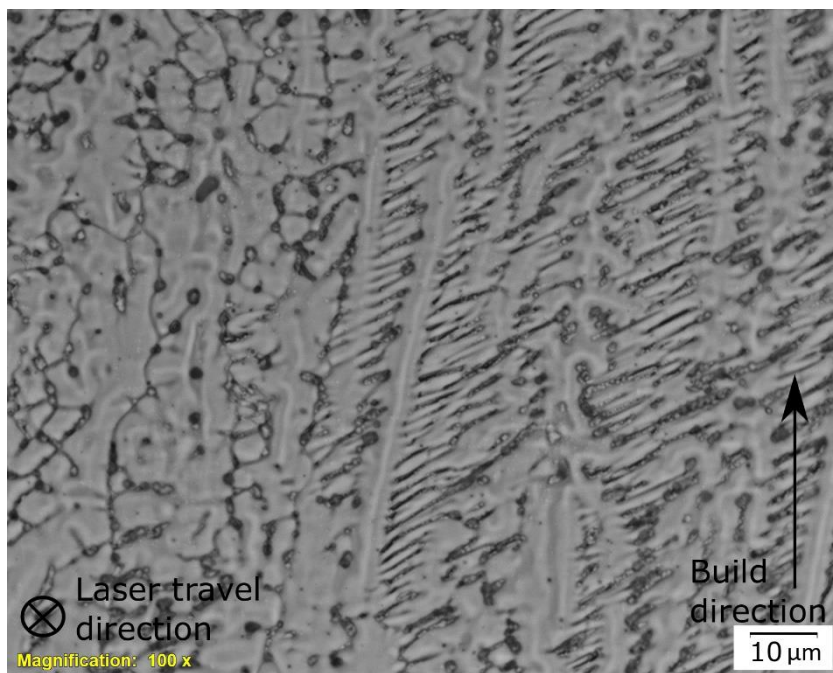


Figure A. 4: Higher magnification of the columnar dendrites with secondary dendritic arms observed towards the edge in layer N7 for sample 3.

Appendix C Fusion boundary and HAZ

Supplemental images for the fusion and resulting heat-affected zone between the deposited SS316L-Si and base materials.

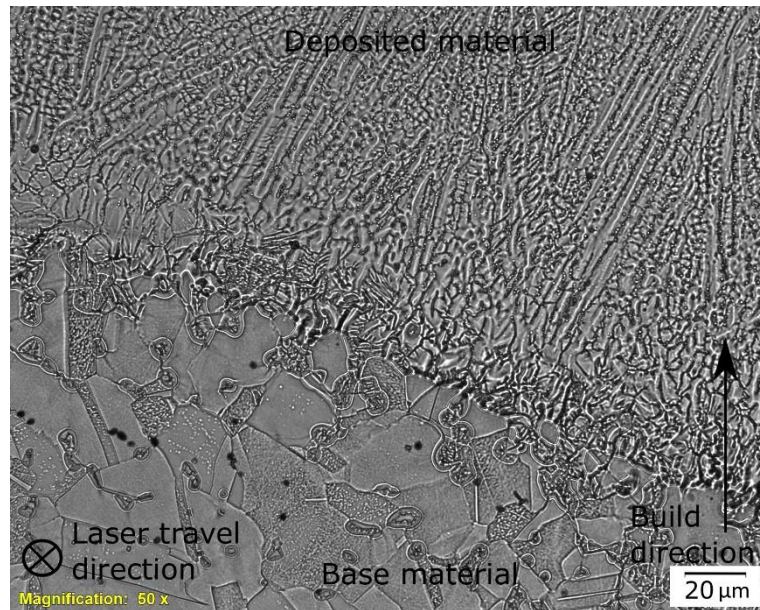


Figure A. 5: LOM-graph of solid fusion between deposited- and base material in sample 3.

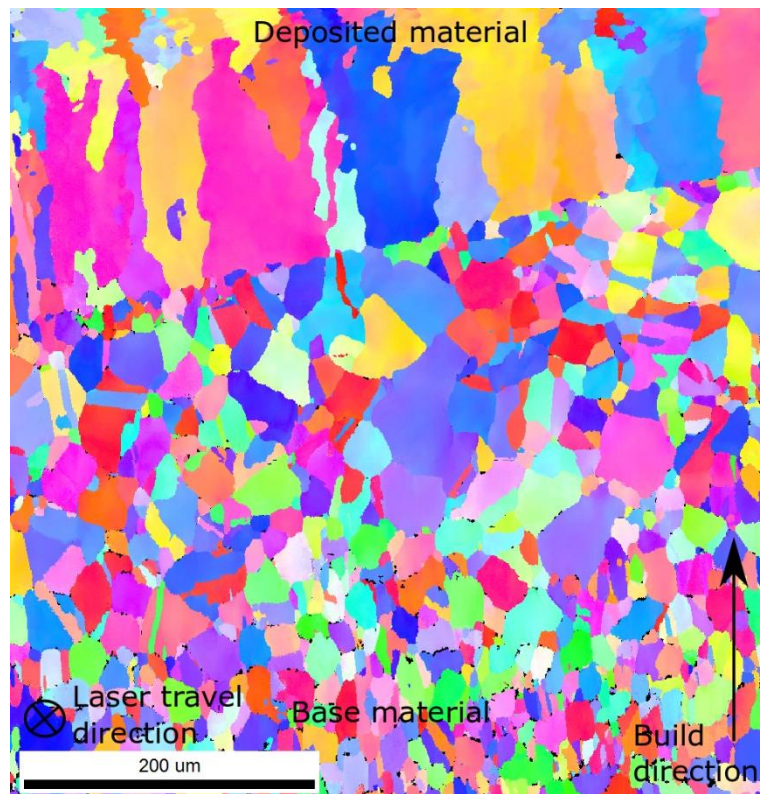


Figure A. 6: EBSD inverse pole mapping over the resulting heat-affected zone after the deposition process for sample 1.

Appendix D *Hardness data*

Tabulated results from hardness measurements for all 4 samples in both parallel to- and normal to build direction:

| Sample 1 – SS316L-Si DLD on SS304 | Parallel to build direction | Normal to build direction | |
|---|--------------------------------|---------------------------|-------------|
| | Set 1 | Set 1 - Middle | Set 2 - HAZ |
| Deposited material | 181 | 159 | 174 |
| | 176 | 167 | 175 |
| | 174 | | |
| | 175 | | |
| | 177 | | |
| | 177 | | |
| | 168 | | |
| | 159 | | |
| | 173 | | |
| | 174 | | |
| | 186 | | |
| | 265 | | |
| 258 | | | |
| Average | | 163 | 174.5 |
| Total average (exclusive base material) | 174.42 | | 167.75 |

| Sample 2 – SS316L-Si DLD on SS304 | Parallel to build direction | | Normal to build direction | | |
|--|--------------------------------|-------|---------------------------|-------------------|----------------|
| | Set 1 | Set 2 | Set 1 - Top | Set 2 - Middle | Set 3 - HAZ |
| Deposited material | 171 | 111 | 111 | 171 | 183 |
| | 179 | 146 | 140 | 167 | 184 |
| | 179 | 166 | 150 | 169 | 178 |
| | 187 | 161 | 137 | 172 | 181 |
| | 185 | 167 | 117 | 183 | 182 |
| | 182 | 166 | 140 | 181 | 178 |
| | 184 | 169 | 171 | 175 | 182 |
| | 164 | 170 | | 185 | 180 |
| | 175 | 171 | | | |
| | 183 | 171 | | | |
| | 180 | 184 | | | |
| Base material | 257 | 256 | | | |
| | 254 | 276 | | | |
| | 248 | 269 | | | |
| | 240 | 257 | | | |
| | 248 | 246 | | | |
| | 241 | 260 | | | |
| Average | 179 | 162 | 138 | 175.375 | 181 |
| Total average (exclusive base material) | 170.5 | | | 164.79 | |

| Sample 3 – SS316L-Si DLD on SS316L | Parallel to build direction | | Normal to build direction | | |
|--|--------------------------------|--------|---------------------------|-------------------|----------------|
| | Set 1 | Set 2 | Set 1 - Top | Set 2 - Middle | Set 3 - HAZ |
| Deposited material | 170 | 169 | 170 | 172 | 179 |
| | 175 | 167 | 169 | 162 | 178 |
| | 175 | 176 | 161 | 176 | 167 |
| | 168 | 170 | | | |
| | 172 | 162 | | | |
| | 163 | 170 | | | |
| | 167 | 166 | | | |
| | 171 | 175 | | | |
| Base material | 179 | 178 | | | |
| | 184 | 178 | | | |
| | 174 | 176 | | | |
| | 177 | 177 | | | |
| Average | 172.4 | 170.33 | 166.67 | 170 | 174.67 |
| Total average (exclusive base material) | 171.37 | | 170.44 | | |

| Sample 4 – SS316L-Si DLD on SS316L | Parallel to build direction | | Normal to build direction | | |
|--|--------------------------------|---------|---------------------------|-------------------|----------------|
| | Set 1 | Set 2 | Set 1 - Top | Set 2 - Middle | Set 3 - HAZ |
| Deposited material | 172 | 175 | 163 | 165 | 181 |
| | 175 | 158 | 175 | 176 | 179 |
| | 175 | 166 | 175 | 170 | 183 |
| | 176 | 163 | 172 | 171 | 181 |
| | 163 | 174 | 169 | 172 | 176 |
| | 176 | 174 | 175 | 184 | 180 |
| | 185 | 172 | 172 | 163 | 183 |
| | 179 | 183 | | | |
| Base material | 180 | 184 | | | |
| | 177 | 181 | | | |
| | 181 | 183 | | | |
| | 181 | 177 | | | |
| Average | 175.125 | 170.625 | 171.57 | 171.57 | 180.43 |